

# Exoplanetary Microlensing

**B. Scott Gaudi**

The Ohio State University

Gravitational microlensing occurs when a foreground star happens to pass very close to our line of sight to a more distant background star. The foreground star acts as a lens, splitting the light from the background source star into two images, which are typically unresolved. However, these images of the source are also magnified, by an amount that depends on the angular separation between the lens and source. The relative motion between the lens and source therefore results in a time-variable magnification of the source: a microlensing event. If the foreground star happens to host a planet with projected separation near the paths of these images, the planet will also act as a lens, further perturbing the images and resulting in a characteristic, short-lived signature of the planet. This chapter provides an introduction to the discovery and characterization of exoplanets with gravitational microlensing. The theoretical foundation of the method is reviewed, focusing in particular on the phenomenology of planetary microlensing perturbations. The strengths and weakness of the microlensing technique are discussed, highlighting the fact that it is sensitive to low-mass planetary companions to stars throughout the Galactic disk and foreground bulge, and that its sensitivity peaks for planet separations just beyond the snow line. An overview of the practice of microlensing planet searches is given, with a discussion of some of the challenges with detecting and analyzing planetary perturbations. The chapter concludes with a review of the results that have been obtained to date, and a discussion of the near and long-term prospects for microlensing planet surveys. Ultimately, microlensing is potentially sensitive to multiple-planet systems containing analogs of all the solar system planets except Mercury, as well as to free floating planets, and will provide a crucial test of planet formation theories by determining the demographics of planets throughout the Galaxy.

## 1. INTRODUCTION

Gravitational lensing generally refers to the bending of light rays of a background light source by a foreground mass. Gravitational microlensing, on the other hand, traditionally refers to the special case when multiple images are created but have separations of less than a few milliarcseconds, and hence are unresolved with current capabilities. Although the idea of the gravitational deflection of light by massive bodies well predates General Relativity, and can be traced as far back as Sir Isaac Newton<sup>1</sup>, the concept of gravitational microlensing appears to be attributable to Einstein himself. In 1936 Einstein published a paper in which he derived the equations of microlensing by a foreground star closely aligned to a background star (*Einstein*, 1936). Indeed it seems that Einstein had been thinking about this idea as far back as 1912 (*Renn et al.*, 1997), and perhaps had even hoped to use the phenomenon to explain the appearance of Nova Geminorum 1912 (*Sauer*, 2008). However, by 1936 he had dismissed the practical significance of the microlensing effect, concluding that “there is no great chance of observing this phenomenon” (*Einstein*, 1936).

Indeed, there is no “great chance” of observing gravitational microlensing. The optical depth to gravitational microlensing, i.e., the probability that any given star is being appreciably lensed at any given time, is of order  $10^{-6}$  to-

ward the Galactic bulge, and is generally similar or smaller for other lines of sight<sup>2</sup>. Thus at least partly due to this low probability, the idea of gravitational microlensing lay mostly dormant for five decades after Einstein’s 1936 paper (with some notable exceptions, e.g., *Liebes*, 1964; *Refsdal*, 1964). It was not until the seminal paper by *Paczynski* (1986) that the idea of gravitational microlensing was resurrected, and then finally put into practice with the initiation of several observational searches for microlensing events toward the Large and Small Magellanic Clouds and Galactic bulge in the early 1990s (*Alcock et al.* 1993; *Aubourg et al.* 1993; *Udalski et al.*, 1993). The roster of detected microlensing events now numbers in the thousands. These events have been discovered by many different collaborations, toward several lines of sight including the Magellanic Clouds (*Alcock et al.*, 1997, 2000; *Palanque-Delabrouille et al.*, 1998), and M31 (*Paulin-Henriksson et al.* 2002; *de Jong et al.*, 2004; *Uglesich et al.*, 2004; *Calchi Novati et al.*, 2005), with the vast majority found toward the Galactic bulge (*Udalski et al.*, 2000; *Sumi et al.*, 2003; *Thomas et al.*, 2005; *Hamadache et al.*, 2006) or nearby fields in the Galactic plane (*Derue et al.*, 2000).

<sup>1</sup> See *Schneider et al.* 1992 for a thorough recounting of the history of gravitational lensing.

<sup>2</sup> The phenomenon of gravitational lensing of multiply-imaged quasars by stars in the foreground galaxy that is creating the multiple images of the quasar is also referred to as microlensing. In this instance the optical depth to microlensing can be of order unity. However, in this chapter we are concerned only with gravitational microlensing of stars within our Galaxy or in nearby galaxies, where the optical depths to microlensing are always small.

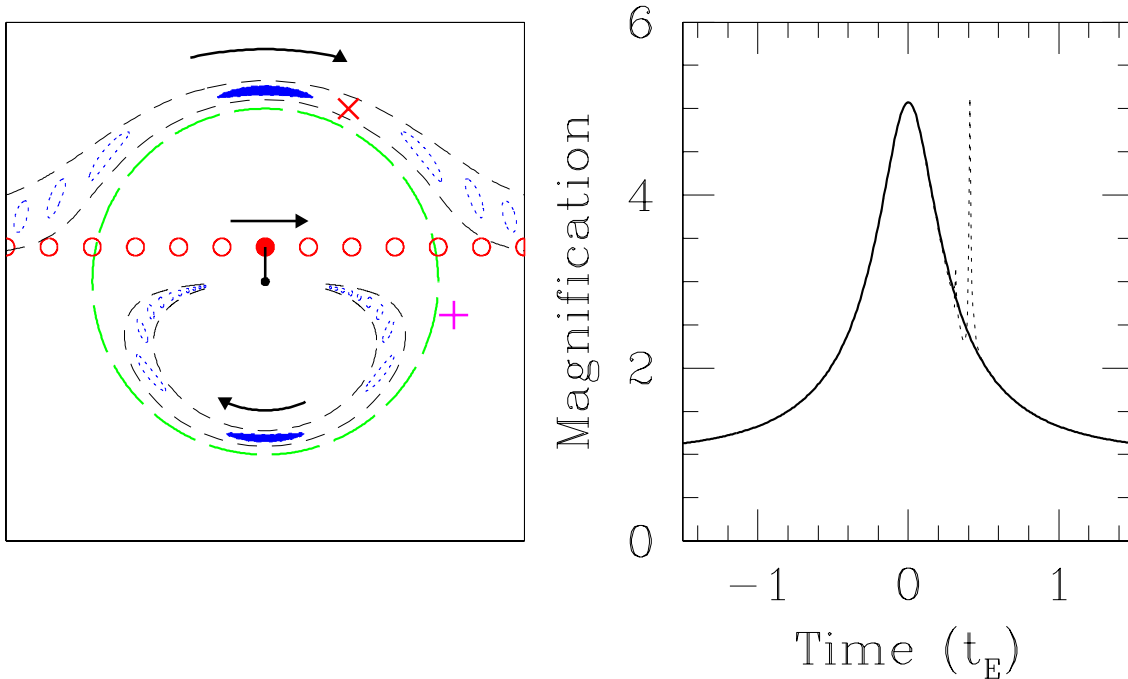


Fig. 1.— Left: The images (dotted ovals) are shown for several different positions of the source (solid circles), along with the primary lens (dot) and Einstein ring (long dashed circle). If the primary lens has a planet near the path of one of the images, i.e. within the short-dashed lines, then the planet will perturb the light from the source, creating a deviation to the single lens light curve. Right: The magnification as a function of time is shown for the case of a single lens (solid) and accompanying planet (dotted) located at the position of the X in the left panel. If the planet was located at the + instead, then there would be no detectable perturbation, and the resulting light curve would be essentially identical to the solid curve.

Even before the first microlensing events were detected, it was suggested by *Mao & Paczynski* (1991) that gravitational microlensing might also be used to discover planetary companions to the primary microlens stars. The basic idea is illustrated in Figure 1. As the foreground star passes close to the line of sight to the background source, it splits the source into two images, which sweep out curved trajectories on the sky as the foreground lens star passes close to the line of sight to the source. These images typically have separations of order one milliarcsecond, and so are unresolved. However, the total area of these images is also larger than the area of the source, and as a result the background star also exhibits a time-variable magnification, which is referred to as a microlensing event. If the foreground star happens to host a planet with projected separation near the paths of one of these two images, the planet will further perturb the image, resulting in a characteristic, short-lived signature of the planet.

*Gould & Loeb* (1992) considered this novel method of detecting planets in detail, and laid out the practical requirements for an observational search for planets with microlensing. In particular, they advocated a “two tier” approach. First, microlensing events are discovered and alerted real-time by a single survey telescope that monitors many square degrees of the Galactic bulge on a roughly nightly basis. Second, these ongoing events are then densely monitored with many smaller telescopes to dis-

cover the short-lived signatures of planetary perturbations.

The search for planets with microlensing began in earnest in 1995 with the formation of several follow-up collaborations dedicated to searching for planetary deviations in ongoing events (*Albrow et al.*, 1998; *Rhie et al.* 2000). These initial searches adopted the basic approach advocated by *Gould & Loeb* (1993): monitoring ongoing events alerted by several survey collaborations (e.g., *Udalski et al.*, 1994; *Alcock et al.* 1996), using networks of small telescopes spread throughout the southern hemisphere. Although microlensing planet searches have matured considerably since their initiation, this basic approach is still used to this day, with the important modification that current follow-up collaborations tend to focus on high-magnification events, which individually have higher sensitivity to planets (*Griest & Safizadeh*, 1998), as discussed in detail below.

From 1995–2001, no convincing planet detections were made, primarily because the relatively small number of events being alerted each year ( $\sim 50 - 100$ ) by the survey collaborations meant that there were only a few events ongoing at any given time, and often these were poorly suited for follow-up. Although interesting upper limits were placed on the frequency of Jovian planets (*Gaudi et al.* 2002, *Snodgrass et al.*, 2004), perhaps the most important result during this period was the development of both the theory and practice of the microlensing method, which re-

sulted in its transformation from a theoretical abstraction to a viable, practical method of searching for planets.

In 2001, the OGLE collaboration (*Udalski, 2003*) upgraded to a new camera with a 16 times larger field of view and so were able to monitor a larger area of the bulge with a higher cadence. As a result, in 2002 OGLE began alerting nearly an order of magnitude more events per year than previous to the upgrade. These improvements in the alert rate and cadence, combined with improved cooperation and coordination between the survey and follow-up collaborations, led to the first discovery of an extrasolar planet with microlensing in 2003 (*Bond et al. 2004*). The MOA collaboration upgraded to a 1.8m telescope and 2 deg<sup>2</sup> camera in 2004 (*Sako et al., 2008*), and in 2007 the OGLE and MOA collaborations started alerting  $\sim 850$  events per year, thus ushering in the “golden age” of microlensing planet searches.

The first detections of exoplanets with microlensing (*Bond et al., 2004; Udalski et al., 2005; Beaulieu et al., 2006; Gould et al., 2006; Gaudi et al., 2008a; Bennett et al., 2008; Dong et al., 2009; Janczak et al., 2009; Sumi et al., 2009*) have provided important lessons about the kinds of information that can be extracted from observed events. When microlensing planet surveys were first being developed, it was thought that the primary virtue of the method would be solely its ability to provide statistics on large-separation and low-mass planets. Individual detections would be of little interest because the only routinely measured property of the planets would be the planet/star mass ratio, and the nature of the host star in any given system would remain unknown because the microlensing event itself provides little information about the properties of the host star, and follow-up reconnaissance would be difficult or impossible due to the large distances of the detected systems from Earth. In fact, experience with actual events has shown that much more information can typically be gleaned from a combination of a detailed analysis of the light curve, and follow-up, high-resolution imaging. As a result, in most cases it is possible to infer the mass of the primary lens and the basic physical properties of planetary system, including the planet mass and physical separation. In some special cases it is possible to infer considerably more information.

The theoretical foundation of microlensing is highly technical, the practical challenges associated with searching for planets with microlensing are great, and the analysis of observed microlensing datasets is complicated and time-consuming. Furthermore, although it is possible to learn far more about individual systems than was originally thought, extracting this information is difficult, and it is certainly the case that the systems will never be as well studied as planets systems found by other methods in the solar neighborhood.

Give the intrinsic limitations and difficulties of the microlensing method, and might therefore wonder: “why bother?” The primary motivation for going to all this trouble is that microlensing is sensitive to planets in a region of parameter space that is difficult or impossible to probe with

other methods, namely low-mass planets beyond the ‘snow line’, the point in the protoplanetary disk beyond which ices can exist. The snow line plays a crucial role in the currently-favored model of planet formation. Thus, even the first few microlensing planet detections have provided important constraints on planet formation theories. The second generation of microlensing surveys will potentially be sensitive to multiple-planet systems containing analogs of all the solar system planets except Mercury, as well as to free floating planets. Ultimately, when combined with the results from other complementary surveys, microlensing surveys can potentially yield a complete picture of the demographics of essentially *all* planets with masses greater than that of Mars. Thus it is well worth the effort, even given the drawbacks.

The primary goal of this chapter is to provide a general introduction to gravitational microlensing and searches for planets using this method. Currently, the single biggest obstacle to the progress of microlensing searches for planets is simply a lack of human power. There are already more observed binary and planetary events than can be modeled by the handful of researchers in the world with sufficient expertise to do so. This situation is likely to get worse when next-generation microlensing planet surveys come on line. However, because the theoretical foundation of microlensing is quite technical and the practical implementation of microlensing planet searches is fairly complex, it can be very difficult and time consuming for the uninitiated to gain sufficient familiarity with the field to make meaningful contributions. This difficulty is exacerbated by the fact that the explanations of the relevant concepts are scattered over dozens of journal articles. The aim of this chapter is to partially remedy this situation by providing a reasonably comprehensive review, which a beginner can use to gain at least a basic familiarity with the many concepts, tools, and techniques that are required to actively participate and contribute to current microlensing planet searches. Readers are encouraged to peruse reviews by *Paczynski 1996, Sackett 1999, Mao 2008, and Bennett 2009a* for additional background material.

Section 2 provides an overview of the theory of gravitational microlensing searches for planets. This is the heart of the chapter, and is fairly long and detailed. Much of this section may not be of interest to all readers, and some of the material may be too technical for a beginner to the subject. Therefore, the first subsection (2.1) provides a primer on the basic properties and features of microlensing. Beginners, or casual readers who are only interested in a basic introduction to the method itself and its features, can read only this section (paying particular attention to Figures 1, 2, and 3), and then skip to Section 4. Section 3 discusses the practical implementation of planetary microlensing, while Section 4 reviews the basic advantages and drawbacks of the method. Section 5 provides a summary of the results to date, as well as a brief discussion of their implications. Section 6 discusses future prospects for microlensing planet searches, and in particular the expected yields of a next-

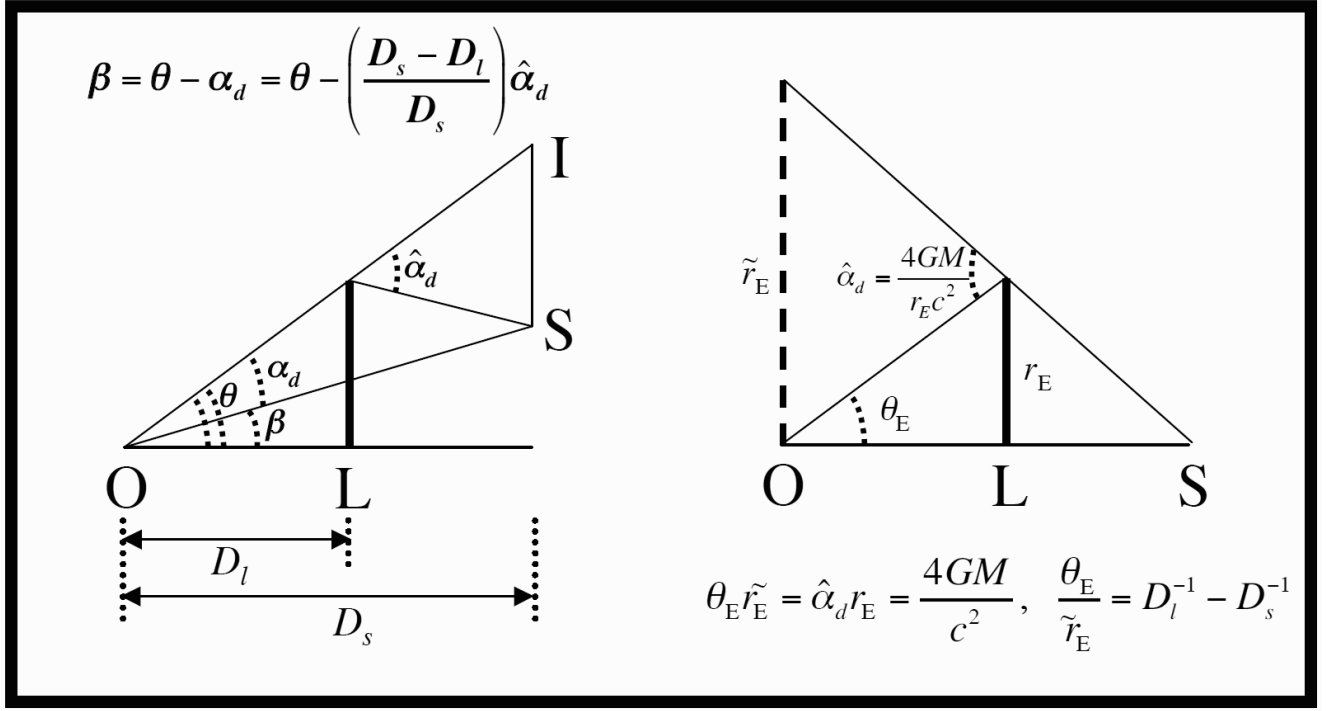


Fig. 2.— Left: The lens (L) at a distance  $D_l$  from the observer (O) deflects light from the source (S) at distance  $D_s$  by the Einstein bending angle  $\hat{\alpha}_d$ . The angular positions of the images  $\theta$  and unlensed source  $\beta$  are related by the lens equation,  $\beta = \theta - \alpha_d = \theta - (D_s - D_l)/D_s \hat{\alpha}_d$ . For a point lens,  $\hat{\alpha}_d = 4GM/(c^2 D_l \theta)$ . Right: Relation of higher-order observables, the angular ( $\theta_E$ ) and projected ( $\tilde{r}_E$ ) Einstein radii, to physical characteristics of the lensing system. Adapted from Gould, 2000.

generation ground-based planet search, and a space-based mission.

## 2. FOUNDATIONAL CONCEPTS AND EQUATIONS

### 2.1. Basic Microlensing

This section provides a general overview of the basic equations, scales, and phenomenology of microlensing by a point mass, and a brief introduction to how microlensing can be used to find planets, and how such planet searches work in practice. It is meant to be self-contained, and therefore the casual reader who is not interested in a detailed discourse on the theory, phenomenology, and practice of planetary microlensing can simply read this section and then skip to Section 4 without significant loss of continuity.

A microlensing event occurs when a foreground “lens” happen to pass very close to our line of sight to a more distant background “source.” Microlensing is a relatively improbable phenomenon, and so in order to maximize the event rate, microlensing survey are typically carried out toward dense stellar fields. In particular, the majority of microlensing planet surveys are carried out toward the Galactic center. Therefore, for our purposes, the lens is typically a main-sequence star or stellar remnant in the foreground Galactic disk or bulge, whereas the source is a main-sequence star or giant typically in the bulge.

The left panel of Figure 2 shows the basic geometry of microlensing. Light from the source at a distance  $D_s$  is

deflected by an angle  $\hat{\alpha}_d$  by the lens at a distance  $D_l$ . For a point lens,  $\hat{\alpha}_d = 4GM/(c^2 D_l \theta)$ , where  $M$  is the mass of the lens, and  $\theta$  is the angular separation of the images of the source and the lens on the sky<sup>3</sup>. The relation between  $\theta$ , and the angular separation  $\beta$  between the lens and source in the absence of lensing, is called the *lens equation*, and is given trivially by  $\beta = \theta - \alpha_d$ . From basic geometry and using the small-angle approximation,  $\hat{\alpha}_d(D_s - D_l) = \alpha_d D_s$ . Therefore, for a point lens,

$$\beta = \theta - \frac{4GM}{c^2 \theta} \frac{D_s - D_l}{D_s D_l}. \quad (1)$$

The left panel of Figure 3 shows the basic source and image configurations for microlensing by a single point mass. From Equation 1, if the lens is exactly aligned with the source ( $\beta = 0$ ), it images the source into an “Einstein ring” with a radius  $\theta_E = \sqrt{\kappa M \pi_{\text{rel}}}$ , where  $M$  is the mass of the lens,  $\pi_{\text{rel}} = \text{AU}/D_{\text{rel}}$  is the relative lens-source parallax,  $D_{\text{rel}} \equiv (D_l^{-1} - D_s^{-1})^{-1}$  is the relative lens-source distance, and  $\kappa = 4G/c^2 \text{AU} \simeq 8.14 \text{ mas } M_{\odot}^{-1}$ . It is also instructive

<sup>3</sup>This form for the bending angle can be derived heuristically by assuming that a photon passing by an object of mass  $M$  at a distance  $b \equiv D_l \theta$  will experience an impulse given by the Newtonian acceleration  $GM/b^2$  over a time  $2b/c$ , thereby inducing a velocity perpendicular to the original trajectory of  $\delta v = (GM/b^2)(2b/c) = 2GM/(bc)$ . The deflection is then  $\delta v/c = 2GM/(bc^2)$ . The additional factor of two cannot be derived classically, and arises from General Relativity (see, e.g., Schneider *et al.* 1992).

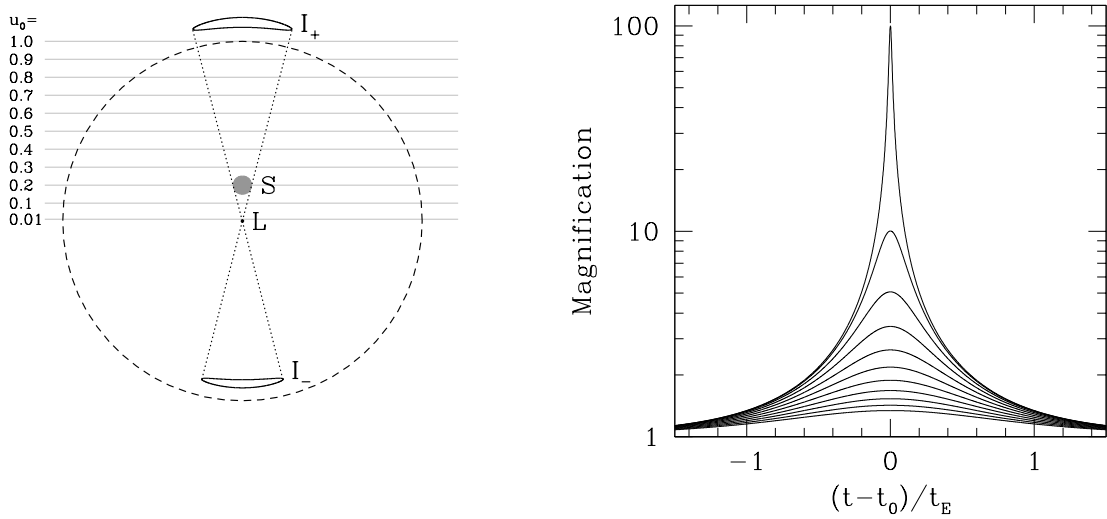


Fig. 3.— Basic point-mass microlensing. (Left) All angles are normalized by the angular Einstein ring radius  $\theta_E$ , shown as a dashed circle of radius  $\theta_E$ . The source (S) is located at an angular separation of  $u = 0.2$  from the lens (L). Two images are created, one image outside the Einstein ring ( $I_+$ ), on the same side of the lens as the source with position from the lens of  $y_+ = 0.5(\sqrt{u^2 + 4} + u)$ , and one inside the Einstein ring, on the opposite side of the lens as the source with position from the lens of  $y_- = -0.5(\sqrt{u^2 + 4} - u)$ . The images are compressed radially but elongated tangentially. Since surface brightness is conserved, the magnification of each image is just the ratio of its area to the area of the source. Since the images are typically unresolved, only the total magnification of the two images is measured, which depends only on  $u$ . (Right) Magnification as a function of time (light curves), for the ten trajectories shown in the left panel with impact parameters  $u_0 = 0.01, 0.1, 0.2, \dots, 1.0$ . Time is relative to the time  $t_0$  of the peak of the event (when  $u = u_0$ ), and in units of the angular Einstein crossing time  $t_E$ . Higher magnification implies more elongated images, which leads to increased sensitivity to planetary companions. Adapted from *Paczynski 1996*.

to note that  $\theta_E = \sqrt{2R_{Sch}/D_{rel}}$ , where  $R_{Sch} \equiv 2GM/c^2$  is the Schwarzschild radius of the lens. Quantitatively,

$$\theta_E = 550 \text{ mas} \left( \frac{M}{0.3 M_\odot} \right)^{1/2} \left( \frac{\pi_{rel}}{125 \mu\text{as}} \right)^{1/2}, \quad (2)$$

which corresponds to a physical Einstein ring radius at the distance of the lens of,

$$\begin{aligned} r_E &\equiv \theta_E D_l \\ &= 2.2 \text{ AU} \left( \frac{M}{0.3 M_\odot} \right)^{1/2} \left( \frac{D_s}{8 \text{ kpc}} \right)^{1/2} \left[ \frac{x(1-x)}{0.25} \right]^{1/2} \end{aligned} \quad (3)$$

where  $x \equiv D_l/D_s$ .

Normalizing all angles on the sky by  $\theta_E$ , we can define  $u = \beta/\theta_E$  and  $y = \theta/\theta_E$ . Using these definitions and the definition for  $\theta_E$ , the lens equation (1) reduces to the form

$$u = y - y^{-1}. \quad (5)$$

This is equivalent to a quadratic equation in  $y$ :  $y^2 - uy - 1 = 0$ . Thus in the case of imperfect alignment ( $u \neq 0$ ), there are two images, with positions

$$y_{\pm} = \pm \frac{1}{2}(\sqrt{u^2 + 4} \pm u). \quad (6)$$

The positive, or “major” image is always outside the Einstein ring, whereas the negative, or “minor” image is al-

ways inside the Einstein ring<sup>4</sup>. As can be seen in Figure 3, the angular separation between these images at the time of closest alignment is  $\sim 2\theta_E$ . Thus for typical lens masses ( $0.1 - 1 M_\odot$ ) and lens and source distances ( $1 - 10 \text{ kpc}$ ),  $\theta_E \lesssim \text{mas}$  and so the images are not resolved. However, the images are also distorted, and since surface brightness is conserved, this implies they are also magnified. The magnification of each image is just the ratio of the area of the image to the area of the source. As can be seen in Figure 3, the images are typically elongated tangentially by an amount  $y_{\pm}/u$ , but are compressed radially by an amount  $dy_{\pm}/du$ . The magnifications are then

$$A_{\pm} = \left| \frac{y_{\pm}}{u} \frac{dy_{\pm}}{du} \right| = \frac{1}{2} \left[ \frac{u^2 + 2}{u\sqrt{u^2 + 4}} \pm 1 \right], \quad (7)$$

<sup>4</sup>The images formed by a gravitational lens can also be found by determining the relative time delay as a function of the (vector) angle  $\theta$  for hypothetical light rays propagating from the source. This time delay function includes the effect of the difference in the geometric path length, as well the gravitational (Shapiro) delay, as a function of  $\theta$ . The images are then located at the stationary points (maxima, minima, or saddle points) of the time delay surface. For a point-mass lens, the positive solution in Equation 6 corresponds to a minimum in the time delay surface, and so is also referred to as the “minimum” image. The negative solution corresponds to a saddle point, and so is also referred to as the “saddle” image. There is formally a third image, corresponding to the maximum of the time delay surface, but this image is located behind the lens, and is infinitely demagnified (for a true point lens).

and thus the total magnification is

$$A(u) = \frac{u^2 + 2}{u\sqrt{u^2 + 4}}. \quad (8)$$

Note that, as  $u \rightarrow \infty$ ,  $A_+ \rightarrow 1$  and  $A_- \rightarrow 0$ . Also, for  $u \ll 1$ , the magnification takes the form  $A \simeq 1/u$ .

Because the lens, source, and observer are all in relative motion, the angular separation between the lens and source is a function of time. Therefore, the magnification of the source is also a function of time: a microlensing event. In the simplest case of uniform, rectilinear motion, the relative lens-source motion can be parametrized by

$$u(t) = \left[ u_0^2 + \left( \frac{t - t_0}{t_E} \right)^2 \right]^{1/2}, \quad (9)$$

where  $u_0$  is the minimum separation between the lens and source (in units of  $\theta_E$ ),  $t_0$  is the time of maximum magnification (corresponding to when  $u = u_0$ ), and  $t_E$  is the time scale to cross the angular Einstein ring radius,  $t_E \equiv \theta_E / \mu_{\text{rel}}$ , where  $\mu_{\text{rel}}$  is the proper motion of the source relative to the lens. This form for  $u$  gives rise to a smooth, symmetric microlensing event with a characteristic form (often called a ‘‘Paczynski curve’’), as shown in the right panel of Figure 3. The typical timescales for events toward the Galactic bulge are of order a month,

$$t_E = 19 \text{ d} \left( \frac{M}{0.3 M_\odot} \right)^{1/2} \left( \frac{\pi_{\text{rel}}}{125 \mu\text{as}} \right)^{1/2} \left( \frac{\mu_{\text{rel}}}{10.5 \text{ mas/yr}} \right)^{-1} \quad (10)$$

but can range from less than a day to years. The magnification is  $A > 1.34$  for  $u \leq 1$ , and so the magnifications are substantial and easily detectable.

If the lens star happens to have a planetary companion, and the planet happens to be located near the paths of one or both of the two images created by the primary lens, the companion can create a short-timescale perturbation on the primary microlensing event when the image(s) sweep by the planet (Mao & Paczynski 1991; Gould & Loeb, 1992). There are two conceptually different channels by which planets can be detected with microlensing, delineated by the maximum magnification  $A_{\text{max}}$  of the primary event in which the planet is detected.

Consider the case of a relatively low-magnification (i.e.,  $A_{\text{max}} \lesssim 10$  or  $u_0 \gtrsim 0.1$ ) primary event, such as illustrated in Figure 1. Over the course of the primary event, the two images sweep out a path on the sky, with the path of the major (minimum) image entirely contained outside the Einstein ring radius, and the path of the minor (saddle) image entirely contained within the Einstein ring radius. In the main detection channel, the primary hosts a planet which happens to be located near the path of one<sup>5</sup> of these two images for such a low-magnification event. As the image

sweeps by the position of the planet, the planet will further perturb the light from this image and yield a short-timescale deviation (Gould & Loeb, 1992). The duration of this deviation is  $\sim t_{E,p} = q^{1/2} t_E$ , where  $q = m_p/M$  is the mass ratio and  $m_p$  is the planet mass, and the magnitude of the perturbation depends on how close the perturbed image passes by the planet. Given a range of primary event durations of  $\sim 10 - 100$  days, the duration of the perturbations range from a few hours for an Earth-mass planet to a few days for Jovian-mass planets. As can be seen in Figure 2, the location of the perturbation relative to the peak of the primary event depends on two parameters:  $\alpha$ , the angle of the projected star-planet axis with respect to the source trajectory<sup>6</sup>, and  $d$ , the instantaneous angular separation between the planet and host star in units of  $\theta_E$ .

Because the orientation of the source trajectory relative to the planet position is random, the time of this perturbation is not predictable and the detection probability is  $\sim A(t_{0,p})\theta_{E,p}/\theta_E$ , where  $A(t_{0,p})$  is the unperturbed magnification of the image that is being perturbed at the time  $t_{0,p}$  of the perturbation (Horne et al., 2009), and  $\theta_{E,p} \equiv q^{1/2}\theta_E$  is the Einstein ring radius of the planet. Here the factor  $A$  accounts for the fact that the area of the image plane covered by magnified images is larger by their magnification.

Since the planet must be located near one of the two primary images in order to yield a detectable deviation, and these images are always located near the Einstein ring radius when the source is significantly magnified (see Figure 1), the sensitivity of the microlensing method peaks for planet-star projected separations of  $\sim r_E$ , i.e., for  $d \sim 1$ . However, microlensing can also detect planets well outside the Einstein ring ( $d \gg 1$ ), albeit with less sensitivity. Since the magnification of the minor image decreases with position as  $y_-^4$  (see Equations 6 and 7), microlensing is generally not sensitive to planets  $d \ll 1$ , i.e., close-in planets.

Given the existence of a planet with a projected separation within a factor of  $\sim 2$  of the Einstein ring radius, the detection probabilities range from tens of percent for Jovian planets to a few percent for Earth-mass planets (Gould & Loeb, 1992; Bolatto & Falco, 1994; Bennett & Rhie, 1996; Peale, 2001). Detecting planets via the main channel requires substantial commitment of resources because the unpredictable nature of the perturbation requires dense, continuous sampling, and furthermore the detection probability per event is relatively low so many events must be monitored.

A useful feature of low-magnification planetary microlensing events such as that shown in Figure 1 is that it is possible to essentially ‘read off’ the light curve parameters from the observed features (Gould & Loeb, 1992; Gaudi & Gould, 1997b). For the primary event, the three gross observable parameters are the time of maximum magnifica-

<sup>5</sup> As can be seen in Figure 1, for low-magnification events, the two images are well-separated, and thus a low mass ratio planet will generally only significantly perturb one of the two images.

<sup>6</sup> Conventionally, both the lensing deflection angle and the source trajectory angle are denoted by the symbol  $\alpha$ . In order to maintain contact with the literature, this unfortunate convention is maintained here, but to avoid confusion the deflection angle is denoted with the subscript ‘‘d’’.

tion  $t_0$ , the peak magnification  $A_{\max}$ , and a measure of the duration of the event such as its full-width half-maximum  $t_{FWHM}$ . The latter two observables can then be related to the Einstein timescale  $t_E$  and impact parameter  $u_0$  using Equations 8 and 9<sup>7</sup>. For example, for small  $u_0$  we have  $u_0 \sim A_{\max}^{-1}$  and  $t_E \sim 0.5t_{FWHM}u_0^{-1}$ . Unfortunately, only  $t_E$  contains any information about the physical properties of the lens, and then only in a degenerate combination of the lens mass, distance, and relative lens-source proper motion. However, as discussed in detail in Section 3.3, in many cases it is often possible to obtain additional information which partially or totally breaks this degeneracy. In particular, in those cases where it is possible to isolate the light from the lens itself, this measurement can be used to constrain the lens mass (Bennett *et al.*, 2007). The three parameters that characterize the planetary perturbation are the duration of the perturbation, the time of the perturbation  $t_{0,p}$ , and the magnitude of the perturbation,  $\delta_p$ . As mentioned previously, the duration of the perturbation is proportional to  $t_{E,p} \equiv q^{1/2}t_E$ , and so gives the planet/star mass ratio  $q$ . The time and magnitude of the perturbation then specify the projected separation  $d$  and angle of the source trajectory with respect to the binary axis  $\alpha$ , since  $t_{0,p}$  and  $\delta_p$  depend on the location of the planet relative to the path of the perturbed image (Gaudi & Gould, 1997b).

The other channel by which microlensing can detect planets is in high magnification events (Griest & Safizadeh, 1998)<sup>8</sup>. In addition to perturbing images that happen to pass nearby, planets will also distort the perfect circular symmetry of the Einstein ring. Near the peak of high-magnification events, as the lens passes very close to the observer-source line of sight (i.e. when  $u \ll 1$ ), the two primary images are highly elongated and sweep along the Einstein ring, thus probing this distortion. For very high-magnification events, these images probe nearly the entire Einstein ring radius and so are sensitive to all planets with separations near  $r_E$ , regardless of their orientation with respect to the source trajectory. Thus high-magnification events can have nearly 100% sensitivity to planets near the Einstein ring radius, and are very sensitive to low-mass planets (Griest & Safizadeh, 1998). However, these events are rare: a fraction  $\sim 1/A_{\max}$  of events have maximum magnification  $\gtrsim A_{\max}$ . Fortunately, these events can often be predicted several hours to several days ahead of peak, and furthermore the times of high sensitivity to planets are within a full-width half-maximum of the event peak, or roughly a day for typical high-magnification events (Rattenbury *et al.*, 2002). Thus scarce observing resources can be concentrated on these few events and only during the times of maximum sensitivity. Because the source stars are highly magnified, it is also possible to use more common, smaller-

aperture telescopes.

## 2.2. Theory of Microlensing

Gravitational lensing can be thought of as the mapping  $\beta \rightarrow \theta$  between the angular position of a source  $\beta$  in the absence of lensing to the angular position(s)  $\theta$  of the image(s) of the source under the action of the gravitational lens. This mapping is given by the lens equation,

$$\beta = \theta - \alpha_d(\theta), \quad (11)$$

where  $\alpha_d$  is deflection of the source due to the lens.

Consider a source at a distance  $D_s$  and a lens located at a distance  $D_l$  from the observer. Figure 2 shows the lensing geometry. The deflection angle  $\alpha_d$  is related to the angle  $\hat{\alpha}_d$  by which the lens mass bends the light ray from the source by  $\hat{\alpha}_d(D_s - D_l) = \alpha_d D_s$ . Assume the lens is a system of  $N_L$  point masses each with mass  $m_i$  and position  $\theta_{m,i}$ . Further assume that the lenses are static (or, more precisely, moving much more slowly than  $c$ ), and their distribution along the line of sight is small in comparison to  $D_l$ ,  $D_s$ , and  $D_s - D_l$ . The deflection angle is then,

$$\alpha_d(\theta) = \frac{4G}{D_{\text{rel}}c^2} \sum_i^{N_L} m_i \frac{\theta - \theta_{m,i}}{|\theta - \theta_{m,i}|^2}, \quad (12)$$

where  $D_{\text{rel}} \equiv (D_l^{-1} - D_s^{-1})^{-1}$ . See Schneider *et al.* (1992) and Petters *et al.* (2001) for the expression for  $\alpha_d$  for a general mass distribution, as well for the derivation of Equations 11 and 12 from the time delay function and ultimately the metric.

It is common practice to normalize all angles to the angular Einstein ring radius,

$$\theta_E \equiv (\kappa M \pi_{\text{rel}})^{1/2}, \quad (13)$$

where  $M \equiv \sum_i^{N_L} m_i$  is the total mass of the lens,  $\pi_{\text{rel}} \equiv \text{AU}/D_{\text{rel}}$  is the relative lens-source parallax, and  $\kappa = 4G/(c^2 \text{AU}) \simeq 8.14 \text{ mas } M_{\odot}^{-1}$ . The reason for this convention is clear when considering the single lens (Section 2.2.1). The dimensionless vector source position is defined to be  $\mathbf{u} \equiv \beta/\theta_E$ , and the dimensionless vector image positions are defined to be  $\mathbf{y} \equiv \theta/\theta_E$ .

It is often convenient to write the lens equation in complex coordinates (Witt, 1990). Defining the components of the (dimensionless) source position to be  $\mathbf{u} = (u_1, u_2)$  and the image position(s) to be  $\mathbf{y} = (y_1, y_2)$ , the two-dimensional source and images positions can be expressed in complex form as,  $\zeta = u_1 + iu_2$  and  $z = y_1 + iy_2$ . The lens equation can now be rewritten

$$\zeta = z - \sum_i^{N_L} \frac{\epsilon_i}{\bar{z} - \bar{z}_{m,i}}, \quad (14)$$

where  $z_{m,i}$  is the position of mass  $i$ ,  $\epsilon \equiv m_i/M$ . The overbars denote complex conjugates, which in Equation 14 arise from the identity  $z/|z|^2 \equiv \bar{z}^{-1}$ . This equation can then be solved to find the image positions  $z_j$ .

<sup>7</sup>For the purposes of exposition, this discussion ignores blending, which is generally important and complicates the interpretation of observed light curves. See Section 3.1.

<sup>8</sup>There is no formal definition for ‘high’-magnification events, however typically high-magnification refers to events with maximum magnification  $A_{\max} \gtrsim 100$ , corresponding to impact parameters  $u_0 \lesssim 0.01$ .

Lensing conserves surface brightness, but because of the mapping the angular area of each image of the source is not necessarily equal to angular area of the unlensed source. Thus the flux of each image (the area times the surface brightness) is different from the flux of the unlensed source: the source is magnified or demagnified. For a small source, the magnification  $A_j$  of each image  $j$  is given by the amount the source is “stretched” due to the lens mapping. Mathematically, the amount of stretching is given by the inverse of the determinant of the Jacobian of the mapping (14) evaluated at the image position,

$$A_j = \frac{1}{\det J} \bigg|_{z=z_j}, \quad \det J \equiv \frac{\partial(x_1, x_2)}{\partial(y_1, y_2)} = 1 - \frac{\partial \zeta}{\partial \bar{z}} \frac{\partial \bar{\zeta}}{\partial z}. \quad (15)$$

See Witt (1990) for a derivation of the rightmost equality. Note that these magnifications can be positive or negative, where the sign corresponds to the parity (handedness) of the image. By definition in microlensing the images are unresolved, and we are interested in the total magnification which is just the sum of the magnifications of the individual images,  $A \equiv \sum_j |A_j|$ .

An interesting and critical property of gravitational lenses is that the mapping can be singular for some source positions. At these source positions,  $\det J = 0$ . In other words, an infinitesimally small displacement in the source position maps to an infinitely large separation in the image position<sup>9</sup>. For point sources at these positions, the magnification is formally infinite, and for sources near these positions, the magnification is large.

From the lens equation (14),

$$\frac{\partial \zeta}{\partial \bar{z}} = \sum_i^{N_l} \frac{\epsilon_i}{(\bar{z}_{m,i} - \bar{z})^2}, \quad (16)$$

and therefore, from equation (15), the image positions where  $\det J = 0$  are given by,

$$\left| \sum_i^{N_l} \frac{\epsilon_i}{(\bar{z}_{m,i} - \bar{z})^2} \right|^2 = 1. \quad (17)$$

The set of all such image positions define closed *critical curves*. These can be found by noting that the sum in Equation 17 must have a modulus equal to unity. Therefore, we can solve for the critical image positions parametrically by solving the equation

$$\sum_i^{N_l} \frac{\epsilon_i}{(\bar{z}_{m,i} - \bar{z})^2} = e^{i\phi}, \quad (18)$$

for each value of the parameter  $\phi = [0, 2\pi)$ . The set of source positions corresponding to these image positions define closed curves called *caustics*. By clearing the complex

conjugates  $\bar{z}$  and fractions (Witt, 1990), Equation 18 can be written as a complex polynomial of degree  $2N_l$ , there are at most  $2N_l$  critical curves and caustics. Given their importance in planetary microlensing, caustics are discussed in considerably more detail below.

### 2.2.1. Single Lenses

For a single point mass ( $N_l = 1$ ), defining the origin as the position of the lens, the lens equation reduces to,

$$\beta = \theta - \frac{\theta_E^2}{\theta}. \quad (19)$$

Since the lens is circularly symmetric, the images are always located along the line connecting the lens and source, and the vector notation has been suppressed, but the convention that positive values of  $\theta$  are for images on the same side of the lens as the source is kept. If the lens is perfectly aligned with the source, then  $\beta = 0$ , and  $\theta = \theta_E$ . In other words, the lens images the source into a ring of radius equal to the angular Einstein ring radius.

The dimensionless single lens equation is,

$$u = y - \frac{1}{y}. \quad (20)$$

In the case of imperfect alignment, this becomes a quadratic function of  $y$ , and so there are two images of the source, with positions,

$$y_{\pm} = \pm \frac{1}{2} \left( \sqrt{u^2 + 4} \pm u \right). \quad (21)$$

One of these images (the major image, or minimum) is always outside the Einstein ring radius ( $y_+ \geq 1$ ) on the same side of the lens as the source, and the other image (the minor image, or saddle point) is always inside the Einstein ring radius ( $|y_-| \leq 1$ ) on the opposite side of the lens as the source. The separation between the two images is  $|y_+ - y_-| = (u^2 + 4)^{1/2}$ , and thus the images are separated by  $\sim 2\theta_E$  when both images are significantly magnified (i.e. when  $u \lesssim 1$ ). Since  $\theta_E$  is of order a milliarcsecond for typical lens masses, and source and lens distances in events toward the Galactic bulge, the images are unresolved.

The magnifications of each image can be found analytically,

$$A_{\pm} = \frac{1}{2} (A \pm 1) \quad (22)$$

where the total magnification is,

$$A(u) = \frac{u^2 + 2}{u\sqrt{u^2 + 4}}. \quad (23)$$

A few properties are worth noting. First,  $u \ll 1$ ,  $A(u) \simeq u^{-1}$ . The magnification diverges for  $u \rightarrow 0$ , and the point  $u = 0$  defines the caustic in the single lens case. Second, for  $u \gg 1$ ,  $A(u) \simeq 1 + 2u^{-4}$ , and thus the excess magnification drops rapidly for large source-lens angular separations.

<sup>9</sup>This is analogous to the familiar distortion seen in cylindrical map projections of the globe (such as the Mercator projection) for latitudes far from the equator, due to the singular nature of these mappings at the poles.

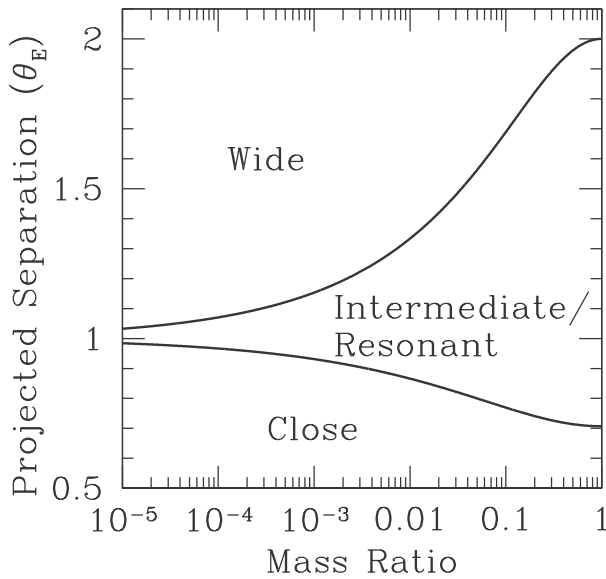


Fig. 4.— The critical values of  $d$ , the projected separation in units of  $\theta_E$ , at which the caustic topology (number of caustic curves) of a binary lens changes as a function of the mass ratio  $q$ . The upper curve shows  $d_w$ , the critical value of  $d$  between the wide caustic topology consisting of two disjoint caustics, and the intermediate or resonant caustic topology consisting of a single caustic. The lower curve shows  $d_c$ , the critical value between the resonant caustic topology and the close caustic topology consisting of three disjoint caustics.

### 2.2.2. Binary Lenses

For a two point-mass lens ( $N_l = 2$ ), the lens equation is,

$$\zeta = z + \frac{\epsilon_1}{\bar{z}_{m,1} - \bar{z}} + \frac{\epsilon_2}{\bar{z}_{m,2} - \bar{z}}. \quad (24)$$

This can be written as a fifth-order complex polynomial in  $z$ , which cannot be solved analytically. Witt & Mao, 1995 provide the coefficients of the polynomial. It can easily be solved with standard numerical routines, e.g., Laguerre’s method (Press et al., 1992), to yield the image positions  $z$ . It is important to note that the solutions to the fifth-order complex polynomial are not necessarily solutions to the lens equation (Equation 24). Depending on the location of the source with respect to the lens positions, two of the images can be spurious. Thus there are either three or five images.

The boundaries of the three and five image regions are the caustic curves (where  $\det J = 0$ ), and thus the number of images changes by two when the source crosses the caustic. A binary lens has one, two, or three closed and non-self-intersecting caustic curves. Which of these three topologies is exhibited depends on the mass ratio of the lens  $q \equiv m_1/m_2$  and on the angular separation of the two lens components in units of Einstein ring radius of binary,  $d \equiv |z_{m,1} - z_{m,2}|$ . For a given  $q$ , the values of  $d$  for which the topology changes are given by (Schneider &

Weiss, 1986; Dominik, 1999b),

$$\frac{q}{(1+q)^2} = \frac{(1-d_c)^3}{27d_c^8}, \quad d_w = \frac{(1+q^{1/3})^{3/2}}{(1+q)^{1/2}}. \quad (25)$$

For  $d \leq d_c$ , there are three caustic curves, for  $d_c \leq d \leq d_w$ , there is one caustic curve, and for  $d \geq d_w$ , there are two caustic curves. These are often referred to as the “close”, “intermediate” or “resonant”, and “wide” topologies, respectively. Figure 4 plots  $d_c$  and  $d_w$  as a function of  $q$ . For equal-mass binaries,  $q = 1$ , the critical values of the separation are  $d_c = 2^{-1/2}$  and  $d_w = 2$ .

A useful property of binary lenses is that the total magnification of all the images is always  $A \geq 3$  when the source is interior to the caustic curve, i.e., when there are five images of the source (Witt & Mao, 1995). Thus if the magnification of a source is observed to be less than 3 during a microlensing event, it can be immediately concluded that either the source is exterior to the caustic, or the source is significantly blended with an unrelated, unlensed star<sup>10</sup>, thus diluting the magnification.

### 2.2.3. Triple Lenses and Beyond

For a triple lens ( $N_l = 3$ ), the lens equation can be written a tenth-order complex polynomial in  $z$  (Gaudi et al., 1998), which can be solved using the same techniques as in the binary lens case. Rhie, 2002 provides the coefficients of the polynomial. There are a maximum of ten images, and there are a minimum of four images, with the number of images changing by a multiple of two when the source crosses the caustic. The caustics of triple lenses can exhibit quite complicated topologies, including nested and/or self-intersecting caustic curves. The topology depends on five parameters: two mass ratios, two projected separations, and the angle between projected position vectors of the companions and the primary lens.

In general, the lens equation for a system of  $N_l$  point lenses is can be written as a complex polynomial of order  $N_l^2 + 1$ . However, it has been shown that the maximum number of images is  $5(N_l - 1)$  for  $N_l \geq 2$  (Rhie, 2001, 2003; Khavinson & Neumann, 2006). Thus for  $N_l > 3$ , it is always the case that some of the roots of the polynomial are not solutions to the lens equation.

### 2.2.4. Magnification Near Caustics

As mentioned previously, the caustics are the set of source positions for which the magnification of a point source is formally infinite. Caustic curves are characterized by multiple concave segments called *folds* which meet at points called *cusps*. Folds and cusps are so named because the local lensing properties of sources close to these caustics are equivalent to the generic fold and cusp mapping singularities of mathematical catastrophe theory. For a more

<sup>10</sup>There is a third, less likely possibility that there are additional bodies in the system. In this case, the bound that  $A \geq 3$  interior to the caustic can be violated (Witt & Mao, 1995)

precise formulation of this statement and additional discussion, see *Petters et al.*, 2001. This leads to the particularly important property of fold and cusps that their local lensing properties are universal, regardless of the global properties of the lens. Thus the positions and magnifications of the critical images of sources near folds and cusps have universal scaling behaviors that can be described essentially analytically, and whose normalization depend only on the local properties of the lens potential. This universal and local behavior of the magnification near caustics has proven quite useful, in that it allows one to analyze light curves near caustic crossings separate from and independent of the global lens model (see, e.g., *Gaudi & Gould*, 1999, *Albrow et al.*, 1999b; *Rhie & Bennett*, 1999, *Afonso et al.*, 2001; *Dominik*, 2004a,b).

The lensing behavior near folds and cusps has been discussed in detail by a number of authors (*Schneider & Weiss*, 1986, 1992; *Mao*, 1992; *Zakharov*, 1995, 1999; *Fluke & Webster*, 1999; *Petters et al.*, 2001, *Gaudi & Petters*, 2002a,b; *Pejcha & Heyrovsky*, 2009). The salient properties are briefly reviewed here, but the reader is encouraged to consult these papers for a more in-depth discussion.

For sources close to and interior<sup>11</sup> to a fold caustic, there are two highly-magnified images with nearly equal magnification and opposite parity that are nearly equidistant from the corresponding critical curve. Neglecting the curvature of the caustic and any changes in the lensing properties parallel to the caustic, the total magnification of these divergent images is (*Schneider & Weiss*, 1986),

$$A_{\text{div}}(\Delta u_{\perp}) = \left( \frac{\Delta u_{\perp}}{u_r} \right)^{-1/2} \Theta(\Delta u_{\perp}), \quad (26)$$

where  $\Delta u_{\perp}$  is the perpendicular distance to the caustic, with  $\Delta u_{\perp} > 0$  for sources interior to the caustic,  $\Theta(x)$  is the Heaviside step function, and  $u_r$  is the characteristic ‘strength’ of the fold caustic locally, and is related to local derivatives of the lens potential. As the source approaches the caustic, the images brighten and merge, disappearing when the source crosses the caustic. The behaviors of the remaining (non-critical) images are continuous as the source crosses the caustic. Thus immediately outside of a fold, the magnification is finite and (typically) modest.

For sources close to and interior to a cusp, there are three highly-magnified images. For a source on the axis of symmetry of the cusp, the total magnification of the three images is  $\propto \Delta u_c^{-1}$ , where  $\Delta u_c$  is the distance of the source from the cusp. As the source approaches the cusp, the magnification of all three images increases and the images merge. Two of the three images disappear as the source exits the cusp. The magnification of the remaining image is continuous as the source exits the cusp, and in particular the image remains highly magnified, also with magnification which is  $\propto \Delta u_c^{-1}$ . Thus, in contrast to folds, sources

immediately exterior to cusps are highly magnified. As with the fold, the behaviors of the non-critical images are continuous as the source crosses the caustic.

Caustic curves are closed, and thus for any given source trajectory (which is simply a continuous path through the source plane), caustic crossings come in pairs. Generally, since the majority of the length of a caustic is made up of fold caustics, both the caustic entry and exit are fold crossings. Since the magnification immediately outside of a fold is not divergent, it is usually impossible to predict a caustic entry beforehand. Once one sees a fold caustic entry, a caustic exit is guaranteed, and this is typically a fold exit. Monitoring a caustic exit is useful for two reasons. First, the strong finite source effects (see below) during the crossing can be used to provide additional information about the lens (see Section 3.3), and measure the limb-darkening of the source (e.g., *Albrow et al.*, 1999c; *Fields et al.*, 2003). In addition, during the caustic crossing the source is highly magnified and potentially very bright, which allows for otherwise impossible spectroscopic observations to determine properties of the source star, such as its effective temperature and atmospheric abundances (*Minniti et al.*, 1998; *Johnson et al.*, 2008). Unfortunately, it is typically difficult to predict when this exit will happen well before the crossing (*Jaroszynski & Mao*, 2001).

For both fold and cusp caustics, the magnification of a source of finite size begins to deviate by more than a few percent from the point-source approximation when the center of the source is within several source radii of the caustic (*Pejcha & Heyrovsky*, 2009). Formally, the magnification of a finite source can be found simply by integrating the point-source magnification over of source, weighting by the source surface brightness distribution. Practically, this approach is difficult and costly to implement precisely due to the divergent magnification near the caustic curves. An enormous amount of effort has been put into developing robust and efficient algorithms to compute the magnification for finite sources (*Dominik*, 1995, 2007; *Wambsganss*, 1997; *Gould & Gauchere*, 1997; *Griest & Safizadeh*, 1998; *Vermaak*, 2000; *Dong et al.*, 2006; *Gould*, 2008; *Pejcha & Heyrovsky*, 2009; *Bennett*, 2009b). The most efficient of these algorithms use a two-pronged approach. First, semi-analytic approximations to the finite-source magnification derived from an expansion of the magnification in the vicinity of the source are used where appropriate (*Gould*, 2008; *Pejcha & Heyrovsky*, 2009). Second, where necessary a full numerical evaluation of the finite source magnification is performed by integrating in the image plane. Integrating in the image plane removes the difficulties with the divergent behavior of the magnification near caustics, because the surface brightness profiles of the images are smooth and continuous. Thus one simply ‘shoots’ rays in the image plane, and determines which ones ‘land’ on the source using the lens equation. The ratio of the total area of all the images divided by the area of the source (appropriately weighted by the surface brightness profile of the source) gives the total magnification. The devilish details then lie in the manner

<sup>11</sup> Here interior to a fold caustic is defined such that the caustic curves away from the source.

in which one efficiently samples the image plane (see e.g., *Rattenbury et al.*, 2002; *Dong et al.*, 2006; *Pejcha & Heyrovsky*, 2009; *Bennett*, 2009b).

For planetary microlensing events, efficient routines for evaluating the finite-source magnification are crucial, for two reasons. First, nearly all planetary perturbations are strongly affected by finite source effects. Second, the processes of finding the best-fit model to an observed light curve and evaluating the model parameter uncertainties requires calculating tens of thousands of trial model curves (or more), and the majority of the computation time is spent calculating the finite-source magnifications.

### 2.3. Planetary Microlensing Phenomenology

For binary lenses in which the companion mass ratio is  $q \ll 1$  (i.e., planetary companions), the companion will cause a small perturbation to the overall magnification structure of the lens. Thus the majority of source positions will give rise to magnifications that are essentially indistinguishable from a single lens. The source positions for which the magnification deviates significantly from a single lens are all generally confined to a relatively narrow region around the caustics. Thus much of the phenomenology of planetary microlensing can be understood by studying the structure of the caustics and the magnification pattern near the caustics.

Recall there are three different caustic topologies for binary lenses: close, intermediate, and wide (See Figure 4). For  $q \ll 1$ , the critical values of the separation where these caustic topologies change can be approximated by  $d_c \simeq 1 - 3q^{1/3}/4$  and  $d_w \simeq 1 + 3q^{1/3}/2$  (*Dominik*, 1999b). Therefore, for planetary lenses, the intermediate or resonant caustics are confined to a relatively narrow range of separations near  $d = 1$ , and this range shrinks as  $q^{1/3}$ . Figure 5 shows the caustics for a Jupiter/Sun mass ratio of  $q = 0.001$ , and 11 different separations  $d = 0.6, 0.7, 0.8, 0.9, 0.95, 1.0, 1.05, 1.11, 1.25, 1.43, 1.67$ .

For both the close ( $d < d_c$ ; Figure 5i-k) and wide ( $d > d_w$ ; Figure 5a-c) topologies, one caustic is always located near the position of the primary (the origin in Figure 5). This is known as the central caustic. Figure 6 shows an expanded view of these caustics, which have a highly asymmetric ‘arrow’ shape, with one cusp at the arrow tip pointing toward the planet, and three cusps at the ‘back end’ of the caustic pointing away from the planet. The on-axis cusp pointing away from the planet is generally much ‘weaker’ than the other cusps, in the sense that the scale of the gradient in magnification along the cusp axis is smaller for the weaker cusp, so that at fixed distance from the cusp, the excess magnification is smaller for the weaker cusp. The magnification pattern near a central caustic is illustrated in Figure 7. The light curves (one-dimensional slices through the magnification pattern) for sources passing perpendicular to the binary-lens axis close the back-end will exhibit a ‘U’-shaped double-peaked deviation from the single-lens form (Figure 8c,d), whereas sources passing perpendicular

to the binary-lens axis close to the tip of the central caustic will exhibit a single bump (Figure 8b,d). Sources passing the caustic parallel to the binary-lens axis will exhibit little deviation from the single lens form, essentially unless they cross the caustic.

In the limit that  $q \ll 1$ , and  $|d - 1| \gg q$ , it is possible show that, for fixed  $d$ , the size of the central caustic scales as  $q$ . Furthermore, the overall shape of the caustic, as quantified, e.g., by its length-to-width ratio, depends only on  $d$ , such that the caustic becomes more asymmetric (the length-to-width ratio increases) as  $d \rightarrow 1$ . Finally, the central caustic shape and size is invariant under the transformation  $d \rightarrow d^{-1}$ . See *Chung et al.*, 2005 and Figure 6. As illustrated in Figure 8, the  $d \rightarrow d^{-1}$  duality results in a degeneracy between light curves produced by central caustic perturbations due to planetary companions, typically referred to as the close/wide degeneracy (*Griest & Safizadeh* 1999; *Dominik*, 1999b; *Albrow et al.*, 2000; *An*, 2005)

For the close ( $d < d_c$ ) topology (Figure 5h-j), there are three caustics, the central caustic and two larger, triangular-shaped caustics with three cusps. The latter caustics are referred to as the planetary caustics, and are centered on the planet/star axis at angular separation of  $u_c \simeq |d - d^{-1}|$  from the primary lens, on the opposite side of the primary from the planet<sup>12</sup>. The caustics are symmetrically displaced perpendicular to the planet/star axis, with the separation between the caustics increasing with decreasing  $d$  and so increasing  $u_c$ . As illustrated in Figure 7, the magnification pattern near these caustics is characterized by small regions surrounding the caustics where a source exhibits a positive deviation from the single lens magnification, and a large region between the caustics where a source exhibits a negative deviation from the single lens magnification. Figure 9c,d shows a representative light curve from a source passing near the planetary caustics of a close planetary lens with  $d = 0.8$  and  $q = 0.001$ .

For the wide ( $d > d_w$ ) topology (Figure 5h-j), there are two caustics, the central caustic and a single planetary caustic with four cusps. As for the close planetary caustics, the wide planetary caustic is centered on the planet/star axis at an angular separation of  $u_c \simeq |d - d^{-1}|$  from the primary lens, but in this case on the same side of the primary from the planet. The caustic is an asteroid shape, with the length along the planet/star axis being generally longer than the width. The asymmetry (i.e., length-to-width ratio) of the planetary caustic increases as  $d \rightarrow 1$ . The magnification pattern near the wide planetary caustic is characterized by large positive deviations interior to the caustic, and lobes

<sup>12</sup>It is possible to derive the location of the planetary caustic(s) for both the close and wide topologies by noting that, when the source crosses the planetary caustic(s), the planet is perturbing one of the two images of the source created by the primary lens (the major image in the case of the wide topology, and the minor image in the case of the close topology). For a source position  $u$ , the locations of the two primary images  $y_{\pm}(u)$  are given by Equation 21. The planet must therefore be located at  $d \sim y_{\pm}(u)$  to significantly perturb the image, and thus the center of caustic  $u_c$  is located at the solution of the inversion of Equation 21, i.e.,  $u(y_{\pm} = d)$ , which yields  $u_c = d - d^{-1}$ .

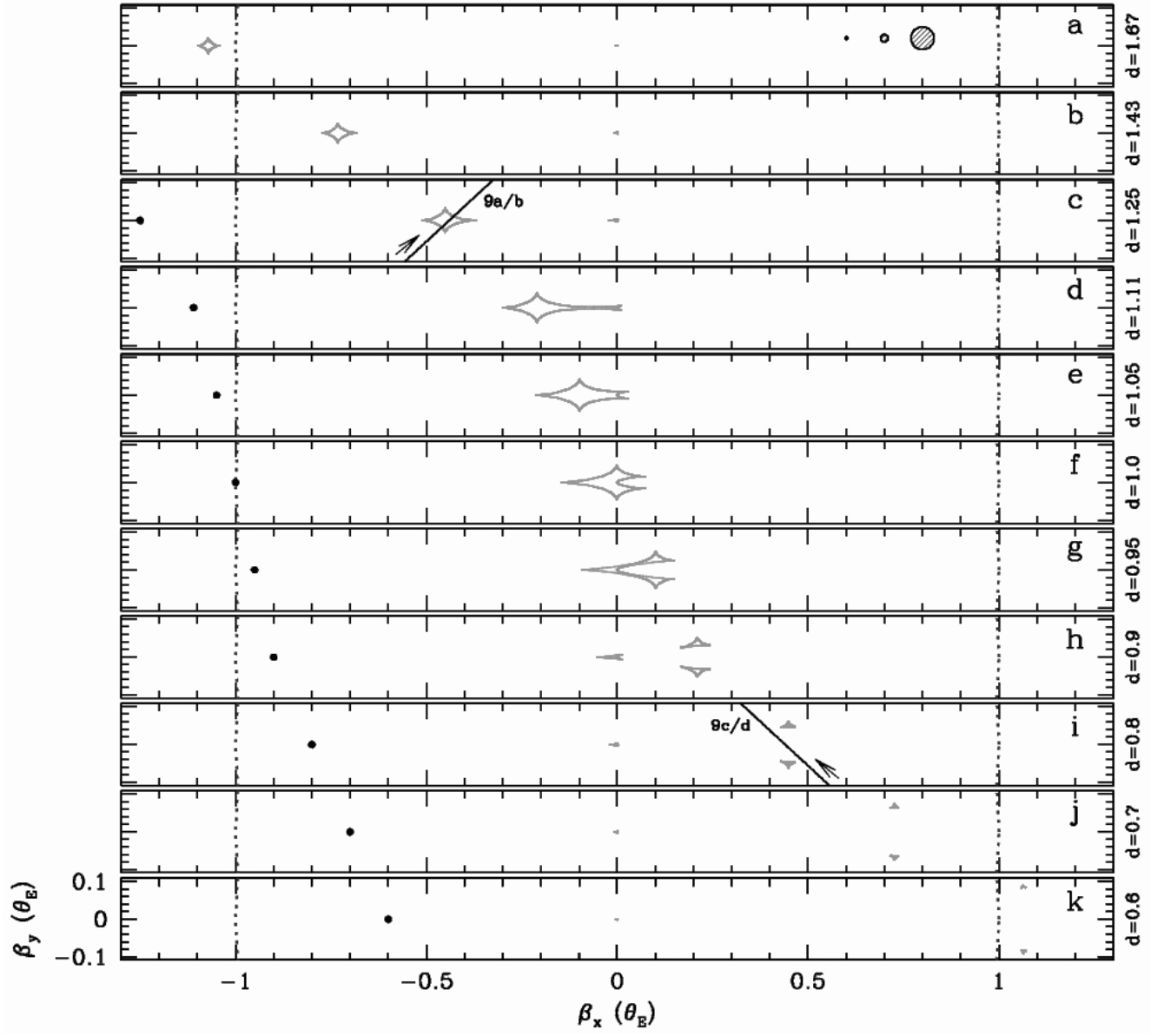


Fig. 5.— The grey curves show the caustics for a planetary lens with mass ratio  $q = 0.001$ , and various values of  $d$ , the projected separation in units of  $\theta_E$ . The dotted lines show sections of the Einstein ring. The dots show the location of the planet. In panels c and i, an example trajectory is shown which produces a perturbation by the planetary caustic; the resulting light curves are shown in Figure 9. In panel a, three different representative angular source sizes in units of  $\theta_E$  are shown,  $\rho_* = 0.003, 0.01$ , and  $0.03$ . For typical microlensing event parameters, these correspond to stars in the Galactic bulge with radii of  $\sim R_\odot, \sim 3R_\odot$ , and  $\sim 10R_\odot$ , i.e., a main-sequence turn-off star, a subgiant, and a clump giant.

of positive deviation extending outward along the axes of the four cusps, particularly along the planet/star axis in the direction of the primary. There are relatively small regions of slight negative deviation from the single-lens magnification immediately outside the fold caustic between the cusps. Figure 9a,b shows a representative light curve from a source passing through the planetary caustic of a wide planetary lens with  $d = 1.25$  and  $q = 0.001$ .

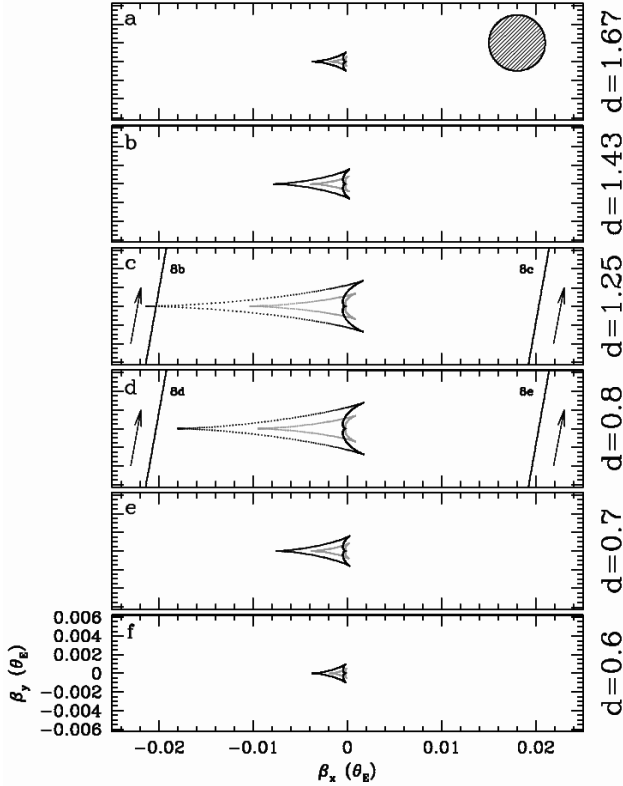


Fig. 6.— The black curves show the central caustics for a planetary lens with  $q = 0.001$ , and various values of  $d$ , the projected separation in units of  $\theta_E$ . The primary lens is located at the origin, and so trajectories which probe the central caustic correspond to events with small impact parameter  $u_0$ , or events with high maximum magnification. The grey curves show the central caustic for a mass ratio of  $q = 0.0005$ , demonstrating that the size of the central caustic scales as  $q$ . For  $q \ll 1$ , the central caustic and proximate magnification patterns are essentially identical under the transformation  $d \leftrightarrow d^{-1}$ . The degree of asymmetry, i.e. the length to width ratio, of the central caustic depends on  $d$ , such that the caustic becomes more asymmetric as  $d \rightarrow 1$ . In panels c and d, example trajectories are shown which produce perturbations by the central caustic; the resulting light curves are shown in Figure 8. In panel a, a representative angular source size in units of  $\theta_E$  of  $\rho_* = 0.003$  is shown. For typical microlensing event parameters, this correspond to a star in the Galactic bulge of radius  $\sim R_\odot$ , i.e., a main-sequence turn-off star.

In the wide ( $d > d_w$ ) and close ( $d < d_c$ ) cases, the planet is essentially perturbing one of the two images created by the primary lens, and the other image (on the other side of the Einstein ring) is essentially unaffected. In this case, and in the limit that  $q \rightarrow 0$ , the lensing behavior

near the planet and the perturbed primary image is equivalent to a single lens with pure external shear (Gould & Loeb, 1992; Dominik, 1999; Gaudi & Gould, 1997a), i.e., a Chang-Refsdal lens (Chang & Refsdal, 1979). The Chang-Refsdal lens has been studied extensively (e.g., Chang & Refsdal, 1984; An, 2005; An & Evans, 2006), and its properties are well-understood. The lens equation is,

$$\zeta = z - \frac{1}{z} - \gamma \bar{z}, \quad (27)$$

where  $\gamma$  is the shear and the origin is taken to be the location of the planet. This is equivalent to a fourth-order complex polynomial in  $z$ , which can be solved analytically, or numerically in the same manner as the binary-lens case (see Section 2.2). There are 2 or 4 images, depending on the source position. The correspondence between the Chang-Refsdal lens and the wide/close planetary case is achieved by setting  $\gamma = d^{-2}$  and choosing the origin of the binary lens to be  $d - d^{-1}$  from the primary lens, and including in the Chang-Refsdal approximation the magnification of the unperturbed image created by the primary on the other side of the Einstein ring. Note that  $\gamma > 1$  corresponds to the planetary caustics for the close topology, whereas  $\gamma < 1$  corresponds to the wide topology.

The properties of the caustics of a Chang-Refsdal lens (and thus the planetary caustics of wide/close planetary lenses) can be studied analytically. Based on expressions from Bozza, 2000, Han, 2006 has studied the scaling of the planetary caustics. The overall size of the wide ( $d > 1$ ) planetary caustic is approximately  $\propto q^{1/2} d^{-2}$ , and the length-to-width ratio is  $\sim 1 + d^{-2}$ . The shape is independent of  $q$  in this approximation. The overall size of the close ( $d < 1$ ) planetary caustics are approximately  $\propto q^{1/2} d^3$ , and their shape is also independent of  $q$ . The vertical separation between the two planetary caustics in the close topology is  $\propto q^{1/2} d^{-1}$ .

For the resonant case ( $d_c \leq d \leq d_w$ ) there exists a single, relatively large caustic with six cusps. For fixed  $q$ , the resonant caustic is larger than either the central or planetary caustics. The large size of these caustics results in a large cross-section and thus an enhanced detection probability. Indeed, in the first planet detected by microlensing, the source crossed a resonant caustic. The large size also means that the light curve deviation can last a significant fraction of the duration of the event. However, resonant caustics are also ‘weak’ in the sense that for a large fraction of the area interior to or immediate outside the caustic, the excess magnification relative to a single lens is small (see Figure 7). The exceptions to this are source positions in the vicinity the cusp located on the planet/star axis pointing toward the planet, and source positions near the ‘back end’ of the caustic near the position of the primary, which are characterized by large negative deviations relative to the single-lens magnification. The precise shape of the resonant caustic depends sensitively on  $d$ , and thus small changes in the value of  $d$  lead to large changes in the caustic morphology, as can be seen in Figure 5. As a result, the effects of

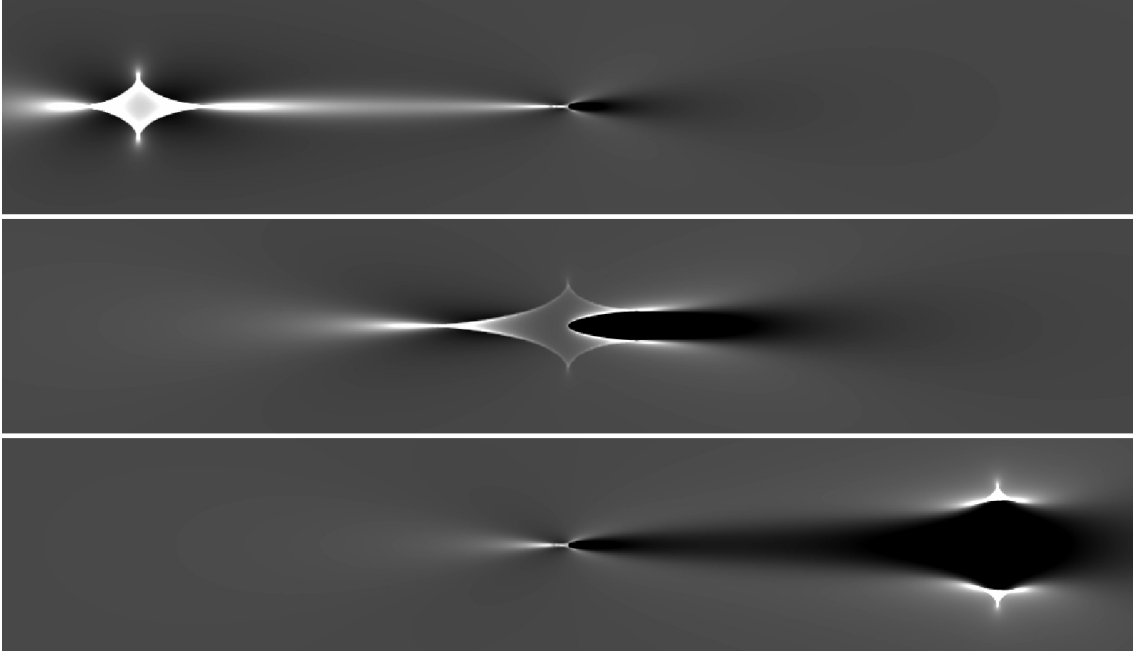


Fig. 7.— The magnification pattern as a function of source position for a planetary companion with  $q = 0.001$  and  $d = 1.25$  (top panel),  $d = 1.0$  (middle panel), and  $d = 0.8$  (bottom panel), corresponding to wide, intermediate/resonant, and close topologies, respectively. The greyscale shading denotes  $2.5 \log(1 + \delta)$ , where  $\delta$  is the fractional deviation from the single-lens (i.e., no planet) magnification. White shading corresponds to regions with positive deviation from the single lens magnification, whereas black shading corresponds to negative deviations. For the wide and close topology, there are two regions of large deviations, corresponding to the central caustics located at the position of the primary (the center of each panel), and the planetary caustics. For the intermediate/resonant topology, there is only one large caustic, which produces relatively weak perturbations for a large fraction of the caustic area.

orbital motion, which result in a change in  $d$  over the course of the event, are expected to be more important for resonant caustic perturbations. The size of resonant caustics scales as  $q^{1/3}$ , in contrast to planetary caustics, which scale as  $q^{1/2}$ , and central caustics, which scale as  $q$ .

### 3. PRACTICE OF MICROLENSING

#### 3.1. Light Curves and Fitting

The apparent relative motion between the lens and the source gives rise to a time-variable magnification of the source: a microlensing event. It is often (but not always, see Section 3.2) a good approximation that the source, lens, and observer are in uniform, rectilinear motion, in which case the angular separation between the lens and source as a function of time can be written as,

$$u(t) = (\tau^2 + u_0^2)^{1/2}, \quad (28)$$

where  $\tau \equiv (t - t_0)/t_E$ ,  $t_0$  is the time of closest alignment, which is also the time of maximum magnification,  $u_0$  is the impact parameter of the event, and  $t_E$  is the Einstein ring crossing time,

$$t_E \equiv \frac{\theta_E}{\mu_{\text{rel}}}, \quad (29)$$

where  $\mu_{\text{rel}}$  is the relative lens-source proper motion. Figure 3 shows the magnification as a function of time for a

microlensing event due to a single lens, with impact parameters of  $u_0 = 0.01, 0.1, 0.2, \dots, 0.9, 1.0$ , which serve to illustrate the variety of light curve shapes.

Of course, what is observed is not the magnification, but the flux of a photometered source as a function of time, which is given by,

$$F(t) = F_s A(t) + F_b. \quad (30)$$

Here  $F_s$  is the flux of the microlensing star, and  $F_b$  is the flux of any unresolved light (or “blended light”) that is not being lensed. The latter can include light from a companion to the source, light from unrelated nearby stars, light from a companion to the lens, and (most interestingly) light from the lens itself. Microlensing experiments are typically carried out toward crowded fields in order to maximize the event rate, and therefore one often finds unrelated stars blended with the microlensed source for typical ground-based resolutions of  $\sim 1''$ . Even in the most crowded bulge fields, most unrelated background stars are resolved at the resolution of the *Hubble Space Telescope* (*HST*). Figure 10 shows the fields of two events as observed from the ground with typical seeing, with *HST*, and with ground-based adaptive optics (AO).

The observed flux as a function of time for a microlensing event due to a single lens can be fit by five parameters:  $t_0, u_0, t_E, F_s$ , and  $F_b$ . It is important to note that several of these parameters tend to be highly degenerate. There

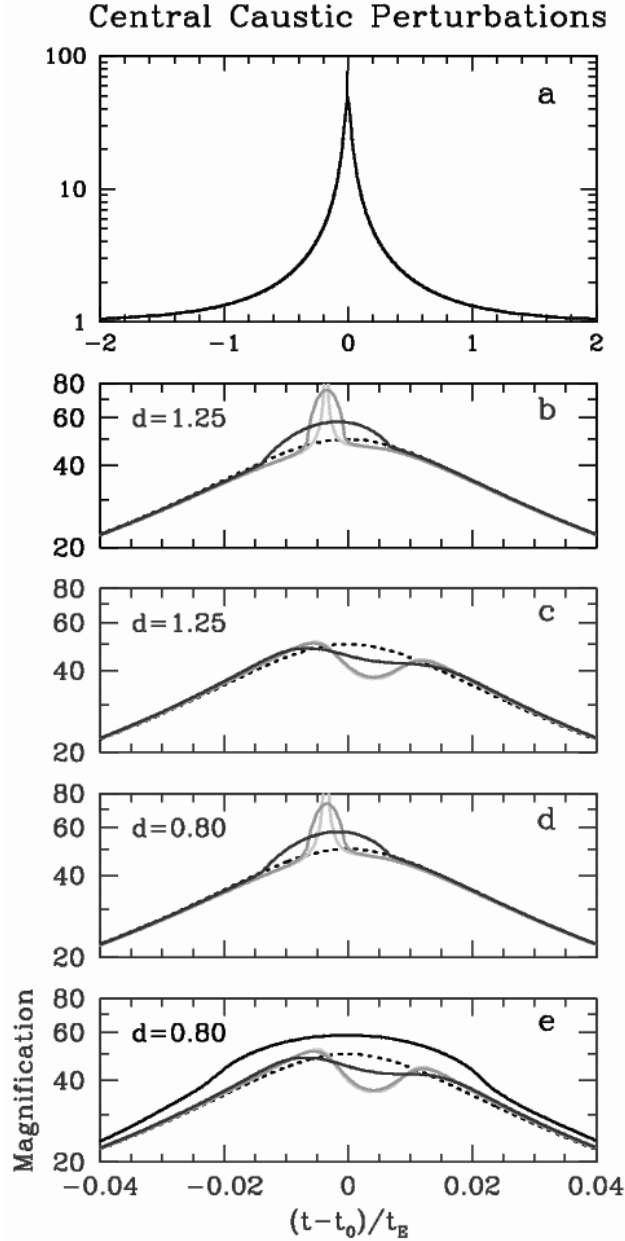


Fig. 8.— Example light curves of planetary perturbations arising from the source passing close to the central caustic in a high-magnification event, for a planet/star mass ratio of  $q = 0.001$ . Panel (a) shows the overall light curve. The impact parameter of the event with respect to the primary lens is  $u_0 = 0.02$ , corresponding to a peak magnification of  $A_{\max} \sim u_0^{-1} = 50$ . Panels (b-e) show zooms of the light curve peak. Two different cases are shown, one case of the wide planetary companion with  $d = 1.25$  (b,c), and a close planetary companion with  $d = 0.80$  (d,e). These two cases satisfy  $d \leftrightarrow d^{-1}$  and demonstrate the close/wide degeneracy. The source passes close to the central caustic; two example trajectories are shown in Figure 6 and the resulting light curves including the planetary perturbations are shown in panels b-e. The dotted line shows the magnification with no planet, whereas the solid lines show the planetary perturbations with source sizes of  $\rho_* = 0, 0.003$ , and  $0.01$ , (lightest to darkest). In panel e, the light curve for  $\rho_* = 0.03$  is also shown. In this case, the primary lens transits the source, resulting in a ‘smoothed’ peak. Although the planetary deviation is largely washed out, it is still detectable with sufficiently precise photometry.

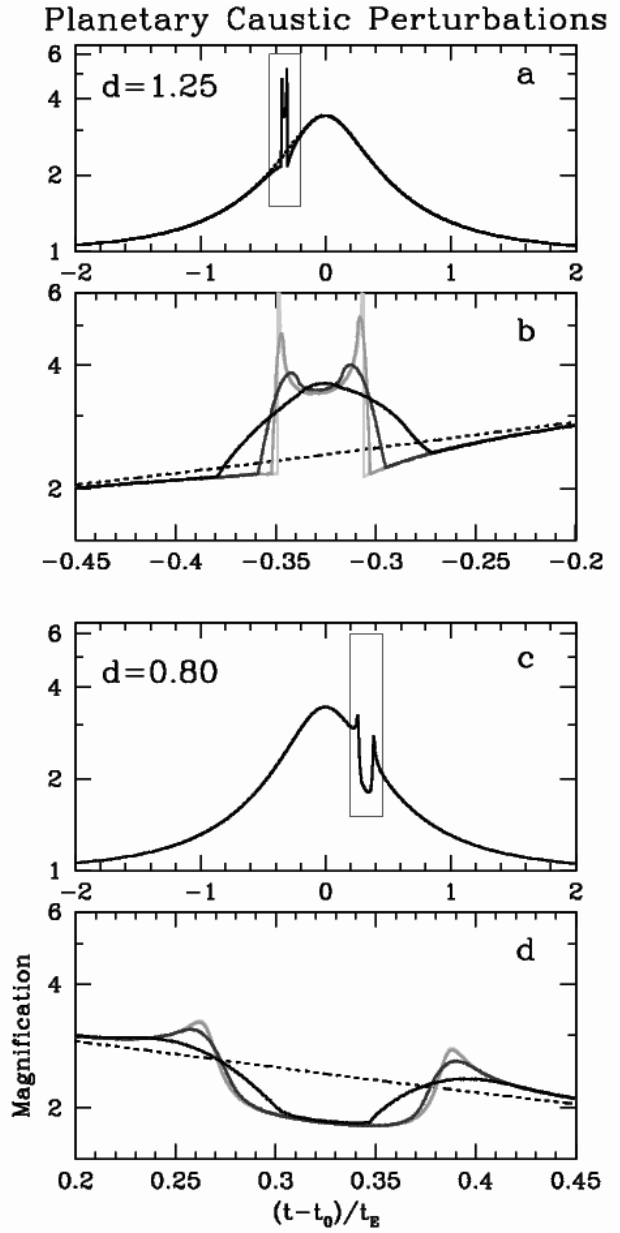


Fig. 9.— Example light curves of planetary perturbations arising from the source passing close to the planetary caustic for a planet/star mass ratio of  $q = 0.001$ . Panels (a,c) show the overall light curves, whereas panels (b,d) show zooms of the planetary deviation. Two cases are shown, one case of the wide planetary companion with  $d = 1.25$  (a,b), and a close planetary companion with  $d = 0.80$  (c,d). In both cases, the impact parameter of the event with respect to the primary lens is  $u_0 = 0.3$ . The trajectories for the light curves displayed are shown in Figure 5. The dotted line shows the magnification with no planet, whereas the solid lines show the planetary perturbations with source sizes of  $\rho_* = 0, 0.003, 0.01$ , and  $0.03$  (lightest to darkest).

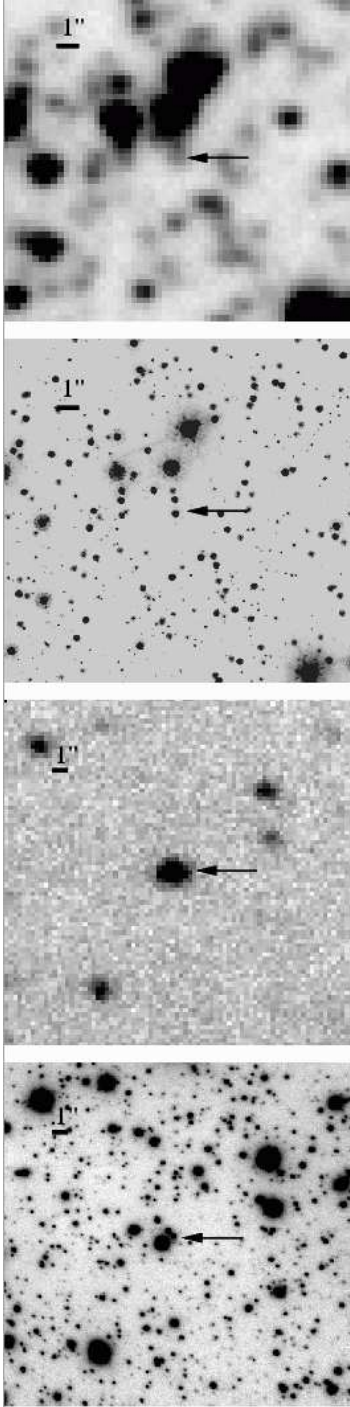


Fig. 10.— Top panel: A  $15'' \times 15''$   $I$ -band image of the field of planetary microlensing event OGLE-2005-BLG-071 obtained with the OGLE 1.3m Warsaw telescope at Las Campanas Observatory in Chile. Second panel from top: Same field as the top panel, but taken with the *Advanced Camera for Surveys* instrument on the *Hubble Space Telescope* in the F814W filter. Third panel from top:  $22'' \times 22''$   $H$ -band image of the field of planetary microlensing event MOA-2008-BLG-310 obtained with the CTIO/SMARTS2 1.3m telescope at Cerro Tololo InterAmerican Observatory in Chile. Bottom panel: Same field and filter as the panel above, but taken with the NACO instrument on VLT. In all panels, the arrow indicates the microlensing target.

are only four gross observable properties of a single-lens curve:  $t_0$ , the overall timescale of the event (i.e.,  $t_{FWHM}$ ), and the peak and baseline fluxes. Thus  $u_0$ ,  $t_E$ ,  $F_s$ , and  $F_b$  tend to be highly correlated, and are only differentiated by relatively subtle differences between light curves with the same values of the gross observables but different values of  $u_0$ ,  $t_E$ ,  $F_s$ , and  $F_b$  (Wozniak & Paczynski, 1997; Han, 1999; Dominik, 2009). As a result of these degeneracies, when fitting to data it is often useful to employ an alternate parametrization of the single-lens model that is more directly tied to these gross observables, in order to avoid strong covariances between the model parameters.

In practice, several different observatories using several different filter bandpasses typically contribute data to any given observed microlensing event. Since the flux of the source and blend will vary depending the specific bandpass, and furthermore different observatories may have different resolutions and thus different amounts of blended light, one must allow for a different source and blend flux for each filter/observatory combination. Thus the total number of parameters for a generic model fit to an observed dataset is  $N_{nl} + 2 \times N_O$ , where  $N_{nl}$  is the number of (non-linear) parameters required to specify the magnification as a function of time, and  $N_O$  is the total number of independent datasets. Since the observed flux is a linear function of  $F_s$  and  $F_b$ , for a given set of  $N_{nl}$  parameters which specify  $A(t)$ , the set of source and blend fluxes can be found trivially using a linear least-squares fit. Thus in searching for the best-fit model, one typically uses a hybrid method in which the best-fit non-linear parameters (e.g.,  $t_0$ ,  $u_0$ ,  $t_E$  for a single lens) are varied using, e.g., a downhill-simplex, Markov Chain Monte Carlo (MCMC), or grid-search method, and the specific best-fit  $F_s$  and  $F_b$  values for each trial set of non-linear parameters are determined via linear least squares.

The addition of a second lens component increases the number of model parameters by (at least) three, and the complexity enormously. As discussed in Section 2.3, the magnification pattern (magnification as a function of source position) for a binary lens is described two parameters,  $d$ , the separation of lens components in units of the Einstein ring of the lens, and  $q$ , the mass ratio of the lens. Four additional parameters specify the trajectory of the source through the magnification patterns as a function of time:  $t_0$ ,  $u_0$ ,  $t_E$ , and  $\alpha$ . The first three are analogous to the single lens case:  $u_0$  is the impact parameter of the trajectory from the origin of the lens in units of  $\theta_E$ ,  $t_0$  is the time when  $u = u_0$ , and  $t_E$  is the Einstein ring crossing time. Finally,  $\alpha$  specifies the angle of the trajectory relative to the binary-lens axis. Thus  $6 + 2 \times N_O$  parameters are required to specify the light curve arising from a generic, static binary lens. There are many possible choices for the origin of the lens, as well as the mass used for the normalization of  $\theta_E$ . The optimal choice depends on the particular properties of the lens being considered, i.e., wide stellar binary, close stellar binary, or planetary system (Dominik, 1999b). For planetary systems, one typically chooses the location of the primary for the origin and normalizes  $\theta_E$  the total mass of

the system.

Light curves arising from binary lenses exhibit an astonishingly diverse and complex phenomenology. While this diversity makes for a rich field of study, it complicates the interpretation of observed light curves mightily, for several reasons. First, other than a few important exceptions (i.e., for planetary caustic perturbations, see Section 2.1), the salient features of binary and planetary light curves have no direct relationship the canonical parameters of the underlying model. Thus it is often difficult to choose initial guesses for the fit parameters, and even if a trial solution is found, it is difficult to be sure that all possible minima have been located. Second, small changes in the values of the canonical parameters can lead to dramatic changes the resulting light curve. In particular, the sharp changes in the magnification that occur when the source passes close to or crosses a caustic can make any goodness-of-fit statistic such as  $\chi^2$  very sensitive to small changes in the underlying parameters. This, combined with the shear size of parameter space, makes brute-force searches difficult and time-consuming.

The complicated and highly corrugated shape of the  $\chi^2$  surface also causes many of the usual minimization routines (i.e. downhill simplex) to fail to find the global or even local minimum. These difficulties are compounded by the fact that the magnification of a binary lens is non-analytic and time-consuming to calculate when finite source effects are important.

Aside from their diverse phenomenology, binary lens light curves also have the important property that they can be highly degenerate, in the sense that two very different underlying lens models can produce very similar light curves. These degeneracies can be accidental, in the sense that that with relatively poor quality data or incomplete coverage of the diagnostic light curve features, otherwise distinguishable light curves can provide equally good statistical fits to a given dataset (Dominik & Hirshfeld, 1996; Dominik, 1999; Albrow *et al.*, 1999b). This is particularly problematic for caustic-crossing binary-lens light curves in which only one (i.e., the second) caustic crossing is observed. In this instance, it is typically the case that very different models can fit a given dataset<sup>13</sup>. The more insidious degeneracies, however, are those that arise from mathematical symmetries in the lens equation itself (Dominik, 1999b). For example, in the limit of a very widely separated ( $d_w \gg 1$ ) or very close ( $d_c \ll 1$ ) binary lenses, Taylor expansion reveals that the lens equations in the two cases are identical (up to an overall coordinate translation) to order  $d_c^2$  or  $d_w^{-2}$  for  $d_w \leftrightarrow d_c^{-1}(1+q)^{1/2}$  (Dominik, 1999b; Albrow *et al.*, 2002; An, 2005). Thus the magnifications are also identical to this order in these two cases. Note that for  $q_c, q_w \ll 1$ , this degeneracy is simply  $d_c \leftrightarrow d_w^{-1}$ . This degeneracy was discussed in the context of planetary lenses in Section 2.3.

It is not known if there exist analogous degeneracies for more complex (i.e., triple) lenses. These mathematical degeneracies are insidious because, if the model is deep within the limits where the degeneracies manifest themselves, it is essentially impossible, even in principle, to distinguish between the degenerate models with the photometric data alone (but see Gould & Han, 2000 for a way to resolve the close/wide degeneracy with astrometry). Both classes of degeneracies complicate the fitting of observed light curves. First, the existence of these degeneracies implies that simply finding a fit does not imply that the fit is unique. Second, these degeneracies may complicate the physical interpretation of observed light curves, because the degenerate models generally imply very different lens properties.

A number of authors have developed routines to locate fits to observed binary lens light curves. Mao & DiStefano, 1999 compiled a large library of point-source binary lens light curves, and classified these according to their salient features, such as, e.g., the number of peaks and time between peaks. They then match the features in the observed light curves to those in the library to find trial solutions for minimization routines. This approach effectively works by establishing a mapping between the light curve features and the canonical parameters. DiStefano & Perna, 1997 adopted a conceptually similar approach, where they decomposed the observed light curve into a linear combination of basis functions, then compared the resulting coefficients of this fit to those found for a library of events, again to identify promising trial solutions. Similarly, Vermaak, 2003 used artificial neural networks to identify promising regions of parameter space. While these methods can in principle be applied to any binary-lens light curve, because they are not intrinsically systematic, it is difficult to be sure that all possible fits have been identified.

Albrow *et al.*, 1999b and Cassan, 2008 developed algorithms to find a complete set of solutions for binary-lens light curves where the source crosses a caustic. These algorithms are robust in the sense that they will identify all possible fits to such light curves, and thus uncover all possible degenerate solutions (e.g., Afonso *et al.*, 2000). Unfortunately, they are also fairly user-intensive, and are obviously only applicable to a limited subset of events.

Currently, the most robust and efficient approaches to fitting observed binary-lens light curves use some variant of a hybrid approach, for example a grid search over those non-linear parameters that are not simply related to the light curve features are thus are poorly-behaved (such as the mass ratio  $q$ , projected separation  $d$ , and/or the angle of the trajectory  $\alpha$ ), combined with a downhill-simplex, steepest-descent, or MCMC fit to the remaining non-linear parameters that are more directly related to the observed light curve features. The linear parameters (such as the source and blend flux) are trivially fit for each trial solution. Often when there is some prior gross knowledge of the approximate model parameters (i.e. a wide or close planetary or binary lens) a judicious choice of parametrization guided by the inherent magnification properties of the underlying lens

<sup>13</sup>An important corollary is that, given an observed first caustic crossing, it is very difficult to predict the time of the second caustic crossing well in advance. See Albrow *et al.*, 1999b and Jaroszyński, & Mao, 2001 for further discussion.

geometry (i.e., the caustic structure of the lens) can both speed up the fit and improve the robustness of the fitting. Once trial solutions are identified, they can be more carefully explored using, e.g., Markov Chain Monte Carlo techniques. See, e.g., *Gould et al.*, 2006, *Dong et al.*, 2007, and *Bennett*, 2009. Essentially all of these approaches must be modified (although sometimes trivially) to include higher-order effects when these provide significant perturbations to the observed light curve (see Section 3.2).

In general, no robust, practical, universal, and efficient algorithm exists for fitting an arbitrary binary lens light curve in an automated way that is not highly user-intensive. For higher-multiplicity (i.e., triple) lenses, the algorithms are generally even less well-developed. As mentioned in the introduction, this is likely the current single biggest impediment to the progress of microlensing planet searches. Thus there is a urgent and growing need for the development of (more automated) analysis software.

### 3.2. Higher-Order Light Curve Effects

As reviewed in Section 3.1, the simplest model of the observed light curve arising from an isolated lens can be described by  $3 + 2 \times N_O$  parameters: the three parameters that describe the magnification as a function of time ( $u_0, t_0, t_E$ ), and a blend and source flux for each of the  $N_O$  observatory/filter combinations. This model, which accurately describes the vast majority of observed microlensing light curves, is derived under a number of assumptions, some of which may break down under certain circumstances. When a light curve deviates from this classic ‘Paczynski’ or point-source single-lens form, it is generally classified as ‘anomalous’. Not surprisingly, it is frequently the case that a robust measurement of these ‘anomalies’ allows one to infer additional properties of the primary, planet, or both (see Section 3.3).

The most obvious and most common anomaly is when the lens is not isolated. Each additional lens component requires three additional parameters<sup>14</sup> (e.g., mass ratio, projected separation, and angle between the additional component and the primary), and so the light curve arising from a lens consisting of  $N_l$  masses requires a total of  $3 \times N_l + 2 \times N_O$  parameters. Roughly  $\sim 10\%$  of all microlensing lightcurves are observed to be due to binaries. In fact, the true fraction of binary lenses is likely considerably higher, since the effects of a binary companion are only apparent when  $d$  is of order unity.

#### • Finite Source Effects

The second most common anomaly occurs when the assumption of a point source breaks down (*Gould*, 1994; *Witt & Mao*, 1994; *Witt*, 1995). As already discussed in Section 2.2.4, this assumption breaks down when the curvature of

the magnification pattern is significant over the angular size of the source, where ‘significant’ depends on the photometric precision with which the light curve is measured. Generally, the center of the source must pass within a few angular source radii  $\theta_*$  of a caustic in order for finite source effects to be important. The magnitude of finite source effects are parametrized by the angular size of the source in units of the angular Einstein ring radius,  $\rho_* \equiv \theta_*/\theta_E$ . For typical main-sequence sources in the Galactic bulge,  $\rho_*$  is of order  $10^{-3}$ , whereas for typical giant sources,  $\rho_*$  is of order  $10^{-2}$ . In addition, the amount of (filter-dependent) limb-darkening can also have an important effect on the precise shape of the portions of the light curve affected by finite-source effects.

#### • Parallax

Another common anomaly occurs when the assumptions of co-spatial and/or non-accelerating observers break down. For example, the usual expression for  $u$ , the angular separation between the lens and source in units of  $\theta_E$ , presented in Equation 28 assumes that the observer (as well as the lens and source) are moving with constant velocity. The assumption that the values of  $t_0$  and  $u_0$  are the same for all observers implies that they are all co-spatial. When either of these assumptions break down, this is generally termed (microlens) parallax. This occurs in one of three ways. First, when the duration of the microlensing event is a significant fraction of a year, the acceleration of the Earth leads to a significant non-uniform and/or non-rectilinear trajectory of the lens relative to the source, which leads to deviations in the observed light curve (*Gould*, 1992). This is referred to as ‘orbital parallax’. Second, for sources very close to a caustic, small parallax displacements due to the differences in the perspective leads to differences in the magnifications seen by observers located at different observatories for fixed time (*Holz & Wald*, 1996). This is commonly known as ‘terrestrial parallax’. Finally, if the observers are separated by a significant fraction of an AU, for example if the event is simultaneously observed from the Earth and a satellite in a solar orbit, then the differences in the magnification are large even for moderate magnification (*Refsdal*, 1966; *Gould*, 1994). This is known as ‘satellite parallax’. In all three cases, the magnitude of the effect depends on the size of relevant length scale that gives rise to the different or changing perspective (i.e., the projected separation between the observatories, the projected size of the Earth’s orbit, or the projected separation between the satellite and Earth) relative to  $\tilde{r}_E \equiv D_{\text{rel}}\theta_E$ , the angular Einstein ring radius projected on the plane of the observer (See Figure 2).

#### • Xallarap

Analogously to parallax, if the source undergoes significant acceleration over the course of the event due to a binary companion, this will give rise to deviations from the canonical light curve form (*Dominik*, 1998). This effect is commonly known as ‘xallarap’, i.e., parallax spelled backwards, to highlight the symmetry between this effect and orbital parallax. In fact, it is always possible to *exactly*

<sup>14</sup>If the additional component is very far away or very close to the primary lens, the effects of the additional component can be described by only two additional parameters: either the shear due the wide companion or the quadrupole moment of the lens for the close companion, and the angle of the trajectory with respect to the projected binary axis.

mimic the effects of orbital parallax with a binary source with the appropriate orbital parameters (*Smith et al.* 2003). For sufficiently precise data, such that the parallax/xallarap parameters are well constrained, these two scenarios can be distinguished because it would be *a priori* unlikely for a binary source to have exactly the correct parameters to mimic the effects of orbital parallax (*Poindexter et al.*, 2005). The magnitude of xallarap effect depends on the semimajor axis of the binary relative to  $\hat{r}_E \equiv D_s \theta_E$ , the Einstein ring radius projected on the source plane.

#### • Orbital Motion

For binary or higher multiplicity lenses, relative orbital motion of the components can also give rise to deviations from the light curve expected under the usual static lens assumption (*Dominik*, 1998). For the general case of a binary lens and a Keplerian orbit, an additional five parameters beyond the usual static-lens parameters are needed to specify the light curve (*Dominik*, 1998). Typically, however, only two additional parameters can be measured: the two components of the relative projected velocity of the lenses. These two components can be parametrized by the rate of the change of the binary projected binary axis  $\dot{d}$  and the angular rotation rate of the binary  $\omega$ . The effect of the latter is simply to rotate that magnification pattern of the lens on the sky, whereas the former results in a change in the lens mapping itself, and thus a change in the caustic structure and magnification pattern.

#### • Binary Sources

If the source is a binary and the lens happens to pass sufficiently close to both sources, the light curve can exhibit a deviation from the generic single-lens, single source form (*Griest & Hu*, 1992). For static binaries, the morphology of the deviation depends on the flux ratio of the sources, their projected angular separation in units of  $\theta_E$ , and the impact parameter of the lens from the source companion. By convention, such ‘binary source’ effects are conceptually distinguished from xallarap effects by the nature of the deviation: if the deviation is caused by the source companion being significantly magnified by the lens, is called a binary source effect, if it caused by the acceleration due to the companion, it is called xallarap. Of course, depending on the parameters of the source and lens, light curves can exhibit only binary source effects, only xallarap, or both xallarap and binary-source effects.

#### • Other Miscellaneous Effects

A number of additional high-order effects have been discussed in the literature, for example the effects of the finite physical size of the lens (*Bromley*, 1996; *Agol*, 2002). In most cases, these higher-order effects are expected to unobservable and/or extremely rare.

### 3.3. Properties of the Detected Systems

For microlensing events due to single, isolated lenses, the parameters that can routinely be measured are the time of maximum magnification  $t_0$ , the impact parameter of the event in units of the Einstein ring radius  $u_0$ , and the Einstein

timescale  $t_E$ , along with a source flux  $F_s$  and blend flux  $F_b$  for each observatory/filter combination. Of these parameters,  $u_0$  and  $t_0$  are simply geometrical parameters and contain no physical information about the lens. The Einstein timescale  $t_E$  is a degenerate combination of the lens mass  $M$ , the relative lens-source parallax  $\pi_{\text{rel}}$ , and the relative lens-source proper motion  $\mu_{\text{rel}}$ . Therefore it is not possible to uniquely determine the mass and distance to the lens from a measurement of  $t_E$  alone. The blend flux  $F_b$  contains light from any source that is blended with the source, including light from the lens if it is luminous. Unfortunately, for the typical targets toward the Galactic bulge, ground-based images typically contain light from other, unrelated sources, and it is not possible to isolate the light from the lens (see Figure 10). Therefore, in the vast majority of microlensing events, the mass, distance, and proper motion of the lens are unknown.

As discussed below, for binary and planetary microlensing events it is routinely possible to infer the mass ratio  $q$ , and  $d$ , the instantaneous projected separation between the planet and star in units of  $\theta_E$ . However, the mass of the planet is typically not known without a constraint on the primary mass. Furthermore, a measurement of  $d$  alone provides very little information about the orbit, since  $\theta_E$  and the inclination, phase, and ellipticity of the orbit are all unknown *a priori*. For these reasons, when microlensing planet searches were first initiated it was typically believed that detailed information about individual systems would be very limited for planets detected in microlensing light curves. This apparent deficiency was exacerbated by the perception that the host stars would typically be too distant and faint for follow-up observations.

Fortunately, in reality much more information can typically be gleaned from a combination of a detailed analysis of the light curve and follow-up, high-resolution imaging, using the methods outlined below.

#### • Mass Ratio and Projected Separation

First, the requirements for accurately measuring the minimum three additional parameters needed to describe the light curves of binary and planetary microlensing events are discussed. These three additional parameters are the aforementioned  $q$ ,  $d$ , and  $\alpha$ .

For planetary caustic perturbations, these parameters can essentially be ‘read off’ of the observed light curve. In this case, the gross properties of the planetary perturbation can be characterized by three observable quantities: the time of the planetary perturbation  $t_{0,p}$ , the timescale of the planetary perturbation  $t_{E,p}$ , and the magnitude of the perturbation  $\delta_p$ . These quantities then simply and completely specify the underlying parameters  $q$ ,  $d$ ,  $\alpha$ , up to a two-fold discrete degeneracy in  $d$ , corresponding to whether the planet is perturbing the major or minor image, i.e.,  $d \leftrightarrow d^{-1}$ . Since these two situations result in very different types of perturbations (see Figure 9), this discrete degeneracy is easily resolved (*Gaudi & Gould*, 1997b). If finite source effects are important but not dominant, then there also exists a continuous degeneracy between  $q$  and  $\rho_*$ , stemming from the fact that

in this regime, both determine the width of the perturbation  $t_p$  (Gaudi & Gould, 1997b). However, this degeneracy is easily broken by good coverage and reasonably accurate photometry in the wings of the perturbation. Finally, there is also a degeneracy between major image ( $d > 1$ ) planetary caustic perturbations and a certain class of binary-source events, namely those with extreme flux ratio between the two sources. Specifically, it is always possible to find a binary-source light curve that can exactly reproduce the observables  $t_{0,p}$ ,  $t_{E,p}$ , and  $\delta_p$  (Gaudi, 1998). This degeneracy is also easily broken by good coverage and accurate photometry (Gaudi, 1998; Gaudi & Han, 2004; Beaulieu *et al.*, 2006).

For central or resonant caustic perturbations in high-magnification events, extracting the parameters  $q, d, \alpha$  is typically more complicated due to the fact that there is no simple, general relationship between the salient features of the light curve perturbation and these parameters. Thus fitting these perturbations typically requires a more sophisticated approach, as discussed in Section 3.1. In addition, there are a number of degeneracies that plague central caustic perturbations. First, as discussed in 2.3 and illustrated in Figures 6 and 8, there is a close/wide duality such that the central caustic shape and associated magnification pattern are highly degenerate under the transformation  $d \leftrightarrow d^{-1}$  (Griest & Safizadeh 1999; Dominik, 1999b). This degeneracy becomes more severe for very close/very wide planets, and in some cases it is essentially impossible to distinguish between the two solutions, even with extremely accurate photometry and dense coverage of the perturbation (e.g., Dong *et al.*, 2009a). There also exists a degeneracy between central caustic planetary perturbations, and perturbations due to very close or very wide binary lenses. Very close binaries have small, asteroid-shaped caustic located at the center-of-mass of the system, whereas very wide binaries have small, asteroid-shaped caustics near the positions of each of the lenses. The gross features of central caustic perturbations can be reproduced by a source passing by the asteroid-shape caustic produced by a close/wide binary lens (Dominik, 1999; Albrow *et al.*, 2000; An, 2005). Since close/wide binary lenses are themselves degenerate under the transformation  $d_w \leftrightarrow d_c^{-1}(1+q)^{1/2}$ , there is a four-fold degeneracy for perturbations near the peak of high-magnification events. Fortunately, the degeneracy between planetary central caustic perturbations and close/wide binary lens perturbations can be resolved with good coverage of the perturbation and accurate photometry (Albrow *et al.*, 2000; Han & Gaudi, 2008; Han, 2009).

#### •Einstein Ring Radius

The requirement for detecting a planet via microlensing is generally that the source must pass reasonably close to the caustics produced by the planetary companion. However, this is also basically the condition for finite source size effects to be important. Thus for most planetary microlensing events, it is possible to infer the angular size of the source in units of the angular Einstein ring radius,  $\rho_* \equiv \theta_*/\theta_E$ .

The angular size of the source can be estimated by its de-reddened color and magnitude using empirical color-surface brightness relations determined from angular size measurements of nearby stars (van Belle, 1999; Kervella *et al.*, 1994). The source flux  $F_s$  is most easily determined by a fit to the microlensing light curve of the form  $F(t) = F_s A(t) + F_b$ , as the variable magnification of the source allows one to ‘deblend’ the source and blend flux. Determining the color of the source in this manner requires measurements in two passbands, and thus while observations are typically focused on a single passband (typically a far-red visible passband such as  $R$  or  $I$ ), it is important to acquire a few points in a second filter to determine the source color. The extinction toward the source can be approximately determined by comparison to nearby red giant clump stars (Yoo *et al.*, 2004), which have a known and essentially constant luminosity and intrinsic color (e.g., Paczynski & Stanek, 1998). An error in the extinction affects both the inferred color and magnitude of the source, fortunately these have opposite and nearly equal effects on the inferred value of  $\theta_*$  (Albrow *et al.*, 1999a).

Thus for events in which finite source effects are robustly detected, it is possible to measure  $\theta_E$  (Gould, 1994). This partially breaks the timescale degeneracy, since

$$\frac{M}{D_{\text{rel}}} = \frac{c^2}{4G} \theta_E^2. \quad (31)$$

The distance to the source is typically known approximately from its color and magnitude (and furthermore the overwhelming majority of sources are in the bulge), and so a measurement of  $\theta_E$  essentially provides a mass-distance relation for the lens.

#### •Light from the Lens

Although the majority of the lenses that give rise to microlensing events are distant and low-mass main-sequence stars, most are nevertheless usually sufficiently bright that their flux can be measured to relative precision of  $\lesssim 10\%$  with moderate-aperture (1-2m) telescopes and reasonable ( $10^2 - 10^4$  s) exposure times, provided that the light from the lens can be isolated. The fit to the microlensing light curve gives the flux of the source  $F_s$ , and the blend flux  $F_b$ . The latter contains the flux from any stars that are not being lensed but are unresolved on the image, i.e., blended with the source star. Generally, this blend flux can be decomposed into several contributions,

$$F_b = F_l + F_{l,c} + F_{s,c} + \sum_j F_{u,j}, \quad (32)$$

where  $F_l$  is the flux from the lens,  $F_{l,c}$  is the flux from any (blended) companions to the lens,  $F_{s,c}$  is the flux from any (blended) companions to the source, and  $F_{u,j}$  is the flux from each unrelated nearby star  $j$  that is blended with the source. As illustrated in Figure 10, at typical ground-based resolutions of  $1''$  and in the extremely crowded target fields toward the bulge where microlensing surveys are carried out, it is often the case that there are several unrelated

stars blended with the source star. Therefore, the lens light cannot be uniquely identified based on such data alone. At the higher resolutions of  $0.05 - 0.1''$  available from *HST* or ground-based AO imaging, essentially all stars unrelated to the source our lens are resolved. Since the source and lens must be aligned to  $\lesssim \theta_E \sim 1$  mas for a microlensing event to occur and the typical relative lens-source proper motions are  $\mu_{\text{rel}} \sim 5 - 10$  mas yr $^{-1}$  for microlensing events towards the bulge, the lens and source will be blended in images taken within  $\sim 10$  years of the event, even at the resolution of *HST*. However, because the microlensing fit gives  $F_s$ , the lens flux can be determined by subtracting this flux from the combined unresolved lens+source flux in the high-resolution image, assuming no blended companions to the lens or source (Bennett *et al.*, 2007).

There are several potential complications to this procedure to determine the lens flux. First,  $F_s$  determined from the microlensing fit will generally not be absolutely calibrated. Thus the high-resolution photometric data must be ‘photometrically aligned’ to the microlens dataset. Typically this is done by matching stars common to both sets of images. The accuracy of this alignment is usually limited to  $\sim 1\%$  due to the small number of common, isolated stars available (Dong *et al.*, 2009b). It may also be the high-resolution images are taken in a different filter than that for which the source flux  $F_s$  is determined, necessitating a (model-dependent) color transformation and introducing additional uncertainties (e.g., Bennett *et al.*, 2008). Note that it is possible to avoid this procedure entirely if the high-resolution images can be taken at two different epochs with substantially different source star magnifications. However, since this means at least one epoch must be taken when the source is significantly magnified during the event, this requires target-of-opportunity observations. Finally, any light in excess of the source detected in the high-resolution images may be attributed to close physical companions to the lens or source. In some favorable cases (i.e., high magnification events), it is possible to exclude these scenarios by the (lack of) second order effects the companion would produce in the observed light curve. For example, a binary companion to the lens produces a caustic which would be detectable in sufficiently high-magnification events, whereas a sufficiently close companion to the source would give rise to xallarap effects which would be detectable in long timescale events (Dong *et al.*, 2009b).

A measurement of the flux of the lens in a single passband, along with a model for extinction as a function of distance and a mass-luminosity relationship, gives a mass-distance relationship for the lens (Bennett *et al.*, 2007). A second measurement of the flux in a different passband can provide a unique mass and distance to the lens, subject to the uncertainties in the intrinsic color as a function of mass and the dust extinction properties as a function of wavelength and distance.

#### •Proper Motion

For typical values of  $\mu_{\text{rel}} \sim 5 - 10$  mas/yr for mi-

cro-lensing events toward the Galactic bulge, after a few years, the lens and source will be displaced by  $\sim 0.01$  arc-seconds. For luminous lenses, and using space telescope or AO imaging, it is possible measure the relative lens-source proper motion, either by measuring the elongation of the PSF or by measuring the difference in the centroid in several filters if the lens and source have significantly different colors (Bennett *et al.*, 2007). The proper motion can be combined with the timescale to give the angular Einstein ring radius,  $\theta_E = \mu_{\text{rel}} t_E$ .

#### •Microlens Parallax

For some classes of events, it is possible to obtain additional information about the lens by measuring the microlensing parallax,  $\pi_E$ , a vector with magnitude  $|\pi_E| = \text{AU}/\tilde{r}_E$ , and direction of the relative lens-source proper motion. Recall  $\tilde{r}_E \equiv D_{\text{rel}}\theta_E$  is the Einstein ring radius projected onto the observer plane. As discussed in Section 3.2 microlens parallax effects arise in one of three varieties: orbital parallax due to the acceleration of the Earth during the event, terrestrial parallax in high-magnification events observed by non-cospatial observers, and satellite parallax for events observed from the ground and a satellite in solar orbit.

Orbital parallax deviations are generally only significant for events with timescales that are a significant fraction of a year, and so long as compared to the median timescale of  $\sim 20$  days. Furthermore, the deviations due to orbital parallax are subject to an array of degeneracies (Gould *et al.*, 1994; Smith *et al.*, 2003; Gould, 2004), which can hamper the ability to extract unique microlens parallax parameters. The severity of these degeneracies depend on the particular parameters of the event in question, but for most events it is the case that the only robustly-measured effect in the light curve is an overall asymmetry, which only yields one projection of  $\pi_E$ , namely that in the direction perpendicular to the instantaneous Earth-Sun acceleration vector at the time of the event (Gould *et al.* 1994). If the direction of the relative lens-source proper motion vector  $\mu_{\text{rel}}$  can be independently determined from the proper motion of a luminous lens, then it is possible to determine the full  $\pi_E$  vector, since  $\pi_E$  is parallel to  $\mu_{\text{rel}}$ .

Orbital parallax measurements made from two observatories are also subject to several degeneracies, which have been studied by several authors (Refsdal, 1966; Gould, 1994, 1995; Bouteux & Gould, 1996; Gaudi & Gould, 1997a). These can be resolved in a number of ways (Gould, 1995; Gould, 1999; Dong *et al.*, 2007), including observing from a third observatory, which allows one to uniquely ‘triangulate’ the parallax effects (Gould, 1994). Similarly, terrestrial parallax measurements from only two observatories are subject to degeneracies which can be resolved with simultaneous observations from a third observatory that is not co-linear with the other two.

A measurement of the microlens parallax allows one to partially break the timescale degeneracy and provides a

mass-distance relation for the lens,

$$MD_{\text{rel}} = \frac{c^2}{4G} \tilde{r}_E^2. \quad (33)$$

#### •Orbital Motion of the Planet

In at least two cases, the orbital motion of the planet during the microlensing event has been detected (*Dong et al.*, 2009a; *Bennett et al.*, 2009). The effects of orbital motion generally allow the measurement of the two components of the projected velocity of the planet relative to the primary star. If an external measurement of the mass of the lens is available, and under the assumption of a circular orbit, these two components of the projected velocity completely specify the full orbit of the planet (including inclination), up to a two-fold degeneracy (*Dong et al.*, 2009a). In some cases, higher-order effects of orbital motion can be used to break this degeneracy and even constrain the ellipticity of the orbit (*Bennett et al.*, 2009).

#### •Bayesian Analysis

In the cases when only  $t_E$ ,  $q$ , and  $d$  can be measured, constraints on the mass and distance to the lens (and so mass and semimajor axis of the planet), must rely on a Bayesian analysis which incorporates priors on the distribution of microlens masses, distances and velocities (e.g., *Dominik*, 2006; *Dong et al.*, 2006).

#### •Complete Solutions

In many cases, several of these pieces of information can be measured in the same event, often providing complete or even redundant measurements of the mass, distance, and transverse velocity of the event. For example, a measurement of  $\theta_E$  from finite source effects, when combined with a measurement of  $r_E$  from microlens parallax, yields the lens mass,

$$M = \left( \frac{c^2}{4G} \right) \tilde{r}_E \theta_E, \quad (34)$$

distance

$$D_l^{-1} = \frac{\theta_E}{\tilde{r}_E} + D_s^{-1}, \quad (35)$$

and transverse velocity (*Gould*, 1996).

### 3.4. Practical Aspects of Current Microlensing Searches

The microlensing event rate toward the Galactic bulge is  $\mathcal{O}(10^{-6})$  events per star per year (*Paczynski*, 1991). In a typical field toward the Galactic bulge, the surface density of stars is  $\sim 10^7$  stars per  $\text{deg}^2$  to  $I \sim 20$  (*Holtzman et al.*, 1998). Thus to detect  $\sim 100$  events per year,  $\sim 10 \text{ deg}^2$  of the Bulge must be monitored. Until relatively recently, large-format CCD cameras typically had fields of view of  $\sim 0.25 \text{ deg}^2$ , and thus  $\sim 40$  pointings were required and so fields could only be monitored once or twice per night. While this cadence is sufficient to detect the primary microlensing events, it is insufficient to detect and characterize planetary perturbations, which last a few days or less.

As a result, microlensing planet searches have operated using a two-stage process. The Optical Gravitational Lens Experiment (OGLE, *Udalski*, 2003) and the Microlensing

Observations in Astrophysics (MOA, *Sako et al.*, 2008) collaborations monitor several tens of square degrees of the Galactic bulge, reducing their data real-time in order to alert microlensing event in progress. A subset of these alerted events are then monitored by several follow-up collaborations, including the Probing Lensing Anomalies NETwork (PLANET, *Albrow et al.*, 2008), RoboNet (*Tsapras et al.*, 2009), Microlensing Network for the Detection of Small Terrestrial Exoplanets (MiNDSTeP, *Dominik et al.*, 2008), and Microlensing Follow Up Network ( $\mu$ FUN, *Yoo et al.*, 2004) collaborations. Since only individual microlensing events are monitored, these teams can achieve the sampling and photometric accuracy necessary to detect planetary perturbations. In fact, the line between the ‘alert’ and ‘follow-up’ collaborations is now somewhat blurry, both because the MOA and OGLE collaborations monitor some fields with sufficient cadence to detect planetary perturbations, and because there is a high level of communication between the collaborations, such that the observing strategies are often altered real time based on available information about ongoing events.

There are two conceptually different channels by which planets can be detected with microlensing, corresponding to whether the planet is detected through perturbations due to the central caustic (as shown in Figure 8), or perturbation due to the planetary caustic(s) (as shown in Figure 9). Because, for any given planetary system, the planetary caustics are always larger than the central caustics, the majority of planetary perturbations are caused by planetary caustics. Thus searching for planets via the influence of the planetary caustics is termed the ‘main channel’. However, detecting planets via the main channel requires substantial commitment of resources because the unpredictable nature of the perturbation requires dense, continuous sampling, and furthermore the detection probability per event is relatively low so many events must be monitored. Detecting planets via their central caustic perturbations requires monitoring high magnification primary events near the peak of the event. In this case, the trade-off is that although high-magnification events are rare (a fraction  $\sim 1/A_{\text{max}}$  of events have maximum magnification  $\gtrsim A_{\text{max}}$ ), they are individually very sensitive to planets. The primary challenge lies with this channel lies with identifying high-magnification events real time.

Which approach is taken depends on the resources that the individual collaborations have available. The PLANET collaboration has substantial access to 0.6-1.5m telescopes located in South Africa, Perth, and Tasmania. With these resources, they are able to monitor dozens of events per season, and so are able to search for planets via the main channel. This tactic led to the detection of the first cool rocky/icy exoplanet OGLE-2005-BLG-390Lb (*Beaulieu et al.*, 2006). On the other hand, the  $\mu$ FUN collaboration use a single 1m telescope in Chile to monitor promising alerted events in order try to identify high-magnification events substantially before peak. When likely high-magnification events are identified, the other telescopes in the collaboration are then

engaged to obtain continuous coverage of the light curve during the high-magnification peak. High-magnification events often reach peak magnitudes of  $I \lesssim 15$ , and thus can be monitored with relatively small-apertures (0.3-0.4m). This allows amateur astronomers to contribute to the photometric follow-up. Indeed over half of the members of the  $\mu$ FUN collaboration are amateurs.

#### 4. FEATURES OF THE MICROLENSING METHOD

The unique way in which microlensing finds planets leads to some useful features, as well as some (mostly surmountable) drawbacks. Most of the features of the microlensing method can be understood simply as a result of the fact that planet detection relies on the direct perturbation of images by the gravitational field of the planet, rather than on light from the planet, or the indirect effect of the planet on the parent star.

##### • Peak Sensitivity Beyond the Snow Line

The peak sensitivity of microlensing is for planet-star separations of  $\sim r_E$ , which corresponds to equilibrium temperatures of

$$T_{\text{eq}} = 278 \text{ K} \left( \frac{L}{L_\odot} \right)^{1/4} \left( \frac{r_E}{\text{AU}} \right)^{-1/2} \sim 70 \text{ K} \left( \frac{M}{0.5 M_\odot} \right), \quad (36)$$

where the rightmost expression assumes  $L/L_\odot = (M/M_\odot)^5$ ,  $D_l = 4 \text{ kpc}$ , and  $D_s = 8 \text{ kpc}$ . Thus microlensing is most sensitive to planets in the regions beyond the ‘snow line,’ the point in the protoplanetary disk exterior to which the temperature is less than the condensation temperature of water in a vacuum (*Lecar et al.*, 2006; *Kennedy et al.*, 2007; *Kennedy & Kenyon*, 2008). Giant planets are thought to form in the region immediately beyond the snow line, where the surface density of solids is highest (*Lissauer*, 1987).

Is microlensing sensitive to habitable planets? For assumptions above, and further assuming the habitable zone is centered on  $a_{\text{HZ}} = \text{AU}(L/L_\odot)^{1/2}$ , the projected separation of a planet in the habitable zone in units of  $\theta_E$  is  $d_{\text{HZ}} \sim 0.25(M/M_\odot)^2$ . Thus for typical hosts of  $M \lesssim M_\odot$ , the habitable zone is well inside the Einstein ring radius (*Di Stefano*, 1999). Since microlensing is much less sensitive to planets with separations much smaller than the Einstein ring radius as these can only perturb highly demagnified images, it is much less sensitive to planets in the habitable zones of their parent stars (*Park et al.*, 2006) for typical events. However, it is important to note that this is primarily a statistical statement about the typical sizes of the angular Einstein ring radii of microlensing events, rather than a statement about any intrinsic limitations of the microlensing method. A fraction of events have substantially smaller Einstein ring radii, and for these events there is significant sensitivity to habitable planets. In particular, lenses closer to the observer have smaller Einstein ring radii and so microlensing events from nearby stars will have more sensitivity to habitable planets (*DiStefano & Night*, 2008; *Gaudi et al.* 2008b). Indeed, a space-based microlensing

planet search mission (described in Section 6) will have significant sensitivity to habitable planets, primarily due to the large number of events being searched for planets (*Bennett et al.*, 2008).

##### • Sensitivity to Low-mass Planets

The amplitudes of the perturbations caused by planets are typically large,  $\gtrsim 10\%$ . Furthermore, although the durations of the perturbations get shorter with planet mass (as  $\sqrt{m_p}$ ) and the probability of detection decreases (also roughly as  $\sqrt{m_p}$ ), the amplitude of the perturbations are independent of the planet mass. This holds until the ‘zone of influence’ of the planet, which has a size  $\sim \theta_{E,p}$ , is smaller than the angular size of the source  $\theta_*$ . When this happens, the perturbation is ‘smoothed’ over the source size, as demonstrated in Figures 8 and 9. For typical parameters,  $\theta_{E,p} \sim \mu \text{as}(m_p/M_\oplus)^{1/2}$ , and for a star in the bulge,  $\theta_* \sim \mu \text{as}(R_*/R_\odot)$ . This ‘finite source’ suppression essentially precludes the detection of planets with mass  $\lesssim 5 M_\oplus$  for clump giant sources in the bulge with  $R_* \sim 10 R_\odot$  (*Bennett & Rhie*, 1996). For main-sequence sources ( $R \sim R_\odot$ ), finite source effects become important for planets with the mass of the Earth, but does not completely suppress the perturbations and render them undetectable until masses of  $\sim 0.02 M_\oplus \sim 2 M_{\text{Moon}}$  for main-sequence sources (*Bennett & Rhie*, 1996; *Han et al.*, 2005). Thus microlensing is sensitive to Mars mass planets and even planets a few times the mass of the Moon, for sufficiently small source sizes.

##### • Sensitivity to Long-Period and Free-Floating Planets

Since microlensing can ‘instantaneously’ detect planets without waiting for a full orbital period, it is immediately sensitive to planets with very long periods. Although the probability of detecting a planet decreases for planets with separations larger than the Einstein ring radius because the magnifications of the images decline, it does not drop to zero. For events in which the primary star is also detected, the detection probability for very wide planets with  $d \gg 1$  is  $\sim (\theta_{E,p}/\theta_E)d^{-1} = q^{1/2}d^{-1}$  (*Di Stefano & Scalzo*, 1999b). Indeed since microlensing is directly sensitive to the planet mass, planets can be detected even without a primary microlensing event (*Di Stefano & Scalzo*, 1999a). Even free-floating planets that are not bound to any host star are detectable in this way (*Han et al.*, 2005). Microlensing is the only method that can detect old, free-floating planets. A significant population of free-floating planets is a generic prediction of most planet formation models, particular those that invoke strong dynamical interactions to explain the observed eccentricity distribution of planets (*Goldreich et al.*, 2004; *Juric & Tremaine*, 2008; *Ford & Rasio*, 2004).

##### • Sensitivity to Planets Orbiting a Wide Range of Host Stars

The hosts probed by microlensing are simply representative of the population of massive objects along the line of sight to the bulge sources, weighted by the lensing probability. Figure 11 shows a model by *Gould*, 2000 for the microlensing event rate toward the Galactic bulge as a function of the host star mass for all lenses, and also broken down

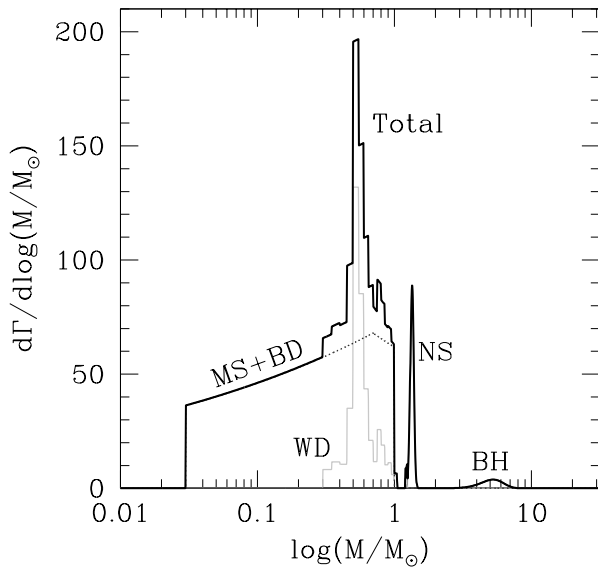


Fig. 11.— The rate of microlensing events toward the Galactic bulge as a function of the mass of the lens, for main sequence (MS) stars and brown dwarfs (BD,  $0.03M_{\odot} < M < 1M_{\odot}$ ) (bold dashed curve) and white dwarfs (WD), neutron stars (NS), and black hole (BH) remnants (solid curves). The total is shown by a bold solid curve. From *Gould, 2000*.

by the type of host, i.e., star, brown dwarf, or remnant. The sensitivity of microlensing is weakly dependent on the host star mass, and has essentially no dependence on the host star luminosity. Thus microlensing is about equally sensitive to planets orbiting stars all along the main sequence, from brown dwarfs to the main-sequence turn-off, as well as planets orbiting white dwarfs, neutron stars, and black holes.

#### • Sensitivity to Planets Throughout the Galaxy

Because microlensing does not rely on light from the planet or host star, planets can be detecting orbiting stars with distances of several kiloparsecs. The microlensing event rate depends on the intrinsic lensing probability, which peaks for lens distances about halfway to the typical sources in the Galactic bulge, and the number density distribution of lenses along the line-of-sight toward the bulge, which peaks at the bulge. The event rate remains substantial for lens distances in the range  $D_l \sim 1 - 8$  kpc. Roughly 40% and 60% of microlensing events toward the bulge are expected to be due to lenses in the disk and bulge, respectively (*Kiraga & Paczynski, 1994*). Specialized surveys may be sensitive to planets with  $D_l \lesssim 1$  kpc (*Di Stefano, 2008; Gaudi et al., 2008*), as well as planets in M31 (*Covone et al., 2000; Chung et al., 2006; Ingrassio et al., 2009*).

#### • Sensitivity to Multiple-Planet Systems

For low-magnification events, multiple planets in the same system can be detected only if the source crosses the planetary caustics of both planets, or equivalently only if both planets happen to have projected positions sufficiently

close to the paths of the two images created by the primary lens. The probability of this is simply the product of the individual probabilities, which is typically  $\mathcal{O}(1\%)$  or less (*Han & Park, 2002*). In high-magnification events, however, individual planets are detected with near-unity probability regardless of the orientation of the planet with respect to the source trajectory (*Griest & Safizadeh, 1998*). This immediately implies all planets sufficiently close to the Einstein ring radius will be revealed in such events (*Gaudi et al., 1998*). This, along with the fact that high-magnification events are potentially sensitive to very low-mass planets, makes such events excellent probes of planetary systems.

#### • Sensitivity to Moons of Exoplanets

Because microlensing is potentially sensitive to planets with mass as low as that of a few times the mass of the Moon (*Bennett & Rhie, 1996*), it is potentially sensitive to large moons of exoplanets. A system with a star of mass  $M$ , planet of mass  $m_p$ , and moon of mass  $m_m$  corresponds to a triple lens with the hierarchy  $m_m \ll m_p \ll M$ . *Bennett & Rhie, 2002; Han & Han, 2002; Han, 2008; and Liebig & Wambsganss, 2009* have all considered the detectability of moons of various masses, orbiting planets of various masses. Generally, these studies find that massive terrestrial ( $m_m \sim M_{\oplus}$ ) moons (should they exist) are readily detectable. Less massive moons, with masses similar to our Moon, are considerably more difficult to detect, but may be detectable in next-generation microlensing planet searches, particularly those from space, in some favorable circumstances (i.e., for sources with small dimensionless source size  $\rho_*$ ). Analogous to planetary microlensing, moons with projected separation much smaller than the Einstein radius of the planet  $r_{E,p} \equiv \theta_{E,p} D_l$  are difficult to detect (*Han, 2008*). Contrary to planetary microlensing, however, the signal of the moon does not diminish for angular separations much greater than  $r_{E,p}$  (*Han, 2008*), although of course it becomes less likely that both the planetary and moon signal will be detected simultaneously.

A minimum requirement for a moon to be stable is that its semimajor axis must be less the Hill radius of the planet, which is given by

$$r_H = a_p \left( \frac{m_p}{3M} \right)^{1/3}, \quad (37)$$

where  $a_p$  is the semimajor axis of the planet. The ratio of  $r_H$  to the Einstein ring radius of the planet is,

$$\frac{r_H}{r_{E,p}} \sim dq^{-1/6}. \quad (38)$$

Thus for  $q \lesssim 10^{-3}$ , detectable moons also (fortuitously) happen to be stable.

## 5. RECENT HIGHLIGHTS

To date, ten detections of planets with microlensing have been announced, in nine systems (*Bond et al., 2004; Udalski et al., 2005; Beaulieu et al., 2006; Gould et al., 2006; Gaudi et al., 2008a; Bennett et al., 2008; Dong et al., 2009;*

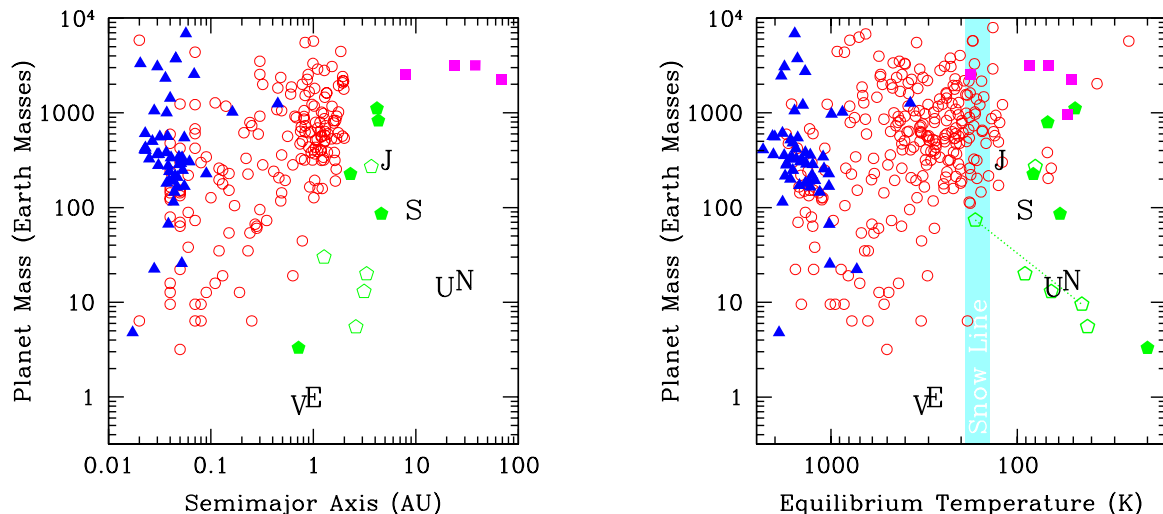


Fig. 12.— (Left) Mass versus semi-major axis for known exoplanets. (Right) Mass versus equilibrium temperature for known exoplanets. In both panels, radial velocity detections are indicated by red circles, transiting planets are indicated by blue triangles, microlensing detections are indicated by green pentagons, and direct detections are indicated by magenta squares. The letters indicate the locations of the Solar System planets. The solid pentagons are those microlensing detections for which the primary mass and distance are measured, and thus planet mass, semimajor axis, and equilibrium temperature are well-constrained. The open pentagons indicate those microlensing detections for which only partial information about the primary properties is available, and thus the planet properties are relatively uncertain. An extreme example is shown in right panel, where two points connected by a dotted line are plotted for event MOA-2008-BLG-310Lb (*Janczak et al.* 2009), corresponding to the extrema of the allowed range of planet properties. In the right panel, the light blue stripe roughly indicates the location of the snow line. These figures also demonstrate the complementarity of the various planet detection techniques: transit and radial velocity surveys are generally sensitive to planets interior to the snow line, whereas microlensing and direct imaging surveys are sensitive to more distant planets beyond the snow line.

*Janczak et al.*, 2009; *Sumi et al.*, 2009). In addition, there are another seven events with clear, robust planetary signatures that await complete analysis and/or publication. The masses, separations, and equilibrium temperatures of the ten announced planets are shown in Figure 12. We can expect to a handful of detections per year at the current rate.

The right panel of this Figure 12 demonstrates that the first microlensing planet detections are probing a region of parameter space that has not been previously explored by any method, namely planets beyond snow line. As a result, although the total number of planets found by microlensing to date is small in comparison to the sample of planets revealed by the radial velocity and transit methods, these discoveries have already provided important empirical constraints on planet formation theories. In particular, the detection of four cold, low mass ( $5 - 20 M_{\oplus}$ ) planets amongst the sample of microlensing detections indicates that these planets are common (*Beaulieu et al.*, 2006; *Gould et al.*, 2006, *Sumi et al.*, 2009). The detection of a Jupiter/Saturn analog also suggests that solar system analogs are probably not rare (*Gaudi et al.*, 2008). Finally, the detection of a low-mass planetary companion to a brown-dwarf star suggests that such objects can form planetary systems similar to those around solar-type main-sequence stars (*Bennett et al.* 2008).

Another important lesson learned from these first few detections is that it is possible to obtain substantially more

information about the planetary systems than previously thought. In all ten cases, finite source effects have been detectable and so it has been possible to measure  $\theta_E$ , which yields a mass-distance relation for the primary (see Section 3.3). Furthermore, for four systems, additional constraints allow for a complete solution for the primary mass and distance, and so planet mass.

### 5.1. Individual Detections

The first two planets found by microlensing, OGLE-2003-BLG-235/MOA-2003-BLG-53Lb (*Bond et al.*, 2004), and OGLE-2005-BLG-071Lb (*Udalski et al.*, 2005), are Jovian-mass objects with separations of  $\sim 2 - 4$  AU. While the masses and separations of these planets are similar to many of the planets discovered via radial velocity surveys, their host stars are generally less massive and so the planets have substantially lower equilibrium temperatures of  $\sim 50 - 70$  K, similar to Saturn and Uranus.

The third and fourth planets discovered by microlensing are significantly lower mass, and indeed inhabit a region of parameter space that was previously unexplored by any method. OGLE-2005-BLG-390Lb is a very low-mass planet with a planet/star mass ratio of only  $\sim 8 \times 10^{-5}$  (*Beaulieu et al.*, 2006). A Bayesian analysis combined with a measurement of  $\theta_E$  from finite source effects indicates that the planet likely orbits a low-mass M dwarf with  $M = 0.22^{+0.21}_{-0.11} M_{\odot}$ , and thus has a mass of only

$5.5^{+5.5}_{-2.7} M_{\oplus}$ . Its separation is  $2.6^{+1.5}_{-0.6}$  AU, and so has a cool equilibrium temperature of  $\sim 50$  K. OGLE-2005-BLG-169Lb is another low-mass planet with a mass ratio of  $8 \times 10^{-5}$  (Gould *et al.*, 2006), essentially identical to that of OGLE-2005-BLG-390Lb. A Bayesian analysis indicates a primary mass of  $0.52^{+0.19}_{-0.22} M_{\odot}$ , and so a planet of mass  $\sim 14^{+5}_{-6} M_{\oplus}$ , a separation of  $3.3^{+1.9}_{-0.9}$  AU, and an equilibrium temperature of  $\sim 70$  K (Bennett *et al.*, 2007). In terms of its mass and equilibrium temperature, OGLE-2005-BLG-169Lb is very similar to Uranus. OGLE-2005-BLG-169Lb was discovered in a high-magnification  $A_{\max} \sim 800$  event; as argued above, such events have significant sensitivity to multiple planets. There is no indication of any additional planetary perturbations in this event, which excludes Jupiter-mass planets with separations between 0.5-15 AU, and Saturn-mass planets with separations between 0.8-9.5 AU. Thus it appears that this planetary system is likely dominated by the detected Neptune-mass companion.

The fifth and sixth planets discovered by microlensing were detected is what is arguably one of the most information-rich and complex microlensing events ever analyzed, OGLE-2006-BLG-109 (Gaudi *et al.*, 2008; Bennett *et al.*, 2009). The light curve exhibited five distinct features. Four of these features are attributable to the source crossing the resonant caustic of a Saturn-mass planet, and include a short cusp crossing, followed by a pair of caustic crossings, and finally a cusp approach, all spanning roughly two weeks. The fifth feature cannot be explained by the Saturn-mass planet caustic, but rather is due to the source approaching the tip of the central caustic of an inner, Jupiter-mass planet.

The OGLE-2006-BLG-109Lb planetary system bears a remarkable similarity to a scaled version of Jupiter and Saturn. By combining all the available information, it is possible to infer that the primary is an M dwarf with a mass of  $M = 0.51^{+0.05}_{-0.04} M_{\odot}$  at distance of  $D_l = 1.51^{+0.11}_{-0.12}$  kpc. The two planets have masses of  $0.73 \pm 0.06 M_{\text{Jup}}$  and  $0.27 \pm 0.02 M_{\text{Jup}}$  and separations of  $2.3 \pm 0.5$  AU and  $4.5^{+2.1}_{-1.0}$  AU, respectively. Thus the mass and separation ratios of the two planets are very similar to Jupiter and Saturn. Although the two planets in the OGLE-2006-BLG-109Lb system orbit at about half the distance of their Jupiter/Saturn analogs, their equilibrium temperatures are also similar (although somewhat cooler) to Jupiter and Saturn, because of the lower primary mass and luminosity.

The seventh planet detected by microlensing is also a very low-mass, cool planet (Bennett *et al.*, 2008). MOA-2007-BLG-192Lb has a mass ratio of  $q = 2 \times 10^{-4}$ , somewhat smaller than that of Saturn and the sun. However, this event exhibits orbital parallax and the best-fit model also shows evidence for finite source effects, allowing a measurement of the primary mass. In this case, the inferred primary mass is quite low:  $M = 0.060^{+0.028}_{-0.021} M_{\odot}$ , implying a sub-stellar brown-dwarf host, and very low mass for the planet of  $3.3^{+4.9}_{-1.6} M_{\oplus}$ . Remarkably, this planet was detected

from data taken entirely by the MOA and OGLE survey collaborations, without the benefit of additional coverage from the follow-up collaborations. This event therefore serves as an early indication of how future microlensing planet surveys will operate, as detailed in the next section. Unfortunately, in this case, coverage of the planetary perturbation was sparse, and as a result the limits on the mass ratio and primary mass are relatively weak. Fortunately, the inferred primary mass can be confirmed and made more precise with follow-up VLT and/or *HST* observations. If confirmed, this discovery will demonstrate that brown dwarfs can form planetary systems similar to those around solar-type main-sequence stars.

The eighth and ninth microlensing planets, MOA-2007-BLG-400Lb (Dong *et al.*, 2008b) and MOA-2008-BLG-310Lb (Janczak *et al.*, 2009) were detected in events that bear some remarkable similarities. Both were high-magnification events ( $A_{\max} \sim 628$  and  $A_{\max} \sim 400$ , respectively) in which the primary lens transited the source, resulting in a dramatic smoothing of the peak of the event (see panel e of Figure 8 for an example). By eye, single lens models provide relatively good matches to the data. Nevertheless, weak but broad and significant residuals to the single-lens model are apparent in both cases, which are well-fit by perturbations due to the central caustic of a planetary companion. In both cases, the inferred caustic size is significantly smaller than the source size. Also in both cases, precise constraints on the mass ratio are possible despite the weak perturbation amplitudes. MOA-2007-BLG-400Lb is a cool, Jovian-mass planet with mass ratio of  $q = 0.0025 \pm 0.0004$ , and MOA-2008-BLG-310Lb is sub-Saturn mass planet with  $q = (3.3 \pm 0.3) \times 10^{-4}$ . The angular Einstein ring radius of the primary lens 2008-BLG-310-310L as inferred from finite source effects is quite small ( $\theta_E = 0.162 \pm 0.015$  mas), implying that if the primary is a star ( $M \geq 0.08 M_{\odot}$ ), it must have  $D_l > 6.0$  kpc and so be in the bulge (Janczak *et al.*, 2009). This is the best candidate yet for a bulge planet. Unfortunately, it is not possible to definitely determine if the system is in the bulge with currently-available information, and it is possible that the primary is a low-mass star or brown dwarf in the foreground Galactic disk. This ambiguity can be resolved with follow-up high resolution imaging taken immediately, followed by additional observations taken in  $\sim 10$  years, at which point the source and lens will have separated by  $\sim 50$  mas.

The tenth planet, OGLE-2007-BLG-368Lb, is another cold Neptune (Sumi *et al.*, 2009), making it the fourth low-mass ( $\lesssim 20 M_{\oplus}$ ) planet discovered with microlensing. This planet was detected in a relatively low-magnification event with a maximum magnification of only  $\sim 13$ . In this case, the source crossed between the two, triangular-shaped planetary caustics of a close ( $d < 1$ ) topology planetary lens, and thus the light curve exhibited a large ( $\sim 20\%$ ) dip, characteristic of the planetary perturbations due to such configurations (see Figure 9c,d).

## 5.2. Frequency of Cold Planets

The microlensing detection sensitivity declines with planet mass as  $\sim m_p^{1/2}$ , and thus the presence of two low-mass planets amongst the first four detections was an indication that the frequency of cold super Earths/Neptunes ( $5 - 15 M_\oplus$ ) is substantially higher than that of cold Jovian-class planets. *Gould et al.* 2006 performed a quantitative analysis that accounted for the detection sensitivities and Poisson statistics and demonstrated that, at 90% confidence,  $38_{-22}^{+31}\%$  of stars host cold super Earths/Neptunes with separations in the range  $1.6 - 4.3$  AU. An updated analysis taking into account the planets that have since been detected, as well as those events that did not yield planets, revises this number downward to  $\sim 20 \pm 10\%$  (D. Bennett, private communication). Thus, such planets are common, which is ostensibly a confirmation of the core accretion model of planet formation, which predicts that there should exist many more ‘failed Jupiters’ than bona-fide Jovian-mass planets at such separations, particularly around low-mass primaries (*Laughlin et al.*, 2004; *Ida & Lin*, 2005).

By adopting a simple model for the scaling of the detection efficiency with  $q$ , *Sumi et al.* 2009 used the distribution of mass ratios of the ten microlensing planets discovered to date to derive an intrinsic mass (ratio) function of exoplanets beyond the snow line of  $dN/dq \propto q^{-1.7 \pm 0.2}$ . This implies that cold Neptunes/super Earths ( $q \sim 5 \times 10^{-5}$ ) are  $7_{-3}^{+6}$  times more common than cold Jupiters ( $q \sim 10^{-3}$ ), reinforcing the conclusions of *Gould et al.* 2006.

## 5.3. Properties of the Planetary Systems

As already mentioned, for all of the planet detections, it has been possible to obtain additional information to improve the constraints on the properties of the primaries and planets. For example, for OGLE-2003-BLG-235/MOA-2003-BLG-53Lb, follow-up imaging with *HST* yielded a detection of light from the lens, which constrains the mass of the primary and planet to  $\sim 15\%$ ,  $M = 0.63_{-0.09}^{+0.07} M_\odot$  and  $m_p = 2.6_{-0.6}^{+0.8} M_{\text{Jup}}$  (*Bennett et al.*, 2006). However, it is the analysis of events OGLE-2006-BLG-109 (*Bennett et al.*, 2009) and OGLE-2005-BLG-071 (*Dong et al.*, 2009a) which demonstrate most strikingly the detailed information that can be obtained for planets detected via microlensing.

For microlensing event OGLE-2006-BLG-109, besides the basic signatures of the two planets, the light curve displays finite source effects and orbital parallax, which allow for a complete solution to the lens system and so measurements of the mass and distance to the primary, as well as the masses of the planets (*Gaudi et al.*, 2008a; *Bennett et al.*, 2009). This primary mass measurement is corroborated by a Keck AO *H*-band image of the target that yields a measurement of the flux of the lens, which in this case turns out to be brighter than the source. The lens flux is consistent with the mass inferred entirely from the microlensing observables. In addition, the orbital motion of the outer Saturn-mass planet was detected. This was possi-

ble because the source crossed or approached the resonant caustic due to this planet at four distinct times. Furthermore, as discussed in Section 2.3, the exact shape and size of resonant caustics depend sensitively on  $d$ , which changes over the two weeks of the planetary deviations. In fact, four of the six orbital parameters of the Saturn-mass planet are well-measured, and a fifth parameter is weakly constrained. This information, combined with an assumption of coplanarity with the Jupiter-mass planet and the requirement of stability, enables a constraint on the orbital eccentricity of the Saturn-mass planet of  $e = 0.15_{-0.10}^{+0.17}$ , and inclination of the system of  $i = 64_{-7}^{+4}$  degrees (*Bennett et al.*, 2009).

In the case of OGLE-2005-BLG-071Lb, *HST* photometry, when combined with information on finite source effects and microlens parallax from the light curve, allows for a measurement of the primary mass and distance, and so planet mass and projected separation. This leads to the conclusion that the companion is a massive planet with  $m_p = 3.8 \pm 0.4 M_{\text{Jup}}$  and projected separation  $r_\perp = 3.6 \pm 0.2$  AU, orbiting an M-dwarf primary with a mass of  $M = 0.46 \pm 0.04 M_\odot$  and a distance of  $D_l = 3.2 \pm 0.4$  kpc (*Dong et al.*, 2009a). Furthermore, the primary has thick-disk kinematics with a projected velocity relative to the Local Standard of Rest of  $v = 103 \pm 15 \text{ km s}^{-1}$ , suggesting that it may be metal-poor. Thus, OGLE-2005-BLG-071Lb may be a massive Jovian planet orbiting a metal-poor, thick-disk M-dwarf. The existence of such a planet may pose a challenge for core-accretion models of planet formation (e.g., *Laughlin et al.*, 2004; *Ida & Lin*, 2004, 2005).

Interestingly, all four microlensing planet hosts for which it has been possible to measure the distance to the system lie in the foreground disk. As mentioned above, MOA-2008-BLG-310Lb is the most promising candidate for a bulge planet, but in this case the primary could still be a foreground disk brown dwarf. In contrast, roughly 60% of all microlensing events toward the Galactic bulge are due to lenses in the bulge (*Kiraga & Paczynski*, 1994). The lack of confirmed microlensing bulge planets could be due to the selection effect that longer events, which are more likely to arise from disk lenses, are preferentially monitored by the follow-up collaborations, or it could reflect a difference between the planet populations in the disk and bulge. Regardless, with a larger sample of planets with well-constrained distances, and a more careful accounting of selection effects, it should be possible to compare the demographics of planets in the Galactic disk and bulge.

## 6. FUTURE PROSPECTS

In the four seasons of 2003-2006 there were five planetary events, containing six detected planets. With the MOA upgrade in 2006 to the MOA-II phase, the rate of planet detections has increased substantially. From the 2007, 2008, and 2009 bulge seasons, there were four, three, and four secure planetary events, respectively (seven of these await publication). Thus even maintaining the current rate, we can expect of order a dozen new planet detections over the

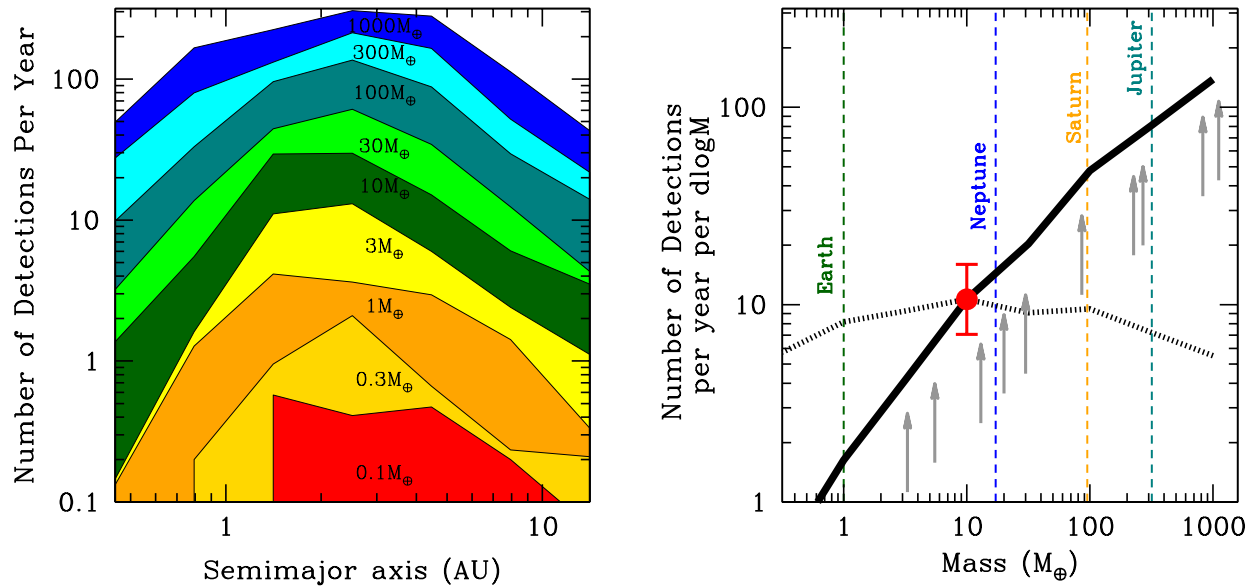


Fig. 13.— Expectations from the next generation of ground-based microlensing surveys, including MOA-II, OGLE-IV, and a KMTNet telescope in South Africa. These results represent the average of two independent simulations, which include very different input assumptions but differ in their predictions by only  $\sim 0.3$  dex. (Left) Number of planets detected per year as a function of semimajor axis for various masses, assuming every star has a planet of the given mass and semimajor axis. (Right) Number of planets detected per year as a function of planet mass, normalized by the number of  $\sim 10 M_{\oplus}$  found to date by microlensing (indicated by the red dot). The solid line is the prediction assuming an equal number of planets per logarithmic mass interval, and the dotted curve assumes that the number of planets per log mass scales as  $m_p^{-0.7}$  (Sumi et al., 2009). In both cases, planets are assumed to be distributed uniformly in  $\log(a)$  between 0.4–20 AU. Arrows indicate the locations of the ten published exoplanets.

next several years. In fact, as described below, we can expect the rate of planet detections to increase substantially, as microlensing planet searches transition toward the next generation of surveys. Besides finding more planets, these surveys will also have improved sensitivity to lower-mass, terrestrial planets. Thus we can expect to have robust constraints on the frequency of Earth-mass planets beyond the snow line within the next decade. A space-based survey would determine the demographics of planets with mass greater than that of Mars and semimajor axis  $\gtrsim 0.5$  AU, determine the frequency of free-floating, Earth-mass planets, and determine the frequency of terrestrial planets in the outer habitable zones of solar-type stars in the Galactic disk and bulge.

The transition to the next generation of ground-based surveys is enabled by the advent of large-format cameras with fields-of-view (FOV) of several square degrees. With such large FOVs, it becomes possible to monitor tens of millions of stars every 10 – 20 minutes, and so discover thousands of microlensing events per year. Furthermore, these events are then simultaneously monitored with the cadence required to detect perturbations due to very low-mass ( $\sim M_{\oplus}$ ) planets. Thus next-generation searches will operate in a very different mode than the current alert/follow-up model. In order to obtain round-the-clock coverage and so catch all of the perturbations, several such telescopes would be needed, located on 3–4 continents roughly evenly spread

in longitude.

In fact, the transition to the ‘next-generation’ is happening already. The MOA-II telescope in New Zealand (1.8m and 2 deg<sup>2</sup> FOV) already represents one leg of such a survey. The OGLE team has recently upgraded to the OGLE-IV phase with a 1.4 deg<sup>2</sup> camera, which will represent the second leg in Chile when it becomes operational in 2010. Although the OGLE telescope has a smaller FOV camera and a smaller aperture (1.3m) than the MOA telescope, these are mostly compensated by the better site quality in Chile. Finally, the Korean Microlensing Telescope Network (KMTNet) is a project with plans to build three 1.6m telescopes with 4 deg<sup>2</sup> FOV cameras, one each in South Africa, South America, and Australia. With the completion of the South African leg of this network (planned 2012), a next-generation survey would effectively be in place. In addition, astronomers from Germany and China are considering initiatives to secure funding to build 1–2m class telescopes with wide FOV cameras in southern Africa or Antarctica.

Detailed simulations of such a next-generation microlensing survey have been performed by several groups (Gaudi et al., unpublished; Bennett, 2004). These simulations include models for the Galactic population of lenses and sources that match all constraints (Han & Gould, 1995, 2003), and account for real-world effects such as weather, variable seeing, moon and sky background, and crowded fields. They reach similar conclusions. Such a survey

would increase the planet detection rate at fixed mass by at least an order of magnitude over current surveys. Figure 13 shows the predictions of these simulations for the detection rate of planets of various masses and separations using a survey including MOA-II, OGLE-IV, and a Korean telescope in South Africa. In particular, if Earth-mass planets with semimajor axes of several AU are common around main-sequence stars, a next generation microlensing survey should detect several such planets per year. This survey would also be sensitive to free-floating planets, and would detect them at a rate of hundreds per year if every star has ejected Jupiter-mass planet.

Ultimately, however, the true potential of microlensing cannot be realized from the ground. Weather, seeing, crowded fields, and systematic errors all conspire to make the detection of planets with mass less than Earth effectively impossible from the ground (Bennett, 2004). As outlined in Bennett & Rhie, 2002, a space-based microlensing survey offers several advantages: the main-sequence bulge sources needed to detect sub-Earth mass planets are resolved from space, the events can be monitored continuously, and it is possible to observe the moderately reddened source stars in the near infrared to improve the photon collection rate. Furthermore, the high spatial resolution afforded by space allows unambiguous identification of light from the primary (lens) stars and so measurements of the primary and planet masses (Bennett et al., 2007).

The expectations from a Discovery-class space-based microlensing survey are impressive. Such a survey would be sensitive to all planets with mass  $\gtrsim 0.1M_{\oplus}$  and separations  $a \gtrsim 0.5$  AU, including free-floating planets (Bennett & Rhie, 2002; Bennett et al., 2009). This range includes analogs to all the solar system planets except Mercury. If every main-sequence star has an Earth-mass planet in the range 1 – 2.5 AU, the survey would detect  $\sim 500$  such planets within its mission lifetime. The survey would also detect a comparable number of habitable Earth-mass planets as the *Kepler* mission (Borucki et al., 2003), and so would provide an important independent measurement of  $\eta_{\oplus}$ . When combined with complementary surveys (such as *Kepler*), a space-based microlensing planet survey would determine the demographics of both bound and free-floating planets with masses greater than that of Mars orbiting stars with masses less than that of the Sun.

The basic requirements for a space-based microlensing planet survey are relatively modest: an aperture of at least 1m, a large FOV camera (at least  $\sim 0.5$  deg<sup>2</sup>) with optical or near-IR detectors, reasonable image quality of better than  $\sim 0.25''$ , and an orbit for which the Galactic bulge is continuously visible. The *Microlensing Planet Finder (MPF)* is an example of a space-based microlensing survey that can accomplish these objectives, essentially entirely with proven technology, and at a cost of  $\sim \$300$  million excluding launch vehicle (Bennett et al., 2009). Interestingly, the requirements for a space-based microlensing planet survey are very similar to, or less stringent than, the requirements for a number of the proposed dark energy missions, in particu-

lar those that focus on weak lensing measurements. Thus, it may be attractive to consider a combined dark energy/planet finding mission that could be accomplished at a substantial savings compared to doing each mission separately (Gould, 2009).

**Acknowledgments.** I would like to thank Subo Dong for preparing Figure 10, Andrzej Udalski for reading over the manuscript, and two anonymous referees for catching some important errors, and comments that greatly improved the presentation.

## REFERENCES

- Afonso, C., Alard, C., Albert, J. N., Andersen, J., Ansari, R., Aubourg, É., Bareyre, P., Bauer, F., Beaulieu, J. P., Bouquet, A., Char, S., Charlot, X., Couchot, F., Coutures, C., Derue, F., Ferlet, R., Glicenstein, J. F., Goldman, B., Gould, A., Graff, D., Gros, M., Haissinski, J., Hamilton, J. C., Hardin, D., de Kat, J., Kim, A., Lasserre, T., Lesquoy, É., Loup, C., Magneville, C., Marquette, J. B., Maurice, É., Milsztajn, A., Moniez, M., Palanque-Delabrouille, N., Perdureau, O., Prévot, L., Regnault, N., Rich, J., Spiro, M., Vidal-Madjar, A., Vigroux, L., Zylberajch, S., Alcock, C., Allsman, R. A., Alves, D., Axelrod, T. S., Becker, A. C., Cook, K. H., Drake, A. J., Freeman, K. C., Griest, K., King, L. J., Lehner, M. J., Marshall, S. L., Minniti, D., Peterson, B. A., Pratt, M. R., Quinn, P. J., Rodgers, A. W., Stetson, P. B., Stubbs, C. W., Sutherland, W., Tomaney, A., Vandehei, T., Rhie, S. H., Bennett, D. P., Fragile, P. C., Johnson, B. R., Quinn, J., Udalski, A., Kubiak, M., Szymański, M., Pietrzyński, G., Woźniak, P., Zebruń, K., Albrow, M. D., Caldwell, J. A. R., DePoy, D. L., Dominik, M., Gaudi, B. S., Greenhill, J., Hill, K., Kane, S., Martin, R., Menzies, J., Naber, R. M., Pogge, R. W., Pollard, K. R., Sackett, P. D., Sahu, K. C., Vermaak, P., Watson, R., & Williams, A. (2000) Combined Analysis of the Binary Lens Caustic-crossing Event MACHO 98-SMC-1. *ApJ*, 532, 340-352
- Afonso, C., Albert, J. N., Andersen, J., Ansari, R., Aubourg, É., Bareyre, P., Bauer, F., Blanc, G., Bouquet, A., Char, S., Charlot, X., Couchot, F., Coutures, C., Derue, F., Ferlet, R., Fouqué, P., Glicenstein, J. F., Goldman, B., Gould, A., Graff, D., Gros, M., Haissinski, J., Hamilton, J. C., Hardin, D., de Kat, J., Kim, A., Lasserre, T., LeGuillou, L., Lesquoy, É., Loup, C., Magneville, C., Mansoux, B., Marquette, J. B., Maurice, É., Milsztajn, A., Moniez, M., Palanque-Delabrouille, N., Perdureau, O., Prévot, L., Regnault, N., Rich, J., Spiro, M., Vidal-Madjar, A., Vigroux, L., Zylberajch, S., & The EROS collaboration (2001) Photometric constraints on microlens spectroscopy of EROS-BLG-2000-5. *A&A*, 378, 1014-1023
- Albrow, M., Beaulieu, J.-P., Birch, P., Caldwell, J. A. R., Kane, S., Martin, R., Menzies, J., Naber, R. M., Pel, J.-W., Pollard, K., Sackett, P. D., Sahu, K. C., Vreesswijk, P., Williams, A., Zwaan, M. A., & The PLANET Collaboration (1998) The 1995 Pilot Campaign of PLANET: Searching for Microlensing Anomalies through Precise, Rapid, Round-the-Clock Monitoring. *ApJ*, 509, 687-702
- Albrow, M. D., Beaulieu, J.-P., Caldwell, J. A. R., Depoy, D. L., Dominik, M., Gaudi, B. S., Gould, A., Greenhill, J., Hill, K., Kane, S., Martin, R., Menzies, J., Naber, R. M., Pollard, K. R., Sackett, P. D., Sahu, K. C., Vermaak, P., Watson, R., Williams,

- A., & Pogge, R. W. (1999a) The Relative Lens-Source Proper Motion in MACHO 98-SMC-1. *ApJ*, 512, 672-677
- Albrow, M. D., Beaulieu, J.-P., Caldwell, J. A. R., Depoy, D. L., Dominik, M., Gaudi, B. S., Gould, A., Greenhill, J., Hill, K., Kane, S., Martin, R., Menzies, J., Naber, R. M., Pogge, R. W., Pollard, K. R., Sackett, P. D., Sahu, K. C., Vermaak, P., Watson, R., Williams, A., & The PLANET Collaboration (1999b) A Complete Set of Solutions for Caustic Crossing Binary Microlensing Events. *ApJ*, 522, 1022-1036
- Albrow, M. D., Beaulieu, J.-P., Caldwell, J. A. R., Dominik, M., Greenhill, J., Hill, K., Kane, S., Martin, R., Menzies, J., Naber, R. M., Pel, J.-W., Pollard, K., Sackett, P. D., Sahu, K. C., Vermaak, P., Watson, R., Williams, A., & Sahu, M. S. (1999c) Limb Darkening of a K Giant in the Galactic Bulge: PLANET Photometry of MACHO 97-BLG-28. *ApJ*, 522, 1011-1021
- Albrow, M. D., An, J., Beaulieu, J.-P., Caldwell, J. A. R., DePoy, D. L., Dominik, M., Gaudi, B. S., Gould, A., Greenhill, J., Hill, K., Kane, S., Martin, R., Menzies, J., Pogge, R. W., Pollard, K. R., Sackett, P. D., Sahu, K. C., Vermaak, P., Watson, R., & Williams, A. (2002) A Short, Nonplanetary, Microlensing Anomaly: Observations and Light-Curve Analysis of MACHO 99-BLG-47. *ApJ*, 572, 1031-1040
- Alcock, C., Akerlof, C. W., Allsman, R. A., Axelrod, T. S., Bennett, D. P., Chan, S., Cook, C. H., Freeman, K. C., Griest, K., Marshall, S. L., Park, H. S., Perlmutter, S., Peterson, B. A., Pratt, M. R., Quinn, P. J., Rodgers, A. W., Stubbs, C. W., & Sutherland, W. (1993) Possible Gravitational Microlensing of a Star in the Large Magellanic Cloud. *Nature*, 365, 621-623
- Alcock, C., Allsman, R. A., Alves, D., Axelrod, T. S., Becker, A. C., Bennett, D. P., Cook, K. H., Freeman, K. C., Griest, K., Guern, J., Lehner, M. J., Marshall, S. L., Peterson, B. A., Pratt, M. R., Quinn, P. J., Reiss, D., Rodgers, A. W., Stubbs, C. W., Sutherland, W., Welch, D. L., & The MACHO Collaboration (1996) Real-Time Detection and Multisite Observations of Gravitational Microlensing. *ApJ*, 463, L67-L70
- Alcock, C., Allsman, R. A., Alves, D., Axelrod, T. S., Becker, A. C., Bennett, D. P., Cook, K. H., Freeman, K. C., Griest, K., Keane, M. J., Lehner, M. J., Marshall, S. L., Minniti, D., Peterson, B. A., Pratt, M. R., Quinn, P. J., Rodgers, A. W., Stubbs, C. W., Sutherland, W., Tomaney, A. B., Vandehei, T., & Welch, D. (1997) First Detection of a Gravitational Microlensing Candidate toward the Small Magellanic Cloud. *ApJ*, 491, L11-L13
- Alcock, C., Allsman, R. A., Alves, D. R., Axelrod, T. S., Becker, A. C., Bennett, D. P., Cook, K. H., Dalal, N., Drake, A. J., Freeman, K. C., Geha, M., Griest, K., Lehner, M. J., Marshall, S. L., Minniti, D., Nelson, C. A., Peterson, B. A., Popowski, P., Pratt, M. R., Quinn, P. J., Stubbs, C. W., Sutherland, W., Tomaney, A. B., Vandehei, T., & Welch, D. (2000) The MACHO Project: Microlensing Results from 5.7 Years of Large Magellanic Cloud Observations. *ApJ*, 542, 281-307
- Agol, E. (2002) Occultation and Microlensing. *ApJ*, 579, 430-436
- An, J. H. (2005) Gravitational lens under perturbations: symmetry of perturbing potentials with invariant caustics. *MNRAS*, 356, 1409-1428
- An, J. H., & Evans, N. W. (2006) The Chang-Refsdal lens revisited. *MNRAS*, 369, 317-334
- Aubourg, E., Bareyre, P., Brehin, S., Gros, M., Lachize-Rey, M., Laurent, B., Lesquoy, E., Magneville, C., Milsztajn, A., Moscoso, L., Queinnee, F., Rich, J., Spiro, M., Vigroux, L., Zylberajch, S., Ansari, R., Cavalier, F., Moniez, M., Beaulieu, J. P., Ferlet, R., Grison, P., Vidal-Madjar, A., Guibert, J., Moreau, O., Tajahmady, F., Maurice, E., Prevot, L., & Gry, C. (1993) Evidence for Gravitational Microlensing by Dark Objects in the Galactic Halo. *Nature*, 365, 623-625
- Beaulieu, J.-P., Bennett, D. P., Fouqué, P., Williams, A., Dominik, M., Jørgensen, U. G., Kubas, D., Cassan, A., Coutures, C., Greenhill, J., Hill, K., Menzies, J., Sackett, P. D., Albrow, M., Brilliant, S., Caldwell, J. A. R., Calitz, J. J., Cook, K. H., Corrales, E., Desort, M., Dieters, S., Dominis, D., Donatowicz, J., Hoffman, M., Kane, S., Marquette, J.-B., Martin, R., Meintjes, P., Pollard, K., Sahu, K., Vinter, C., Wambsganss, J., Woller, K., Horne, K., Steele, I., Bramich, D. M., Burgdorf, M., Snodgrass, C., Bode, M., Udalski, A., Szymański, M. K., Kubiak, M., Więckowski, T., Pietrzyński, G., Soszyński, I., Szewczyk, O., Wyrzykowski, Ł., Paczyński, B., Abe, F., Bond, I. A., Britton, T. R., Gilmore, A. C., Hearnshaw, J. B., Itow, Y., Kamiya, K., Kilmartin, P. M., Korpela, A. V., Masuda, K., Matsubara, Y., Motomura, M., Muraki, Y., Nakamura, S., Okada, C., Ohnishi, K., Rattenbury, N. J., Sako, T., Sato, S., Sasaki, M., Sekiguchi, T., Sullivan, D. J., Tristram, P. J., Yock, P. C. M., & Yoshioka, T. (2006) Discovery of a cool planet of 5.5 Earth masses through gravitational microlensing. *Nature*, 439, 437-440
- Boutreux, T., & Gould, A. (1996) Monte Carlo Simulations of MACHO Parallaxes from a Satellite. *ApJ*, 462, 705-
- Bennett, D. P. (2004) The Detection of Terrestrial Planets via Gravitational Microlensing: Space vs. Ground-based Surveys. *ASPC*, 321, 59-67
- Bennett, D. P. (2009a) Detection of Extrasolar Planets by Gravitational Microlensing. *Exoplanets: Detection, Formation, Properties, Habitability*, eds. J. Mason, (Berlin:Springer) (arXiv:0902.1761)
- Bennett, D. P. (2009b) An Efficient Method for Modeling High Magnification Planetary Microlensing Events. *ApJ*, submitted (arXiv:0911.2703)
- Bennett, D. P., Anderson, J., & Gaudi, B. S. (2007) Characterization of Gravitational Microlensing Planetary Host Stars. *ApJ*, 660, 781-790
- Bennett, D. P., & Rhie, S. H. (1996) Detecting Earth-Mass Planets with Gravitational Microlensing. *ApJ*, 472, 660-664
- Bennett, D. P., & Rhie, S. H. (2002) Simulation of a Space-based Microlensing Survey for Terrestrial Extrasolar Planets. *ApJ*, 574, 985-1003
- Bennett, D. P., Anderson, J., Bond, I. A., Udalski, A., & Gould, A. (2006) Identification of the OGLE-2003-BLG-235/MOAs-2003-BLG-53 Planetary Host Star. *ApJ*, 647, L171-L174
- Bennett, D. P., Anderson, J., & Gaudi, B. S. (2007a) Characterization of Gravitational Microlensing Planetary Host Stars. *ApJ*, 660, 781-790
- Bennett, D. P., Anderson, J., Beaulieu, J. P., Bond, I., Cheng, E., Cook, K., Friedman, S., Gaudi, B. S., Gould, A., Jenkins, J., Kimble, R., Lin, D., Mather, J., Rich, M., Sahu, K., Sumi, T., Tenerelli, D., Udalski, A., & Yoch, P. (2009) A Census of Exoplanets in Orbits Beyond 0.5 AU via Space-based Microlensing. *Astro2010: The Astronomy and Astrophysics Decadal Survey, Science White Papers*, 18
- Bennett, D. P., Bond, I. A., Udalski, A., Sumi, T., Abe, F., Fukui, A., Furusawa, K., Hearnshaw, J. B., Holderness, S., Itow, Y., Kamiya, K., Korpela, A. V., Kilmartin, P. M., Lin, W., Ling, C. H., Masuda, K., Matsubara, Y., Miyake, N., Muraki, Y., Nagaya, M., Okumura, T., Ohnishi, K., Perrott, Y. C., Rattenbury, N. J., Sako, T., Saito, T., Sato, S., Skuljan, L., Sullivan, D. J., Sweatman, W. L., Tristram, P. J., Yock, P. C. M., Kubiak, M., Szymański, M. K., Pietrzyński, G., Soszyński, I., Szewczyk,

- O., Wyrzykowski, L., Ulaczyk, K., Batista, V., Beaulieu, J. P., Brilliant, S., Cassan, A., Fouqué, P., Kervella, P., Kubas, D., & Marquette, J. B. (2008) A Low-Mass Planet with a Possible Sub-Stellar-Mass Host in Microlensing Event MOA-2007-BLG-192. *ApJ*, 684, 663-683
- Bennett, D. P., Rhie, S. H., Nikolaev, S., Gaudi, B. S., Udalski, A., Gould, A., Christie, G. W., Maoz, D., Dong, S., McCormick, J., Szymanski, M. K., Tristram, P. J., Macintosh, B., Cook, K. H., Kubiak, M., Pietrzynski, G., Soszynski, I., Szewczyk, O., Ulaczyk, K., Wyrzykowski, L., DePoy, D. L., Han, C., Kaspi, S., Lee, C. -, Mallia, F., Natusch, T., Park, B. -, Pogge, R. W., Polishook, D., Abe, F., Bond, I. A., Botzler, C. S., Fukui, A., Hearnshaw, J. B., Itow, Y., Kamiya, K., Korpela, A. V., Kilmartin, P. M., Lin, W., Masuda, K., Matsubara, Y., Motomura, M., Muraki, Y., Nakamura, S., Okumura, T., Ohnishi, K., Perrott, Y. C., Rattenbury, N. J., Sako, T., Saito, T., Sato, S., Skuljan, L., Sullivan, D. J., Sumi, T., Sweatman, W. L., Yock, P. C. M., Albrow, M., Allan, A., Beaulieu, J. -, Bramich, D. M., Burgdorf, M. J., Coutures, C., Dominik, M., Dieters, S., Fouque, P., Greenhill, J., Horne, K., Snodgrass, C., Steele, I., Tsapras, Y., Chaboyer, B., Crocker, A., & Frank, S. (2009) Masses and Orbital Constraints for the OGLE-2006-BLG-109Lb,c Jupiter/Saturn Analog Planetary System. *ApJ*, submitted (arXiv:0911.2706)
- Bolatto, A. D., & Falco, E. E. (1994) The detectability of planetary companions of compact Galactic objects from their effects on microlensed light curves of distant stars. *ApJ*, 436, 112-116
- Bond, I. A., Udalski, A., Jaroszyński, M., Rattenbury, N. J., Paczyński, B., Soszyński, I., Wyrzykowski, L., Szymański, M. K., Kubiak, M., Szewczyk, O., Żebruń, K., Pietrzyński, G., Abe, F., Bennett, D. P., Eguchi, S., Furuta, Y., Hearnshaw, J. B., Kamiya, K., Kilmartin, P. M., Kurata, Y., Masuda, K., Matsubara, Y., Muraki, Y., Noda, S., Okajima, K., Sako, T., Sekiguchi, T., Sullivan, D. J., Sumi, T., Tristram, P. J., Yanagisawa, T., & Yock, P. C. M. (2004) OGLE 2003-BLG-235/MOA 2003-BLG-53: A Planetary Microlensing Event. *ApJ*, 606, L155-L158
- Borucki, W. J., Koch, D. G., Lissauer, J. J., Basri, G. B., Caldwell, J. F., Cochran, W. D., Dunham, E. W., Geary, J. C., Latham, D. W., Gilliland, R. L., Caldwell, D. A., Jenkins, J. M., & Kondo, Y. (2003) The Kepler mission: a wide-field-of-view photometer designed to determine the frequency of Earth-size planets around solar-like stars. *SPIE*, 4854, 129-140
- Bozza, V. (2000) Caustics in special multiple lenses. *A&A*, 355, 423-432
- Bromley, B. C. (1996) Finite-Size Gravitational Microlenses. *ApJ*, 467, 537-539
- Calchi Novati, S., Paulin-Henriksson, S., An, J., Baillon, P., Belokurov, V., Carr, B. J., Crézé, M., Evans, N. W., Giraud-Héraud, Y., Gould, A., Hewett, P., Jetzer, P., Kaplan, J., Kerins, E., Smartt, S. J., Stalin, C. S., Tsapras, Y., & Weston, M. J. (2005) POINT-AGAPE pixel lensing survey of M 31. Evidence for a MACHO contribution to galactic halos. *A&A*, 443, 911-928
- Cassan, A. (2008) An alternative parameterisation for binary-lens caustic-crossing events. *A&A*, 491, 587-595
- Chang, K., & Refsdal, S. (1979) Flux variations of QSO 0957+561 A, B and image splitting by stars near the light path. *Nature*, 282, 561-564
- Chang, K., & Refsdal, S. (1984) Star disturbances in gravitational lens galaxies. *A&A*, 132, 168-178
- Chung, S.-J., Han, C., Park, B.-G., Kim, D., Kang, S., Ryu, Y.-H., Kim, K. M., Jeon, Y.-B., Lee, D.-W., Chang, K., Lee, W.-B., & Kang, Y. H. (2005) Properties of Central Caustics in Planetary Microlensing. *ApJ*, 630, 535-542
- Chung, S.-J., Kim, D., Darnley, M. J., Duke, J. P., Gould, A., Han, C., Jeon, Y.-B., Kerins, E., Newsam, A., & Park, B.-G. (2006) The Possibility of Detecting Planets in the Andromeda Galaxy. *ApJ*, 650, 432-437
- Covone, G., de Ritis, R., Dominik, M., & Marino, A. A. (2000) Detecting planets around stars in nearby galaxies. *A&A*, 357, 816-822
- de Jong, J. T. A., Kuijken, K., Crotts, A. P. S., Sackett, P. D., Sutherland, W. J., Uglesich, R. R., Baltz, E. A., Csérjes, P., Gyuk, G., Widrow, L. M., & The MEGA collaboration (2004) First microlensing candidates from the MEGA survey of M 31. *A&A*, 417, 461-477
- Derue, F., Afonso, C., Alard, C., Albert, J.-N., Andersen, J., Ansari, R., Aubourg, É., Bareyre, P., Bauer, F., Beaulieu, J.-P., Blanc, G., Bouquet, A., Char, S., Charlot, X., Couchot, F., Coutures, C., Ferlet, R., Fouqué, P., Glicenstein, J.-F., Goldman, B., Gould, A., Graff, D., Gros, M., Haïssinski, J., Hamilton, J.-C., Hardin, D., de Kat, J., Kim, A., Lasserre, T., Le Guillou, L., Lesquoy, É., Loup, C., Magneville, C., Mansoux, B., Marquette, J.-B., Maurice, É., Milsztajn, A., Moniez, M., Palanque-Delabrouille, N., Perdureau, O., Prévot, L., Regnault, N., Rich, J., Spiro, M., Vidal-Madjar, A., Vigroux, L., & Zylberajch, S. (2001) Observation of microlensing toward the galactic spiral arms. EROS II 3 year survey. *A&A*, 373, 126-138
- Di Stefano, R., & Perna, R. (1997) Identifying Microlensing by Binaries. *ApJ*, 488, 55-63
- Di Stefano, R. (1999) Microlensing and the Search for Extraterrestrial Life. *ApJ*, 512, 558-563
- Di Stefano, R., & Scalzo, R. A. (1999a) A New Channel for the Detection of Planetary Systems through Microlensing. I. Isolated Events due to Planet Lenses. *ApJ*, 512, 564-578
- Di Stefano, R., & Scalzo, R. A. (1999b) A New Channel for the Detection of Planetary Systems through Microlensing. II. Repeating Events. *ApJ*, 512, 579-600
- Di Stefano, R. (2008) Mesolensing Explorations of Nearby Masses: From Planets to Black Holes. *ApJ*, 684, 59-67
- Di Stefano, R., & Night, C. (2008) Discovery and Study of Nearby Habitable Planets with Mesolensing. *ApJ*, submitted (arXiv:0801.1510)
- Dominik, M. (1995) Improved Routines for the Inversion of the Gravitational Lens Equation for a Set of Source Points. *A&AS*, 109, 597-610
- Dominik, M., & Hirshfeld, A. C. (1996) Evidence for a binary lens in the MACHO LMC No. 1 microlensing event. *A&A*, 313, 841-850
- Dominik, M. (1998) Galactic microlensing with rotating binaries. *A&A*, 329, 361-374
- Dominik, M. (1999a) Ambiguities in FITS of observed binary lens galactic microlensing events. *A&A*, 341, 943-953
- Dominik, M. (1999b) The binary gravitational lens and its extreme cases. *A&A*, 349, 108-125
- Dominik, M. (2004a) Theory and practice of microlensing light curves around fold singularities. *MNRAS*, 353, 69-86
- Dominik, M. (2004b) Revealing stellar brightness profiles by means of microlensing fold caustics. *MNRAS*, 353, 118-132
- Dominik, M. (2006) Stochastic distributions of lens and source properties for observed galactic microlensing events. *MNRAS*, 367, 669-692

- Dominik, M. (2007) Adaptive contouring - an efficient way to calculate microlensing light curves of extended sources. *MNRAS*, 377, 1679-1688
- Dominik, M., Jorgensen, U. G., Horne, K., Tsapras, Y., Street, R. A., Wyrzykowski, Ł., Hessman, F. V., Hundertmark, M., Rahvar, S., Wambsganss, J., Scarpetta, G., Bozza, V., Calchi Novati, S., Mancini, L., Masi, G., Teuber, J., Hinse, T. C., Steele, I. A., Burgdorf, M. J., & Kane, S. (2008) Inferring statistics of planet populations by means of automated microlensing searches. (arXiv:0808.0004)
- Dominik, M. (2009) Parameter degeneracies and (un)predictability of gravitational microlensing events. *MNRAS*, 393, 816-821
- Dong, S., DePoy, D. L., Gaudi, B. S., Gould, A., Han, C., Park, B.-G., Pogge, R. W., Udalski, A., Szewczyk, O., Kubiak, M., Szymański, M. K., Pietrzyński, G., Soszyński, I., Wyrzykowski, Ł., Zebur, K. (2006) Planetary Detection Efficiency of the Magnification 3000 Microlensing Event OGLE-2004-BLG-343. *ApJ*, 642, 842-860
- Dong, S., Udalski, A., Gould, A., Reach, W. T., Christie, G. W., Boden, A. F., Bennett, D. P., Fazio, G., Griest, K., Szymański, M. K., Kubiak, M., Soszyński, I., Pietrzyński, G., Szewczyk, O., Wyrzykowski, Ł., Ulaczyk, K., Wieckowski, T., Paczyński, B., DePoy, D. L., Pogge, R. W., Preston, G. W., Thompson, I. B., & Patten, B. M. (2007) First Space-Based Microlens Parallax Measurement: Spitzer Observations of OGLE-2005-SMC-001. *ApJ*, 664, 862-878
- Dong, S., Gould, A., Udalski, A., Anderson, J., Christie, G. W., Gaudi, B. S., The OGLE Collaboration, Jaroszyński, M., Kubiak, M., Szymański, M. K., Pietrzyński, G., Soszyński, I., Szewczyk, O., Ulaczyk, K., Wyrzykowski, Ł., The  $\mu$ FUN Collaboration, DePoy, D. L., Fox, D. B., Gal-Yam, A., Han, C., Lépine, S., McCormick, J., Ofek, E., Park, B.-G., Pogge, R. W., The MOA Collaboration, Abe, F., Bennett, D. P., Bond, I. A., Britton, T. R., Gilmore, A. C., Hearnshaw, J. B., Itow, Y., Kamiya, K., Kilmartin, P. M., Korpela, A., Masuda, K., Matsubara, Y., Motomura, M., Muraki, Y., Nakamura, S., Ohnishi, K., Okada, C., Rattenbury, N., Saito, T., Sako, T., Sasaki, M., Sullivan, D., Sumi, T., Tristram, P. J., Yanagisawa, T., Yock, P. C. M., Yoshioika, T., The PLANET/Robo Net Collaborations, Albrow, M. D., Beaulieu, J. P., Brilant, S., Calitz, H., Cassan, A., Cook, K. H., Coutures, C., Dieters, S., Prester, D. D., Donatowicz, J., Fouqué, P., Greenhill, J., Hill, K., Hoffman, M., Horne, K., Jørgensen, U. G., Kane, S., Kubas, D., Marquette, J. B., Martin, R., Meintjes, P., Menzies, J., Pollard, K. R., Sahu, K. C., Vinter, C., Wambsganss, J., Williams, A., Bode, M., Bramich, D. M., Burgdorf, M., Snodgrass, C., Steele, I., Doublier, V., & Foellmi, C. (2009a) OGLE-2005-BLG-071Lb, the Most Massive M Dwarf Planetary Companion? *ApJ*, 695, 970-987
- Dong, S., Bond, I. A., Gould, A., Kozłowski, S., Miyake, N., Gaudi, B. S., Bennett, D. P., Abe, F., Gilmore, A. C., Fukui, A., Furusawa, K., Hearnshaw, J. B., Itow, Y., Kamiya, K., Kilmartin, P. M., Korpela, A., Lin, W., Ling, C. H., Masuda, K., Matsubara, Y., Muraki, Y., Nagaya, M., Ohnishi, K., Okumura, T., Perrott, Y. C., Rattenbury, N., Saito, T., Sako, T., Sato, S., Skuljan, L., Sullivan, D. J., Sumi, T., Sweatman, W., Tristram, P. J., Yock, P. C. M., The MOA Collaboration, Bolt, G., Christie, G. W., DePoy, D. L., Han, C., Janczak, J., Lee, C.-U., Mallia, F., McCormick, J., Monard, B., Maury, A., Natusch, T., Park, B.-G., Pogge, R. W., Santallo, R., Stanek, K. Z., The  $\mu$ FUN Collaboration, Udalski, A., Kubiak, M., Szymański, M. K., Pietrzyński, G., Soszyński, I., Szewczyk, O., Wyrzykowski, Ł., Ulaczyk, K., & The OGLE Collaboration (2009b) Microlensing Event MOA-2007-BLG-400: Exhuming the Buried Signature of a Cool, Jovian-Mass Planet. *ApJ*, 698, 1826-1837
- Einstein, A. (1936) Lens-Like Action of a Star by the Deviation of Light in the Gravitational Field. *Sci*, 84, 506-507
- Fields, D. L., Albrow, M. D., An, J., Beaulieu, J.-P., Caldwell, J. A. R., DePoy, D. L., Dominik, M., Gaudi, B. S., Gould, A., Greenhill, J., Hill, K., Jørgensen, U. G., Kane, S., Martin, R., Menzies, J., Pogge, R. W., Pollard, K. R., Sackett, P. D., Sahu, K. C., Vermaak, P., Watson, R., Williams, A., Glicenstein, J.-F., & Hauschildt, P. H. (2003) High-Precision Limb-Darkening Measurement of a K3 Giant Using Microlensing. *ApJ*, 596, 1305-1319
- Fluke, C. J., & Webster, R. L. (1999) Investigating the geometry of quasars with microlensing. *MNRAS*, 302, 68-74
- Ford, E. B., & Rasio, F. A. (2008) Origins of Eccentric Extrasolar Planets: Testing the Planet-Planet Scattering Model. *ApJ*, 686, 621-636
- Gaudi, B. S. (1998) Distinguishing Between Binary-Source and Planetary Microlensing Perturbations. *ApJ*, 506, 533-539
- Gaudi, B. S., & Gould, A. (1997a) Satellite Parallaxes of Lensing Events toward the Galactic Bulge. *ApJ*, 477, 152-162
- Gaudi, B. S., & Gould, A. (1997b) Planet Parameters in Microlensing Events. *ApJ*, 486, 85-99
- Gaudi, B. S., & Gould, A. (1999) Spectrophotometric Resolution of Stellar Surfaces with Microlensing. *ApJ*, 513, 619-625
- Gaudi, B. S., & Han, C. (2004) The Many Possible Interpretations of Microlensing Event OGLE 2002-BLG-055. *ApJ*, 611, 528-536
- Gaudi et al. (1998) Microlensing by Multiple Planets in High-Magnification Events. *ApJ*, 502, L33-L37
- Gaudi, B. S., & Petters, A. O. (2002) Gravitational Microlensing near Caustics. I. Folds. *ApJ*, 574, 970-984
- Gaudi, B. S., & Petters, A. O. (2002) Gravitational Microlensing near Caustics. II. Cusps. *ApJ*, 580, 468-489
- Gaudi, B. S., Albrow, M. D., An, J., Beaulieu, J.-P., Caldwell, J. A. R., DePoy, D. L., Dominik, M., Gould, A., Greenhill, J., Hill, K., Kane, S., Martin, R., Menzies, J., Naber, R. M., Pel, J.-W., Pogge, R. W., Pollard, K. R., Sackett, P. D., Sahu, K. C., Vermaak, P., Vreeswijk, P. M., Watson, R., & Williams, A. (2002) Microlensing Constraints on the Frequency of Jupiter-Mass Companions: Analysis of 5 Years of PLANET Photometry. *ApJ*, 566, 463-499
- Gaudi, B. S., Bennett, D. P., Udalski, A., Gould, A., Christie, G. W., Maoz, D., Dong, S., McCormick, J., Szymański, M. K., Tristram, P. J., Nikolaev, S., Paczyński, B., Kubiak, M., Pietrzyński, G., Soszyński, I., Szewczyk, O., Ulaczyk, K., Wyrzykowski, Ł., DePoy, D. L., Han, C., Kaspi, S., Lee, C.-U., Mallia, F., Natusch, T., Pogge, R. W., Park, B.-G., Abe, F., Bond, I. A., Botzler, C. S., Fukui, A., Hearnshaw, J. B., Itow, Y., Kamiya, K., Korpela, A. V., Kilmartin, P. M., Lin, W., Masuda, K., Matsubara, Y., Motomura, M., Muraki, Y., Nakamura, S., Okumura, T., Ohnishi, K., Rattenbury, N. J., Sako, T., Saito, T., Sato, S., Skuljan, L., Sullivan, D. J., Sumi, T., Sweatman, W. L., Yock, P. C. M., Albrow, M. D., Allan, A., Beaulieu, J.-P., Burgdorf, M. J., Cook, K. H., Coutures, C., Dominik, M., Dieters, S., Fouqué, P., Greenhill, J., Horne, K., Steele, I., Tsapras, Y., Chaboyer, B., Crocker, A., Frank, S., & Macintosh, B. (2008a) Discovery of a Jupiter/Saturn Analog with Gravitational Microlensing. *Sci*, 319, 927-930
- Gaudi, B. S., Patterson, J., Spiegel, D. S., Krajci, T., Koff, R.,

- Pojmański, G., Dong, S., Gould, A., Prieto, J. L., Blake, C. H., Roming, P. W. A., Bennett, D. P., Bloom, J. S., Boyd, D., Eyler, M. E., de Ponthière, P., Mirabal, N., Morgan, C. W., Remillard, R. R., Vanmunster, T., Wagner, R. M., & Watson, L. C. (2008b) Discovery of a Very Bright, Nearby Gravitational Microlensing Event. *ApJ*, 677, 1268-1277
- Goldreich, P., Lithwick, Y., & Sari, R. (2004) Final Stages of Planet Formation. *ApJ*, 614, 497-507
- Gould, A. (1992) Extending the MACHO search to about  $10^6$  solar masses. *ApJ*, 392, 442-451
- Gould, A. (1994) Proper motions of MACHOs. *ApJ*, 421, L71-L74
- Gould, A. (1994) MACHO velocities from satellite-based parallaxes. *ApJ*, 421, L75-L78
- Gould, A. (1995) MACHO parallaxes from a single satellite. *ApJ*, 441, L21-L24
- Gould, A. (1996) Microlensing and the Stellar Mass Function. *PASP*, 108, 465-476
- Gould, A. (1999) Microlens Parallaxes with SIRTf. *ApJ*, 514, 869-877
- Gould, A. (2000) Measuring the Remnant Mass Function of the Galactic Bulge. *ApJ*, 535, 928-931
- Gould, A. (2004) Resolution of the MACHO-LMC-5 Puzzle: The Jerk-Parallax Microlens Degeneracy. *ApJ*, 606, 319-325
- Gould, A. (2008) Hexadecapole Approximation in Planetary Microlensing. *ApJ*, 681, 1593-1598
- Gould, A. (2009) Wide Field Imager in Space for Dark Energy and Planets. *Astro2010: The Astronomy and Astrophysics Decadal Survey, Science White Papers*, 100 (arXiv:0902.2211)
- Gould, A., & Gaucherel, C. (1997) Stokes's Theorem Applied to Microlensing of Finite Sources. *ApJ*, 477, 580-584
- Gould, A., & Loeb, A. (1992) Discovering planetary systems through gravitational microlenses. *ApJ*, 396, 104-114
- Gould, A., & Han, C. (2000) Astrometric Resolution of Severely Degenerate Binary Microlensing Events. *ApJ*, 538, 653-656
- Gould, A., Miralda-Escudé, J., & Bahcall, J. N. (1994) Microlensing Events: Thin Disk, Thick Disk, or Halo? *ApJ*, 423, L105-L108
- Gould, A., Udalski, A., An, D., Bennett, D. P., Zhou, A.-Y., Dong, S., Rattenbury, N. J., Gaudi, B. S., Yock, P. C. M., Bond, I. A., Christie, G. W., Horne, K., Anderson, J., Stanek, K. Z., DePoy, D. L., Han, C., McCormick, J., Park, B.-G., Pogge, R. W., Poindexter, S. D., Soszyński, I., Szymański, M. K., Kubiak, M., Pietrzyński, G., Szewczyk, O., Wyrzykowski, Ł., Ulaczyk, K., Paczyński, B., Bramich, D. M., Snodgrass, C., Steele, I. A., Burgdorf, M. J., Bode, M. F., Botzler, C. S., Mao, S., & Swaving, S. C. (2006) Microlens OGLE-2005-BLG-169 Implies That Cool Neptune-like Planets Are Common. *ApJ*, 644, L37-L40
- Griest, K., & Hu, W. (1992) Effect of binary sources on the search for massive astrophysical compact halo objects via microlensing. *ApJ*, 397, 362-380
- Griest, K., & Safizadeh, N. (1998) The Use of High-Magnification Microlensing Events in Discovering Extrasolar Planets. *ApJ*, 500, 37-50
- Han, C. (1999) Analytic relations between the observed gravitational microlensing parameters with and without the effect of blending. *MNRAS*, 309, 373-378
- Han, C. (2006) Properties of Planetary Caustics in Gravitational Microlensing. *ApJ*, 638, 1080-1085
- Han, C. (2008) Microlensing Detections of Moons of Exoplanets. *ApJ*, 684, 684-690
- Han, C. (2009) Distinguishing Between Planetary and Binary Interpretations of Microlensing Central Perturbations Under the Severe Finite-Source Effect. *ApJ*, 691, L9-L12
- Han, C., Gaudi, B. S., An, J. H., & Gould, A. (2005) Microlensing Detection and Characterization of Wide-Separation Planets. *ApJ*, 618, 962-972
- Han, C., & Gaudi, B. S. (2008) A Characteristic Planetary Feature in Double-Peaked, High-Magnification Microlensing Events. *ApJ*, 689, 53-58
- Han, C., & Gould, A. (1995) The Mass Spectrum of MACHOs from Parallax Measurements. *ApJ*, 447, 53-
- Han, C., & Gould, A. (2003) Stellar Contribution to the Galactic Bulge Microlensing Optical Depth. *ApJ*, 592, 172-175
- Han, C., & Han, W. (2002) On the Feasibility of Detecting Satellites of Extrasolar Planets via Microlensing. *ApJ*, 580, 490-493
- Han, C., & Park, M.-G. (2002) A New Channel to Search for Extra-Solar Systems with Multiple Planets via Gravitational Microlensing. *JKAS*, 35, 35-40
- Hamadache, C., Le Guillou, L., Tisserand, P., Afonso, C., Albert, J. N., Andersen, J., Ansari, R., Aubourg, É., Bareyre, P., Beaulieu, J. P., Charlot, X., Coutures, C., Ferlet, R., Fouqué, P., Glicenstein, J. F., Goldman, B., Gould, A., Graff, D., Gros, M., Haissinski, J., de Kat, J., Lesquoy, É., Loup, C., Magneville, C., Marquette, J. B., Maurice, É., Maury, A., Milsztajn, A., Moniez, M., Palanque-Delabrouille, N., Perdereau, O., Rahal, Y. R., Rich, J., Spiro, M., Vidal-Madjar, A., Vigroux, L., & Zylberajch, S. (2006) Galactic Bulge microlensing optical depth from EROS-2. *A&A*, 454, 185-199
- Hardy, S. J., & Walker, M. A. (1995) Parallax effects in binary microlensing events. *MNRAS*, 276, L79-L82
- Holtzman, J. A., Watson, A. M., Baum, W. A., Grillmair, C. J., Groth, E. J., Light, R. M., Lynds, R., & O'Neil, E. J., Jr. (1998) The Luminosity Function and Initial Mass Function in the Galactic Bulge. *AJ*, 115, 1946-1957
- Holz, D. E., & Wald, R. M. (1996) Photon Statistics Limits for Earth-based Parallax Measurements of MACHO Events. *ApJ*, 471, 64-67
- Horne, K., Snodgrass, C., & Tsapras, Y. (2009) A metric and optimization scheme for microlens planet searches. *MNRAS*, 396, 2087-2102
- Ida, S., & Lin, D. N. C. (2004) Toward a Deterministic Model of Planetary Formation. II. The Formation and Retention of Gas Giant Planets around Stars with a Range of Metallicities. *ApJ*, 616, 567-572
- Ida, S., & Lin, D. N. C. (2005) Toward a Deterministic Model of Planetary Formation. III. Mass Distribution of Short-Period Planets around Stars of Various Masses. *ApJ*, 626, 1045-1060
- Ingrasso, G., Calchi Novati, S., De Paolis, F., Jetzer, P., Nucita, A. A., & Zakharov, A. F. (2009) Pixel-lensing as a way to detect extrasolar planets in M31. *MNRAS*, in press (arXiv:0906.1050)
- Janczak, J., et al. (2009) Sub-Saturn Planet MOA-2008-BLG-310Lb: Likely To Be in the Galactic Bulge. *ApJ*, submitted (arXiv:0908.0529)
- Jaroszynski, M., & Mao, S. (2001) Predicting the second caustic crossing in binary microlensing events. *MNRAS*, 325, 1546-1552
- Johnson, J. A., Gaudi, B. S., Sumi, T., Bond, I. A., & Gould, A. (2008) A High-Resolution Spectrum of the Highly Magnified Bulge G Dwarf MOA-2006-BLG-099S. *ApJ*, 685, 508-520
- Jurić, M., & Tremaine, S. (2008) Dynamical Origin of Extrasolar Planet Eccentricity Distribution. *ApJ*, 686, 603-620

- Kennedy, G. M., Kenyon, S. J., & Bromley, B. C. (2007) Planet formation around M-dwarfs: the moving snow line and super-Earths. *Ap&SS*, 311, 9-13
- Kennedy, G. M., & Kenyon, S. J. (2008) Planet Formation around Stars of Various Masses: The Snow Line and the Frequency of Giant Planets. *ApJ*, 673, 502-512
- Kervella, P., Thévenin, F., Di Folco, E., & Ségransan, D. (2004) The angular sizes of dwarf stars and subgiants. Surface brightness relations calibrated by interferometry. *A&A*, 426, 297-307
- Khavinson, D., & Neumann, G. (2006) On the number of zeros of certain rational harmonic functions. *Proc. Amer. Math. Soc.*, 134, 1077-1085
- Kiraga, M., & Paczynski, B. (1994) Gravitational microlensing of the Galactic bulge stars. *ApJ*, 430, L101-L104
- Laughlin, G., Bodenheimer, P., & Adams, F. C. (2004) The Core Accretion Model Predicts Few Jovian-Mass Planets Orbiting Red Dwarfs. *ApJ*, 612, L73-L76
- Lecar, M., Podolak, M., Sasselov, D., & Chiang, E. (2006) On the Location of the Snow Line in a Protoplanetary Disk. *ApJ*, 640, 1115-1118
- Liebes, S. (1964) Gravitational Lenses. *PhRv*, 133, 835-844
- Liebig, C., & Wambsganss, J. (2009) Detectability of extra-solar moons as gravitational microlenses. *A&A*, submitted (arXiv:0912.2076)
- Lissauer, J. J. (1987) Timescales for planetary accretion and the structure of the protoplanetary disk. *Icar*, 69, 249-265
- Mao, S. (1992) Gravitational microlensing by a single star plus external shear. *ApJ*, 389, 63-67
- Mao, S. (2008) Introduction to Gravitational Microlensing (arXiv:0811.0441)
- Mao, S., & Di Stefano, R. (1995) Interpretation of gravitational microlensing by binary systems. *ApJ*, 440, 22-27
- Mao, S., & Paczynski, B. (1991) Gravitational microlensing by double stars and planetary systems. *ApJ*, 374, L37-L40
- Minniti, D., Vandehei, T., Cook, K. H., Griest, K., & Alcock, C. (1998) Detection of Lithium in a Main Sequence Bulge Star Using Keck I as a 15M Diameter Telescope. *ApJ*, 499, L175-L178
- Paczynski, B. (1986) Gravitational microlensing by the galactic halo. *ApJ*, 304, 1-5
- Paczynski, B. (1991) Gravitational microlensing of the Galactic bulge stars. *ApJ*, 371, L63-L67
- Paczynski, B. (1996) Gravitational Microlensing in the Local Group. *ARA&A*, 34, 419-460
- Paczynski, B., & Stanek, K. Z. (1998) Galactocentric Distance with the Optical Gravitational Lensing Experiment and HIP-PARCOS Red Clump Stars. *ApJ*, 494, L219-222
- Palanque-Delabrouille, N., Afonso, C., Albert, J. N., Andersen, J., Ansari, R., Aubourg, E., Bareyre, P., Bauer, F., Beaulieu, J. P., Bouquet, A., Char, S., Charlot, X., Couchot, F., Coutures, C., Derue, F., Ferlet, R., Glicenstein, J. F., Goldman, B., Gould, A., Graff, D., Gros, M., Haissinski, J., Hamilton, J. C., Hardin, D., de Kat, J., Lesquoy, E., Loup, C., Magneville, C., Mansoux, B., Marquette, J. B., Maurice, E., Milsztajn, A., Moniez, M., Perdureau, O., Prevot, L., Renault, C., Rich, J., Spiro, M., Vidal-Madjar, A., Vigroux, L., Zylberajch, S., & The EROS Collaboration (1998) Microlensing towards the Small Magellanic Cloud EROS 2 first year survey. *A&A*, 332, 1-9
- Park, B.-G., Jeon, Y.-B., Lee, C.-U., & Han, C. (2006) Microlensing Sensitivity to Earth-Mass Planets in the Habitable Zone. *ApJ*, 643, 1233-1238
- Paulin-Henriksson, S., Baillon, P., Bouquet, A., Carr, B. J., Crézé, M., Evans, N. W., Giraud-Héraud, Y., Gould, A., Hewett, P., Kaplan, J., Kerins, E., Lastennet, E., Le Du, Y., Melchior, A.-L., Smartt, S. J., & Valls-Gabaud, D. (2002) A Candidate M31/M32 Intergalactic Microlensing Event. *ApJ*, 576, L121-L124
- Peale, S. J. (2001) Probability of Detecting a Planetary Companion during a Microlensing Event. *ApJ*, 552, 889-911
- Pejcha, O., & Heyrovský, D. (2009) Extended-Source Effect and Chromaticity in Two-Point-Mass Microlensing. *ApJ*, 690, 1772-1796
- Petters, A. O., Levine, H., & Wambsganss, J. (2001), *Singularity theory and gravitational lensing*. Birkhäuser, Boston.
- Poindexter, S., Afonso, C., Bennett, D. P., Glicenstein, J.-F., Gould, A., Szymański, M. K., & Udalski, A. (2005) Systematic Analysis of 22 Microlensing Parallax Candidates. *ApJ*, 633, 914-930
- Press, W. H., Teukolsky, S. A., Vetterling, W. T., & Flannery, B. P. (1992), *Numerical recipes in FORTRAN. The art of scientific computing*. University Press, Cambridge.
- Rattenbury, N. J., Bond, I. A., Skuljan, J., & Yock, P. C. M. (2002) Planetary microlensing at high magnification. *MNRAS*, 335, 159-169
- Refsdal, S. (1964) The gravitational lens effect. *MNRAS*, 128, 295-306
- Refsdal, S. (1966) On the possibility of determining the distances and masses of stars from the gravitational lens effect. *MNRAS*, 134, 315-319
- Renn, J., Sauer, T., & Stachel, J. (1997) The origin of gravitational lensing: a postscript to Einstein's 1936 Science paper. *Sci*, 275, 184-186
- Rhie, S. H. (1997) Infimum Microlensing Amplification of the Maximum Number of Images of n-Point Lens Systems. *ApJ*, 484, 63-69
- Rhie, S. H. (2003) How Cumbersome is a Tenth Order Polynomial?: The Case of Gravitational Triple Lens Equation. (arXiv:astro-ph/0202294)
- Rhie, S. H. (2003) n-point Gravitational Lenses with 5(n-1) Images. (arXiv:astro-ph/0305166)
- Rhie, S. H., & Bennett, D. P. (1999) Line Caustic Microlensing and Limb Darkening. (arXiv:astro-ph/9912050)
- Rhie, S. H., Bennett, D. P., Becker, A. C., Peterson, B. A., Fragile, P. C., Johnson, B. R., Quinn, J. L., Crouch, A., Gray, J., King, L., Messenger, B., Thomson, S., Bond, I. A., Abe, F., Carter, B. S., Dodd, R. J., Hearnshaw, J. B., Honda, M., Jugaku, J., Kabe, S., Kilmartin, P. M., Koribalski, B. S., Masuda, K., Matsubara, Y., Muraki, Y., Nakamura, T., Nankivell, G. R., Noda, S., Rattenbury, N. J., Reid, M., Rumsey, N. J., Saito, T., Sato, H., Sato, S., Sekiguchi, M., Sullivan, D. J., Sumi, T., Watase, Y., Yanagisawa, T., Yock, P. C. M., & Yoshizawa, M. (2000) On Planetary Companions to the MACHO 98-BLG-35 Microlens Star. *ApJ*, 533, 378-391
- Sackett, P. D. (1999) Searching for Unseen Planets via Occultation and Microlensing. *Planets Outside the Solar System: Theory and Observations*, eds. J.-M. Mariotti and D. Alloin, (Boston:Kluwer), 189-228 (arXiv:astro-ph/9811269)
- Sako, T., Sekiguchi, T., Sasaki, M., Okajima, K., Abe, F., Bond, I. A., Hearnshaw, J. B., Itow, Y., Kamiya, K., Kilmartin, P. M., Masuda, K., Matsubara, Y., Muraki, Y., Rattenbury, N. J., Sullivan, D. J., Sumi, T., Tristram, P., Yanagisawa, T., & Yock, P. C. M. (2008) MOA-cam3: a wide-field mosaic CCD camera for a gravitational microlensing survey in New Zealand. *ExA*, 22, 51-66

- Sauer, T. (2008) Nova Geminorum 1912 and the origin of the idea of gravitational lensing. *Arch. Hist. Exact Sci.*, 62, 1-22
- Schneider, P., & Weiss, A. (1986) The two-point-mass lens - Detailed investigation of a special asymmetric gravitational lens. *A&A*, 164, 237-259
- Schneider, P., & Weiss, A. (1992) The gravitational lens equation near cusps. *A&A*, 260, 1-2
- Schneider, P., Ehlers, J., & Falco, E. E. (1992), *Gravitational Lenses*. Springer-Verlag, Berlin.
- Smith, M. C., Mao, S., & Paczyński, B. (2003) Acceleration and parallax effects in gravitational microlensing. *MNRAS*, 339, 925-936
- Snodgrass, C., Horne, K., & Tsapras, Y. (2004) The abundance of Galactic planets from OGLE-III 2002 microlensing data. *MNRAS*, 351, 967-975
- Sumi, T., Abe, F., Bond, I. A., Dodd, R. J., Hearnshaw, J. B., Honda, M., Honma, M., Kan-ya, Y., Kilmartin, P. M., Masuda, K., Matsubara, Y., Muraki, Y., Nakamura, T., Nishi, R., Noda, S., Ohnishi, K., Pettersen, O. K. L., Rattenbury, N. J., Reid, M., Saito, T., Saito, Y., Sato, H., Sekiguchi, M., Skuljan, J., Sullivan, D. J., Takeuti, M., Tristram, P. J., Wilkinson, S., Yanagisawa, T., & Yock, P. C. M. (2003) Microlensing Optical Depth toward the Galactic Bulge from Microlensing Observations in Astrophysics Group Observations during 2000 with Difference Image Analysis. *ApJ*, 591, 204-227
- Sumi, T., Bennett, D. P., Bond, I. A., Udalski, A., Batista, V., Dominik, M., Fouqué, P., Kubas, D., Gould, A., Macintosh, B., Cook, K., Dong, S., Skuljan, L., Cassan, A., The MOA Collaboration: F. Abe, Botzler, C. S., Fukui, A., Furusawa, K., Hearnshaw, J. B., Itow, Y., Kamiya, K., Kilmartin, P. M., Korpela, A., Lin, W., Ling, C. H., Masuda, K., Matsubara, Y., Miyake, N., Muraki, Y., Nagaya, M., Nagayama, T., Ohnishi, K., Okumura, T., Perrott, Y. C., Rattenbury, N., Saito, T., Sako, T., Sullivan, D. J., Sweatman, W. L., P., Yock, P. C. M., The PLANET Collaboration: J. P. Beaulieu, Cole, A., Coutures, C., Duran, M. F., Greenhill, J., Jablonski, F., Marboeuf, U., Martioli, E., Pedretti, E., Pejcha, O., Rojo, P., Albrow, M. D., Brilliant, S., Bode, M., Bramich, D. M., Burgdorf, M. J., Caldwell, J. A. R., Calitz, H., Corrales, E., Dieters, S., Dominis Prester, D., Donatowicz, J., Hill, K., Hoffman, M., Horne, K., J. U. G., Kains, N., Kane, S., Marquette, J. B., Martin, R., Meintjes, P., Menzies, J., Pollard, K. R., Sahu, K. C., Snodgrass, C., Steele, I., Street, R., Tsapras, Y., Wambsganss, J., Williams, A., Zub, M., The OGLE Collaboration: M. K. Szyma, Kubiak, M., Pietrzy, G., Soszy, I., Szewczyk, O., Ulaczyk, K., The  $\mu$ SFUN Collaboration: W. Allen, Christie, G. W., DePoy, D. L., Gaudi, B. S., Han, C., Janczak, J., Lee, C. -, McCormick, J., Mallia, F., Monard, B., Natusch, T., Park, B.-G., Pogge, R. W., & Santallo, R. (2009) A Cold Neptune-Mass Planet OGLE-2007-BLG-368Lb: Cold Neptunes Are Common. *ApJ*, submitted (arXiv:0912.1171)
- Thomas, C. L., Griest, K., Popowski, P., Cook, K. H., Drake, A. J., Minniti, D., Myer, D. G., Alcock, C., Allsman, R. A., Alves, D. R., Axelrod, T. S., Becker, A. C., Bennett, D. P., Freeman, K. C., Geha, M., Lehner, M. J., Marshall, S. L., Nelson, C. A., Peterson, B. A., Quinn, P. J., Stubbs, C. W., Sutherland, W., Vandehei, T., & Welch, D. L. (2005) Galactic Bulge Microlensing Events from the MACHO Collaboration. *ApJ*, 631, 906-934
- Tsapras, Y., Street, R., Horne, K., Snodgrass, C., Dominik, M., Allan, A., Steele, I., Bramich, D. M., Saunders, E. S., Rattenbury, N., Mottram, C., Fraser, S., Clay, N., Burgdorf, M., Bode, M., Lister, T. A., Hawkins, E., Beaulieu, J. P., Fouqué, P., Albrow, M., Menzies, J., Cassan, A., & Dominis-Prester, D. (2009) RoboNet-II: Follow-up observations of microlensing events with a robotic network of telescopes. *AN*, 330, 4-11
- Udalski, A., Szymanski, M., Kaluzny, J., Kubiak, M., Krzeminski, W., Mateo, M., Preston, G. W., & Paczynski, B. (1993) The optical gravitational lensing experiment. Discovery of the first candidate microlensing event in the direction of the Galactic Bulge. *AcA*, 43, 289-294
- Udalski, A., Szymanski, M., Kaluzny, J., Kubiak, M., Mateo, M., Krzeminski, W., & Paczynski, B. (1994) The Optical Gravitational Lensing Experiment. The Early Warning System: Real Time Microlensing. *AcA*, 44, 227-234
- Udalski, A., Zebrun, K., Szymanski, M., Kubiak, M., Pietrzynski, G., Soszynski, I., & Wozniak, P. (2000) The Optical Gravitational Lensing Experiment. Catalog of Microlensing Events in the Galactic Bulge. *AcA*, 50, 1-65
- Udalski, A. (2003) The Optical Gravitational Lensing Experiment. Real Time Data Analysis Systems in the OGLE-III Survey. *AcA*, 53, 291-305
- Udalski, A., Jaroszyński, M., Paczyński, B., Kubiak, M., Szymański, M. K., Soszyński, I., Pietrzyński, G., Ulaczyk, K., Szewczyk, O., Wyrzykowski, Ł., Christie, G. W., DePoy, D. L., Dong, S., Gal-Yam, A., Gaudi, B. S., Gould, A., Han, C., Lépine, S., McCormick, J., Park, B.-G., Pogge, R. W., Bennett, D. P., Bond, I. A., Muraki, Y., Tristram, P. J., Yock, P. C. M., Beaulieu, J.-P., Bramich, D. M., Dieters, S. W., Greenhill, J., Hill, K., Horne, K., & Kubas, D. (2005) A Jovian-Mass Planet in Microlensing Event OGLE-2005-BLG-071. *ApJ*, 628, L109-L112
- Uglesich, R. R., Crots, A. P. S., Baltz, E. A., de Jong, J., Boyle, R. P., & Corbally, C. J. (2004) Evidence of Halo Microlensing in M31. *ApJ*, 612, 877-893
- van Belle, G. T. (1999) Predicting Stellar Angular Sizes. *PASP*, 111, 1515-1523
- Vermaak, P. (2000) The effects of resolved sources and blending on the detection of planets via gravitational microlensing. *MNRAS*, 319, 1011-1019
- Vermaak, P. (2003) Rapid analysis of binary lens gravitational microlensing light curves. *MNRAS*, 344, 651-656
- Wambsganss, J. (1997) Discovering Galactic planets by gravitational microlensing: magnification patterns and light curves. *MNRAS*, 284, 172-188
- Witt, H. J. (1990) Investigation of high amplification events in light curves of gravitationally lensed quasars. *A&A*, 236, 311-322
- Witt, H. J. (1995) The Effect of the Stellar Size on Microlensing at the Baade Window. *ApJ*, 449, 42-46
- Witt, H. J., & Mao, S. (1994) Can lensed stars be regarded as pointlike for microlensing by MACHOs?. *ApJ*, 430, 505-510
- Witt, H. J., & Mao, S. (1995) On the Minimum Magnification Between Caustic Crossings for Microlensing by Binary and Multiple Stars. *ApJ*, 447, L105-L108
- Wozniak, P., & Paczynski, B. (1997) Microlensing of Blended Stellar Images. *ApJ*, 487, 55-60
- Yoo, J., DePoy, D. L., Gal-Yam, A., Gaudi, B. S., Gould, A., Han, C., Lipkin, Y., Maoz, D., Ofek, E. O., Park, B.-G., Pogge, R. W., Udalski, A., Soszyński, I., Wyrzykowski, Ł., Kubiak, M., Szymański, M., Pietrzyński, G., Szewczyk, O., Zebruń, K. (2004) OGLE-2003-BLG-262: Finite-Source Effects from a Point-Mass Lens. *ApJ*, 603, 139-151
- Zakharov, A. F. (1995) On the magnification of gravitational lens images near cusps.. *A&A*, 293, 1-4
- Zakharov, A. F. (1999) On the some properties of gravitational lens equation near cusps. *A&AT*, 18, 17-25